


Microstructure and Transient Thermal Stress Analysis  
of  
Austenitic Stainless Steel Weldments  
Using  
Finite Element Method

by



Samir Edmond Chidiac, B. Eng., M.Eng.

A THESIS

Submitted to the School of Graduate Studies  
in Partial Fulfillment of the Requirements

for the Degree

Doctor of Philosophy

McMaster University

May 1988

(C) Copyright by Samir Edmond Chidiac, May 1988.

Modelling of Thermal Effects  
on  
Austenitic Stainless Steel Weldments

To My Parents

Edmond and Naife

DOCTOR OF PHILOSOPHY (1988)  
(Civil Engineering & Engineering Mechanics)

McMASTER UNIVERSITY  
Hamilton, Ontario  
Canada

TITLE:                   Microstructure and Transient Thermal Stress Analysis of  
                          Austenitic Stainless Steel Weldments Using Finite Element  
                          Method

AUTHOR:                Samir Edmond Chidiac  
                          B. Eng. (McMaster University)  
                          M. Eng. (McMaster University)

SUPERVISOR:         Dr. F.A. Mirza

NUMBER OF PAGES:    xvi, 177

## ABSTRACT

A micro/macro-structural analysis is undertaken to determine the effects of welding thermal cycles on austenitic stainless steel. The analysis is subdivided into three parts; heat flow analysis, micro-structural analysis, and thermal elastic visco-plastic analysis.

A three-dimensional, finite element program based on heat conduction equation is developed and also incorporates a model for heat input due to welding to approximate the welding thermal cycles. The program is capable of handling the nonlinear material properties according to the temperature field. A two-point recurrence scheme is employed to obtain the temperature field for every time step. A weighted residual iterative method is employed to minimize drifting.

A micro-structural model based on the Avrami Equation and the grain growth law is developed to predict the grain growth due to welding. The heat affected zone is assumed to be composed mainly of the grain growth zone for the austenitic steel and ignores the recrystallization process.

A coupled thermo-elastic visco-plastic formulation including the micro-structure changes is developed to predict the overall deformations and residual stresses caused by a welding thermal cycle. The macro-structural behaviour is modelled by using the nine-node isoparametric shell element. A twenty seven integration point scheme per element is used to transfer the temperature and the thermal strain field from the heat flow analysis and the ausvenite grain size from the

micro-structural analysis to the thermal elastic visco-plastic analysis. An incremental load method is used along with the Newton-Raphson iterative method to solve for the incremental displacements and hence obtain the macro-structural response.

After the development of all segments of the finite element programs, the accuracy and the stability of the solutions are tested. Various studies are conducted to check the modelling of the heat flow for both low carbon steel and austenitic stainless steel, and the results are compared with the experimental data available in the literature. The micro-structural model is also checked with experimental data available in the literature. Moreover, a micro/macro-structural analysis is performed on heat on edge weld and bead on edge weld for austenitic stainless steel and the results are compared with the experimental and analytical results available in the literature.

## ACKNOWLEDGEMENTS

The author wishes to express his sincere and deepest appreciation to Dr. Farooque A. Mirza, of the Department of Civil Engineering and Engineering Mechanics at McMaster University, for his valuable advice, criticism, and support throughout the research and preparation of this thesis. This appreciation is also extended to Dr. D.S. Wilkinson, of the Department of Materials Science and Engineering at McMaster University, for his valuable advice and constructive criticism throughout the research and formulation of the micro-structural model. The valuable advices of Drs. R.M. Korol and J.D. Embury, members of the supervisory committee, are sincerely appreciated.

The financial assistances from The Natural Science and Engineering Research Council of Canada, McMaster University Hooker's Graduate Scholarships, McMaster University Clifton W. Sherman Scholarship, and the department of Civil Engineering and Engineering Mechanics are deeply appreciated.

The effort and time of Mrs. Marlene Mirza in preparing this thesis are appreciated.

Finally, special thanks to my family and friends for their encouragement and support towards completion of this thesis.

## TABLE OF CONTENTS

ABSTRACT	iii
ACKNOWLEDGEMENTS	v
TABLE OF CONTENTS	vi
LIST OF FIGURES	x
LIST OF TABLES	xvi

### CHAPTER ONE INTRODUCTION

1.1	General	1
1.2	Purpose and Scope	2

### CHAPTER TWO FINITE ELEMENT FORMULATION FOR TRANSIENT HEAT FLOW/WELDING THERMAL CYCLE

2.1	Introduction	6
2.2	Finite Element Formulation	7
2.2.1	Problem Formulation	7
2.2.2	Element Formulation	9
2.3	Transient Solution	13
2.4	Iterative Approach to Non-Linear Problems	14
2.5	Modelling of Heat Input	16
2.6	Modelling of Boundary Conditions	18
2.7	Modelling of Heat Affected Zone	19
2.8	Numerical Examples	20



CHAPTER THREE MICROSTRUCTURAL ANALYSIS OF AUSTENITIC  
STAINLESS STEEL

3.1	Introduction	33
3.2	Grain Growth	34
3.3	Pinning Force/Carbide or Nitride Dissolution	36
3.4	Volume Fraction	37
3.5	Finite Element Formulation for Austenite Grain Growth	39
3.6	Numerical Examples	41

CHAPTER FOUR ELASTO-VISCO-PLASTIC FINITE ELEMENT  
FORMULATION AND APPLICATIONS

4.1	Introduction	56
4.2	Derivation of Finite Element Equilibrium Equations	57
4.3	Isoparametric Shell Element	60
4.4	Constitutive Equations for Elasto- Plastic Analysis	67
4.5	Numerical Algorithm for Elasto- Plastic Formulation	72
4.6	Constitutive Equations for Elastic Visco- -Plastic Analysis	77
4.7	Numerical Algorithm for Elastic Visco-	

	Plastic Formulation	88
4.8	Numerical Examples	91
CHAPTER FIVE EFFECTS OF MICRO-STRUCTURE ON THE MACRO- STRUCTURAL ANALYSIS FOR AUSTENITIC STAINLESS STEEL		
5.1	Introduction	106
5.2	Influence of Temperature on Yield Stress in AISI 316L Austenitic Stainless Steel	106
5.3	Influence of Grain Size on Yield Stress in AISI 316L Austenitic Stainless Steel	108
5.4	Equation Incorporating Micro-structure	109
CHAPTER SIX MICRO/MACRO-STRUCTURAL ANALYSIS OF AUSTENITIC STAINLESS STEEL WELMENDS, NUMERICAL EXAMPLES		
6.1	Introduction	113
6.2	Experimental Studies	114
6.3	Numerical Examples	115
6.3.1	Analysis of Bead-on-Edge Weld	115
6.3.2	Thermal Cycle	115
6.3.3	Grain Growth	117
6.3.4	Finite Element Modelling for the Macro- Structural Analysis	117
6.3.5	Thermo-Elastic Visco-Plastic Analysis	119

6.4.1	Analysis of Heat-on-Edge Weld	122
6.4.2	Thermal Cycle	122
6.4.3	Grain Growth	123
CHAPTER SEVEN CONCLUSIONS AND RECOMMENDATIONS		
7.1	Conclusions	152
7.2	Recommendations	155
APPENDIX A	Element Shape Function	157
APPENDIX B	Construction of Orthogonal Basis	161
APPENDIX C	Mathematical Model for the Pinning Force	164
APPENDIX D	Steffensen Method	168
APPENDIX E	Numerical Instability in the Grain Growth Model	169
BIBLIOGRAPHY		172

## LIST OF FIGURES

### CHAPTER TWO

Fig. 2.1 <sub>a</sub>	(a) A Three-dimensional Isoparametric Element	22
	(b) Parent Element Parabolic	22
Fig. 2.2	A Schematic Representation of the Non-Linear Iterative Method	23
Fig. 2.3	Experimental Data for Radiation, Convection and Conduction for Carbon Steel	24
Fig. 2.4	Geometry and Material Properties for the Transient Heat Flow Problem	25
Fig. 2.5	Isothermals 0.1 - 0.9 for a Square Plate with Unit Initial and Zero Surface Temperature at $t=0.32$ sec. from F.E. Analysis and Close Form Solution	25
Fig. 2.6	Thermal Conductivity of Mild Steel	26
Fig. 2.7	Heat Capacity of Mild Steel	27
Fig. 2.8	Surface Coefficient of Heat Transfer	28
Fig. 2.9	Geometry and Mesh Pattern of the Specimen, and Properties of the Welding Arc	29
Fig. 2.10	Thermal Cycle of the Heat-Affected Zone of a Bead-Welded Specimen	30

Fig. 2.11	Evolution of Temperatures ( $^{\circ}\text{C}$ ) at $t=3.94$ sec	31
Fig. 2.12	Evolution of Temperatures ( $^{\circ}\text{C}$ ) at $t=23.62$ sec	31
Fig. 2.13	Evolution of Temperatures ( $^{\circ}\text{C}$ ) at $t=47.24$ sec	32
Fig. 2.14	Evolution of Temperatures ( $^{\circ}\text{C}$ ) at $t=66.93$ sec	32

### CHAPTER THREE

Fig. 3.1	A Schematic Diagram for the Various Sub- zones of the Heat Affected Zone	45
Fig. 3.2	Idealised Weld Thermal Cycle	46
Fig. 3.3	Influence of Heating and Cooling Rate on Particle Volume Fraction	47
Fig. 3.4	Simulated Welding Thermal Cycle	48
Fig. 3.5	Geometry and Mesh Pattern Used for the Analysis of Austenitic Stainless Steel 316	49
Fig. 3.6	Grain Size Distribution	50
Fig. 3.7	Grain Growth Diagram for a Peak Temperature Equal to $1050^{\circ}\text{C}$	51
Fig. 3.8	Grain Growth Diagram for a Peak Temperature Equal to $1150^{\circ}\text{C}$	52
Fig. 3.9	Grain Growth Diagram for a Peak Temperature Equal to $1250^{\circ}\text{C}$	53

Fig. 3.10	Grain Growth Diagram for a Peak Temperature Equal to 1350°C	54
Fig. 3.11	Grain Size Vs. Maximum Temperature	55

#### CHAPTER FOUR

Fig. 4.1	(a) Parabolic Isoparametric Hexadron	95
	(b) Degeneration to a Shell Element	95
	(c) Parabolic Parent Element	95
Fig. 4.2	Incremental Load Analysis with Newton-- Raphson Iterations	96
Fig. 4.3	Operation Sequence for the Frontal Solver	97
Fig. 4.4	Flow Chart for the Elastic Visco-Plastic Analysis Program	98
Fig. 4.5	Geometry and Material Properties of Simply Supported Plate (Thick Plate Analysis)	99
Fig. 4.6	Load Displacement Curve	99
Fig. 4.7	Geometry and Material Properties of Simply Supported Plate (Thin Plate Analysis)	100
Fig. 4.8	Load Displacement Curve	100
Fig. 4.9	Geometry and Mesh Pattern for the Determinate Structure	101
Fig. 4.10	Time Vs. Maximum Deflection	102
Fig. 4.11	Geometry and Mesh Pattern for the Indeterminate Structure	103

Fig. 4.12	Time Vs. Maximum Deflection (Fully Explicit, $\theta = 0.0$ )	104
Fig. 4.13	Time Vs. Maximum Deflection (Implicit Scheme, $\theta = 0.5$ )	105
CHAPTER FIVE		
Fig. 5.1	Influence of Temperature on the Yield Stress	111
Fig. 5.2	Influence of Austenite Grain Size, $\phi$ , on the Yield Stress at 20 <sup>o</sup> C, 300 <sup>o</sup> C and 600 <sup>o</sup> C	112
CHAPTER SIX		
Fig. 6.1	Specimen Preparations for 308 Stainless Steel	126
Fig. 6.2	Thermal Conductivity of Stainless Steel (Type 316)	127
Fig. 6.3	Thermal Diffusivity of Stainless Steel (Type 316)	128
Fig. 6.4	Surface Coefficient of Heat Transfer	129
Fig. 6.5	Young's Modulus at Elevated Temperatures	130
Fig. 6.6	Yield Point at Various Temperatures	131
Fig. 6.7	Coefficient of Linear Expansion at Elevated Temperatures	132

Fig. 6.8	Geometry and Mesh Pattern of the Specimen, and Properties of the Welding Arc	133
Fig. 6.9	Maximum Reached Temperature Distribution (GMA Weld)	134
Fig. 6.10	Evolution of Temperature ( $^{\circ}\text{C}$ ) at $t=2.12$ sec	135
Fig. 6.11	Evolution of Temperature ( $^{\circ}\text{C}$ ) at $t=23.28$ sec	135
Fig. 6.12	Evolution of Temperature ( $^{\circ}\text{C}$ ) at $t=44.45$ sec	136
Fig. 6.13	Evolution of Temperature ( $^{\circ}\text{C}$ ) at $t=65.62$ sec	136
Fig. 6.14	Evolution of Temperature ( $^{\circ}\text{C}$ ) at $t=86.78$ sec	137
Fig. 6.15	Evolution of Temperature ( $^{\circ}\text{C}$ ) at $t=129.12$ sec	137
Fig. 6.16	Transient Temperature at 2.54 cm from Welding Edge (GMA Weld)	138
Fig. 6.17	Grain Size Distribution	139
Fig. 6.18	Mesh Pattern and the Visco-Plastic Material Properties	140
Fig. 6.19	Deflection Changes at the Centre of 308 Stainless Steel	141
Fig. 6.20	Strain Changes for 308 Stainless Steel at 2.54 cm from Welded Edge	142



Fig. 6.21	Strain Changes for 308 Stainless Steel at 4.45 cm from Welded Edge	143
Fig. 6.22	Longitudinal Residual Stress Distribution	144
Fig. 6.23	Transverse Residual Stress Distribution	145
Fig. 6.24	Maximum Reached Temperature Distribution (GTA Weld)	146
Fig. 6.25	Evolution of Temperature ( $^{\circ}\text{C}$ ) at $t=3.88$ sec	147
Fig. 6.26	Evolution of Temperature ( $^{\circ}\text{C}$ ) at $t=34.90$ sec	147
Fig. 6.27	Evolution of Temperature ( $^{\circ}\text{C}$ ) at $t=69.80$ sec	148
Fig. 6.28	Evolution of Temperature ( $^{\circ}\text{C}$ ) at $t=104.70$ sec	148
Fig. 6.29	Evolution of Temperature ( $^{\circ}\text{C}$ ) at $t=139.60$ sec	149
Fig. 6.30	Evolution of Temperature ( $^{\circ}\text{C}$ ) at $t=182.26$ sec.	149
Fig. 6.31	Transient Temperature at 2.54 cm from Welding Edge (GTA Weld)	150
Fig. 6.32	Grain Size Distribution	151

## LIST OF TABLES

### CHAPTER TWO

Table 2.1	Arc Efficiency for Various Welding Processes and Materials	21
-----------	--	----

### CHAPTER FOUR

Table 4.1	Sampling Points and Weighting Factors in Gauss-Legendre Numerical Integration	94
-----------	---	----

### CHAPTER FIVE

Table 5.1	Composition of Steels Investigated (wt.-%)	110
-----------	--	-----

### CHAPTER SIX

Table 6.1	Chemical Composition of Stainless Steel (Type 308)	125
-----------	--	-----



## CHAPTER ONE

### INTRODUCTION

#### 1.1 General

Welded structures generally involve complex geometric shapes and are subjected to severe thermal loads during fabrication. A proper analysis to determine strength and stiffness of such structures depends largely on the accurate predictions of the heat flow and a realistic macro-structural model that is capable of predicting the thermal effects and their influence on mechanical properties. Moreover, the accuracy of such analysis depends on a proper representation of the geometry of welded structures, particularly in the weld regions. The finite element method provides a powerful tool for analysis of such problems because of its versatility and the availability of computers. The ability of the finite element method to deal with structures of arbitrary complex shape, transient loadings, and also highly nonlinear material properties makes it very attractive when dealing with the analysis of thermally loaded structures and particularly welded structures.

Few researchers have attempted to use numerical models to predict thermal strains, stresses and distortions that are caused by welding. The most recent publication on the past and current knowledge of such analysis and designs of weldments and welded structures has been reported by Masubushi [24]. Furthermore, Ashby and Easterling [6,18], and Alberry and Jones [3,4] have attempted to study the microstructural changes that occur during welding. The currently available model-

ling procedures for the transient problems are rather inefficient and inadequate. This is due to economic limitations, some models have usually included gross simplifications with respect to the load history, the microstructural changes and the material behavior. Furthermore, no attempt was made to relate the effects of microstructural changes, due to welding, to the macro-analysis. Keeping the above effects in mind, a thermo-elastic visco-plastic finite element model is proposed to predict the thermal regime and the corresponding microstructural changes, and then to predict the effects of the above two on the overall structure, particularly thermal strains, stresses and distortions. Two finite element programs have been developed for the modelling of welded structures and their accuracy and stability are tested and compared with the experimental results available in the literature.

## 1.2 Purpose and Scope

The purpose of the present study is to investigate the microstructural changes that occur in Austenitic Stainless Steel due to a welding thermal cycle and then to determine their combined effect on the overall structure. This is accomplished by developing and testing a thermo-elastic visco-plastic finite element model and the subsequent computer programs. To limit the complexity of microstructural changes, this study is concentrated on the modelling of austenitic stainless steel which does not undergo a phase change and therefore avoids the process of recrystallization. While the microstructural model is only limited to austenitic stainless steel, the heat flow analysis and the macrostructural analysis are applicable to all metals provided the material properties are known at high temperatures.

A three-dimensional model is employed to model the heat flow in either a thick or a thin structural element. A recurrence scheme along with an iterative approach is used to obtain the temperature field for successive time intervals. The same three-dimensional interpolation functions are used to obtain the grain size distribution. A general shell element is adopted to model the thermo-elastic visco-plastic response. Due to inelastic behavior, the incremental load method along with the Newton-Raphson method is employed to model the mechanical behavior at each time step. Furthermore, an implicit scheme is employed to compute the updated stress field when performing the visco-plastic analysis.

The finite element formulation for transient heat flow in solids, particularly the welding thermal cycle, is discussed in Chapter Two. The finite element method using the three-dimensional, twenty node isoparametric brick element is discussed. Due to variation in the thermal properties an iterative approach on the residual quantities is desirable and a suitable scheme is employed within each time step. The Gaussian quadrature method is used with twenty seven integration points per element for numerical integration. The transient solution, using a two point recurrence scheme, is also presented. In the analysis of welds, the moving heat source is represented as a source area. The Cauchy and Dirichlet boundary conditions are used to model the heat transfer on the boundary. The modelling of the heat affected zone is also presented. To assess the stability and accuracy of the finite element method, the local and overall performances of the thermal model are investigated and the results are compared to the empirical and experimental results available in the literature.

The microstructural analysis of austenitic stainless steel is discussed in Chapter Three. A mathematical model predicting the austenite grain growth and the definition of the heat affected zone are discussed in this chapter. The Avrami equation is employed in this study to determine the changes that occur in the particle volume fraction due to a welding thermal cycle. Furthermore, the pinning force is computed based on the carbide/nitride dissolution which is a function of the particle volume fraction. A finite element formulation for austenite grain growth is also presented. The stability and accuracy of the proposed model are tested by comparing the results to the analytical and experimental results available in the literature.

Chapter Four describes the elasto-visco-plastic modelling, and the derivation of the finite element equilibrium equations using the virtual work method. The geometry, the displacement field, the stress-strain relationships, and the formulation of the nine node isoparametric shell element are briefly presented. The constitutive equations for elasto-plastic analysis along with the incremental load method and the Newton-Raphson iterative technique are discussed. Also, the constitutive equations for the elastic visco-plastic analysis, using an implicit time stepping formulation to numerically update the relevant stiffness matrix, is presented. Gaussian quadrature is used with the twenty seven integration points per element. A numerical algorithm for the elastic visco-plastic formulation is also presented. To test the model, elastic, elasto-plastic and elastic visco-plastic test problems are carried out. Furthermore, the stability and accuracy of the selective integration technique is explored for nonlinear analyses.

The effects of microstructure on the macrostructural analysis for austenitic stainless steel are discussed in Chapter Five. The influence of temperature on the yield stress, observed experimentally, is presented. The influence of the austenite grain size on the yield stress, again observed experimentally, is also presented. Finally, to incorporate their combined effects on the yield stress and the visco-plastic strain rate, The Hall-Petch equation is employed and is discussed in this chapter.

Chapter Six describes the overall micro- and macro-structural analysis of austenitic stainless steel weldments. There are two cases studied experimentally by Hwang [17] and are used for comparison purposes. A bead-on-edge weld is first analyzed using the proposed thermo-elastic visco-plastic model. The thermal cycle, the austenite grain growth, the thermal deformations, and the residual strains and stresses due to the bead-on-edge weld are calculated and are compared with the experimental results available in the literature. A heat-on-edge weld is also analysed using the transient heat flow model. The thermal cycle and the austenite grain growth due to the heat-on-edge weld are shown and compared with the experimental data available in the literature. However, the overall macro-structural analysis has been omitted because a complete analysis for bead-on-edge has been presented and is believed to be sufficient for demonstration purposes.

## CHAPTER TWO

### FINITE ELEMENT FORMULATION FOR TRANSIENT HEAT FLOW/ WELDING THERMAL CYCLE

#### 2.1 Introduction

Due to material non-linearities and complicated initial and boundary conditions involved in determining the temperature distribution in and around weldments, there is no choice but to use a numerical method. There are two methods that have been extensively used to solve the parabolic equation for transient heat flow problems; the finite difference method and the finite element method. In this study, the more versatile finite element method using the twenty-node three-dimensional isoparametric element is adopted to model the transient heat flow. Because of the elevated temperatures involved due to welding, material nonlinearities are involved and the method accommodates such temperature dependent material properties. This is accomplished through an iterative approach which is incorporated within each time step. This approach allows the use of linear analysis within each time step with some correction to compensate for deviations due to non-linearities.

The finite element formulation of the heat flow problem is based on the principle of virtual work. The transient problem is solved using a time-stepping scheme with options provided for either implicit or fully explicit time marching. A two-point recurrence scheme is adopted to accomplish this. To optimize the com-



puter storage requirement, the skyline technique by Bathe [7] has been adopted to assemble the necessary heat balance matrices.

In the analysis of welds, the emphasis is placed on modelling of the heat generated by a welding arc, and the dissipation of this heat. All possible modes of heat transfer are considered. However, the molten zone has been ignored in the modelling process.

To assess the accuracy and stability of the finite element method, a transient heat flow problem is analyzed and the solution is compared with the existing exact solution. The local and overall performance of the thermal model is tested by comparing both the peak temperatures and cooling rates with either the empirical or experimental results available in the literature.

## 2.2 Finite Element Formulation

### 2.2.1 Problem Statement

The transient heat flow via conduction is governed by the following differential equation

$$\frac{\partial}{\partial x} \left( K_x \frac{\partial T}{\partial x} \right) + \frac{\partial}{\partial y} \left( K_y \frac{\partial T}{\partial y} \right) + \frac{\partial}{\partial z} \left( K_z \frac{\partial T}{\partial z} \right) + Q = \rho C_p \frac{\partial T}{\partial t} \quad (2.1)$$

and can be subject to boundary conditions of the following type;

$$T = T_A \quad \text{on } S_A \quad (2.2)$$

$$K_x \frac{\partial T}{\partial x} \nu_x + K_y \frac{\partial T}{\partial y} \nu_y + K_z \frac{\partial T}{\partial z} \nu_z + q + h(T - T_B) = 0 \quad \text{on } S_B \quad (2.3)$$

where

- T = temperature;
- Q = heat input per unit volume;
- $K_x$  = principal thermal conductivity in x-direction;
- $K_y$  = principal thermal conductivity in y-direction;
- $K_z$  = principal thermal conductivity in z-direction;
- $\rho$  = density;
- $C_p$  = specific heat at constant pressure;
- q = heat input per unit area on boundary  $S_B$ ;
- $T_A$  = specified temperature on boundary  $S_A$ ;
- $\nu_\eta$  = direction cosines of the unit outward normal to the boundary;
- h = coefficient of surface heat transfer;
- t = time; and
- S = running coordinate along the boundary.

The variational principle for Equations 2.1, 2.2 and 2.3, for a linear problem, is well established and given by

$$I = \int_V \left[ \frac{1}{2} \left\{ K_x \left( \frac{\partial T}{\partial x} \right)^2 + K_y \left( \frac{\partial T}{\partial y} \right)^2 + K_z \left( \frac{\partial T}{\partial z} \right)^2 \right\} + QT - \right.$$

$$\rho C_P \frac{\partial T}{\partial t} dV + \int_{S_B} [qT + h\left(\frac{T}{2} - T_B\right)T] dS \quad (2.4)$$

and is valid at any instant of time. The first variation of I in Equation 2.4 yields the field Equation 2.1 and the boundary conditions in Equations 2.2 and 2.3 in the following manner

$$\begin{aligned} \delta I = & - \int_V \left[ K_x \frac{\partial^2 T}{\partial x^2} + K_y \frac{\partial^2 T}{\partial y^2} + K_z \frac{\partial^2 T}{\partial z^2} + Q - \rho C_P \frac{\partial T}{\partial t} \right] \delta T dV \\ & + \int_{S_B} \left[ K_x \frac{\partial T}{\partial x} \nu_x + K_y \frac{\partial T}{\partial y} \nu_y + K_z \frac{\partial T}{\partial z} \nu_z + q + h(T - T_B) \right] \delta T dS \\ & + \int_{S - S_A - S_B} \left[ K_x \frac{\partial T}{\partial x} \nu_x + K_y \frac{\partial T}{\partial y} \nu_y + K_z \frac{\partial T}{\partial z} \nu_z \right] \delta T dS \end{aligned} \quad (2.5)$$

However, for nonlinear analysis due to temperature dependent material properties, the principle of virtual work is adopted for the finite element formulation. Equation 2.5 above also represents the virtual work equation or the weak form in the case of nonlinear analysis.

### 2.2.2 Element Formulation

The three-dimensional isoparametric element, shown in Figure 2.1, has been employed to model heat flow. The twenty-node brick element is adopted

because of its broad applicability. The finite element formulation of the element has been detailed in the literature [7,36] and only a summary is presented here.

For the isoparametric element adopted in this study, the relationship between the cartesian coordinates  $x$ ,  $y$ , and  $z$  and the parent coordinates  $r$ ,  $s$ , and  $t$  is given by

$$X = [N] \{X_e\} = N_i X_{ei}$$

$$Y = [N] \{Y_e\} = N_i Y_{ei} \quad (2.6)$$

$$Z = [N] \{Z_e\} = N_i Z_{ei}$$

where  $[N]$  is the matrix of shape functions in terms of coordinates  $r$ ,  $s$ , and  $t$ . A listing appears in Appendix A.  $\{X_e\}$ ,  $\{Y_e\}$  and  $\{Z_e\}$  are vectors of nodal coordinates of the element. Similarly, the unknown temperature field within an element can be approximated using the same shape functions as employed in Equation 2.6, i.e.

$$T = [N] \{T_e\} = N_i T_{ei} \quad (2.7)$$

According to Zienkiewics et al. [36], and Irons [19], the finite element convergence criteria is satisfied and the element faces are compatible if the interpolation functions,  $[N]$ , chosen preserve the continuity of  $T$  and possess the constant derivatives with respect to  $r$ ,  $s$ , and  $t$  and constant temperature. The transformation

between the cartesian and the parent co-ordinate systems is well established and there derivative components are obtained from

$$\begin{bmatrix} \frac{\partial}{\partial x} N_i \\ \frac{\partial}{\partial y} N_i \\ \frac{\partial}{\partial z} N_i \end{bmatrix} = [J]^{-1} \begin{bmatrix} \frac{\partial}{\partial r} N_i \\ \frac{\partial}{\partial s} N_i \\ \frac{\partial}{\partial t} N_i \end{bmatrix} \quad (2.8)$$

where [J] is the jacobian matrix and is given by

$$[J] = \frac{\partial(X, Y, Z)}{\partial(r, s, t)} \quad (2.9)$$

Once the transformation has been established, it is more convenient to deal with the parent co-ordinates.

Using Equation 2.7, the following integral equation can be obtained as a weak form for a nonlinear problem;

$$\int_{V_2} \frac{1}{2} \left[ (N_{i,x} K_x N_{j,x} + N_{i,y} K_y N_{j,y} + N_{i,z} K_z N_{j,z}) T_i T_j - 2N_i Q T_i \right. \\ \left. + \rho C_p N_i N_j T_i T_j \right] dV +$$

$$\int_{S_B} \left[ qN_i + h \left( \frac{1}{2} N_i N_j T_j - T_B N_i \right) \right] T_i dS = 0 \quad (2.10)$$

The discretized equations of heat balance of Equation 2.10 can be written in the following matrix form;

$$[A] \{T\} + [H] \{\dot{T}\} = \{f(t)\} \quad (2.11)$$

where

$\{\dot{T}\}$  = the time derivative of  $T_i$

$[A]$  = heat conductance matrix

$$A_{ij} = \int_V (N_{i,x} K_x N_{j,x} + N_{i,y} K_y N_{j,y} + N_{i,z} K_z N_{j,z}) dV + \int_{S_B} h N_i N_j dS$$

$[H]$  = heat capacitance matrix

$$H_{ij} = \int_V \rho C_p N_i N_j dV$$

$\{f\}$  = heat input vector

$$f_i = \int_V N_i Q dV - \int_{S_B} N_i (q - hT_B) dS$$

In order to evaluate matrices  $[A]$ ,  $[H]$ , and  $\{f\}$ , numerical integration has been employed. The following transformation for infinitesimal volumes is required for integration over the parent element;

$$dx dy dz = \det[J] dr ds dt \quad (2.12)$$

Gaussian Quadrature with twenty seven integration points is used to perform the numerical integration. As mentioned before, a two-point recurrence scheme is adopted for time marching.

### 2.3 Transient Heat Flow Solution

The two-point recurrence scheme has been implemented to obtain the solution at subsequent times. The following equation describes the recurrence scheme;

$$\left[ \frac{1}{\Delta t_n} [H] + \theta[A] \right] \{T_{n+1}\} = \left[ \frac{1}{\Delta t_n} [H] - (1-\theta)[A] \right] \{T_n\} + \theta\{f_{n+1}\} + (1-\theta)\{f_n\} \quad (2.13)$$

where  $\Delta t_n$  represent the  $n^{\text{th}}$  time interval and  $\theta$  is a parameter that controls the time marching scheme. The value of  $\theta$  varies from 0, for the fully explicit scheme, to 1, for the fully implicit scheme. Note that  $\theta = \frac{1}{2}$  for the Crank-Nicholson method and  $\frac{2}{3}$  for the Galerkin, Zienkiewicz [35].

The instability and oscillation of the two point recurrence scheme were examined by Zienckiewicz [35] and Snyder et al. [30]. They concluded that the time stepping procedure is unconditionally stable when  $\theta$  is greater than or equal to  $\frac{1}{2}$ . In this study, the Galerkin method is adopted, i.e,  $\theta = \frac{2}{3}$ , as it was found to yield superior results. However, the accuracy of results does not depend on  $\theta$  values above but also on the finite element discretization. Because of the elevated temperatures that are involved in the analyses to be presented in this study, the material nonlinearities have to be accounted for during each time step. Due to changes in the thermal properties, an iterative approach has been incorporated and is discussed next.

#### 2.4 Iterative Approach

Without properly accounting for the nonlinearities expected in the thermal properties, the proposed solution procedure will result in errors in the calculated temperature field. The severity of these errors depends on the changes that occur in the temperature field. To overcome this problem, a residual method is proposed to eliminate drifting and at the same time obtain a better approximation. As the temperature changes during the time increment  $\Delta t$ , the thermal properties will change accordingly. Re-writing Equation 2.13 as

$$[K] \{^{i+1}T_{n+1}\} + \{R\} = \{0\} \quad (2.14)$$

where



$$[K] = \frac{1}{\Delta t_n} [H] + \theta [A]$$

$$\{R\} = \left[ \frac{1}{\Delta t_n} [H] - (1-\theta)[A] \right] \{T_n\} + \theta \{f_{n+1}\} + (1-\theta)\{f_n\}$$

For  $i+1$  iteration during  $\Delta t_n$  time increment. This yields a new temperature field  $T_{n+1}^{i+1}$ . Now based on this new temperature field, the material properties are updated and subsequently the heat balance matrices are calculated in the following implicit manner:

$$\begin{aligned} [A]^{i+\theta} &= (1-\theta)[A]^i + \theta[A]^{i+1} \\ [H]^{i+\theta} &= (1-\theta)[H]^i + \theta[H]^{i+1} \end{aligned} \quad (2.15)$$

From the updated material properties, the heat balance residual  $\Delta R^i$  can be obtained as

$$\Delta R^i = [K] \{T_{n+1}^{i+1}\} + \{R_{n+1}\} \quad (2.16)$$

Now the incremental temperature due to  $\Delta R^i$  can be calculated from the following:

$$\{\Delta T_{n+1}^i\} = -[K_{n+1}^0] \{\Delta R^i\}$$

and 
$$T_{n+1}^{i+1} = T_{n+1}^i + \Delta T_{n+1}^i \quad (2.17)$$

After updating the temperature field, the process is repeated until the norm of the incremental temperature vector is small enough within a specified tolerance. Note that the initial  $[K_{n+1}^0]$  is used during such iterations to avoid the decomposition during each iteration within the time step. The residual method described above is schematically shown in Figure 2.2.

## 2.5 Modelling of Heat Input

During a metal-arc welding, the heat is generated as a result of phase transformation of the metal, the chemical reaction between the two metals being welded and the electric power of the welding arc. The first two sources are considered negligible in comparison with the heat generated by the welding arc and hence are completely ignored.

The heat generated by the electric power of a welding arc is given by

$$H = V.I \quad (2.18)$$

where

- H = heat in joules per seconds
- V = arc voltage in Volts
- I = arc current in Amps.

Equation 2.18 can be rearranged so that it expresses the intensity of the

welding heat source. Furthermore, the heat generated by the electric power is not fully transferred to the workpiece. A small portion of that heat is lost to the surrounding atmosphere and some is used to melt the electrode. By far the largest recipient of the heat input is the workpiece through heat conduction and is of most interest in this study. The net heat supplied to the workpiece is, then, given by

$$q = \eta_a \frac{V \cdot I}{v} \quad (2.19)$$

where  $\eta_a$  is called the arc efficiency and  $v$  is the velocity at which the arc moves. The value of  $\eta_a$  varies depending on the type of welding arc and the kind of metal used. To illustrate the wide range of  $\eta_a$ , some values are tabulated in Table 2.1 as given by Masubushi [24]. The determination of the arc efficiency is an important practical consideration. Because of its dependence on many factors as indicated in Table 2.1, it becomes necessary to determine the value experimentally.

The effective thermal power of the welding arc needs to be expressed as

$$Q = 0.24 \eta_a \frac{V \cdot I}{v} \quad (2.20)$$

in which  $Q$  is in calories per centimeter. Equation 2.20 has been adopted to model the heat generated in the workpiece in this study.

The modelling of the heat input is very important in the analysis of welded specimen and particularly in predicting the peak temperature. In this study,

the heat input is per unit area and is considered uniform across the face of an element.

## 2.6 Modelling of Boundary Conditions

The weak form (Equation 2.4) used for the finite element formulation, incorporated the heat balance equation and the boundary conditions given in Equations 2.1, 2.2, and 2.3. The Dirichlet boundary condition (Equation 2.2) on  $S_A$  is easily incorporated by specifying the nodal degrees of freedom along  $S_A$  to take the prescribed values. However, the Cauchy boundary condition (Equation 2.3) along  $S_B$  is much more complex and involves the three modes of heat transfer, namely conduction, convection and radiation. For conduction only

$$q = -\left(K_x \frac{\partial T}{\partial x} \nu_x + K_y \frac{\partial T}{\partial y} \nu_y + K_z \frac{\partial T}{\partial z} \nu_z\right) \quad (2.21)$$

and for convection only is given by

$$h(T - T_B) = -\left(K_x \frac{\partial T}{\partial x} \nu_x + K_y \frac{\partial T}{\partial y} \nu_y + K_z \frac{\partial T}{\partial z} \nu_z\right) \quad (2.22)$$

where  $h$  represents the respective coefficient of heat transfer from the surface.

The major difficulty arises because of the lack of accurate values of the parameter  $h$  at elevated temperatures. To overcome this problem it is proposed that the surface heat transfer coefficient be approximated as a function of the total emissivity which is a measure of radiation. Further, it has been shown experimentally by

Beer and Meek [9] that the effect of convection is less than five percent (Figure 2.3). Based on their experimental results, it is proposed to increase the value of  $h$  obtained from the radiation by five percent to approximately compensate for the convection term.

## 2.7 Modelling of Heat Affected Zone

The metal adjacent to the weld is exposed to high thermal loadings and also undergoes metallurgical changes. This portion of the workpiece, called the heat affected zone (HAZ), is composed of various zones namely, grain growth zone, grain refined zone, partially transformed zone and tempered zone, Easterling [14]. The size and microstructure of each zone is important. However, it has been shown that the microstructure of the grain growth zone plays the most significant role in determination of the weld soundness.

To model this area, it is assumed that the HAZ is composed of only the grain growth zone. Furthermore, as is shown schematically by Easterling [14] in Figure 2.3, the peak temperature at the center of the weld and at the fusion zone are almost identical. This justifies that there is no need to consider the actual weld and the heat generated by the metal fusion in the modelling. Thus the effect of the weld and the transition zone on the thermal cycle are completely ignored in this study.

## 2.8 Numerical Examples

Due to lack of closed form solutions for three-dimensional heat flow problems, it was decided to compare the results with the exact solution for a two-dimensional heat flow problem. A square plate was used for this purpose. The geometry and material properties of the square plate used, to test the accuracy of the model, are shown in Figure 2.4. The closed form solution by Carslaw et al. [10] was given in the form of isothermal contours at one instant of time and is shown in Figure 2.5. The results from the finite element program were identical to the closed form solution. This example demonstrates that the solutions obtained from the three-dimensional transient finite element program are stable and accurate, and hence, can be extended to model weldments.

The heat generated by a welding arc and the heat transfer from and to the workpiece were also modelled. This is accomplished by checking the peak temperature and the cooling rate of the workpiece. The experimental work done by Kihara et al. [21] is used to check the accuracy and stability of the finite element model presented here. The material properties of the specimen are shown in Figures 2.6 to 2.8. The geometry of the specimen, the finite element grid, and the properties of the welding arc are shown in Figure 2.9. Figure 2.10 shows the results obtained from the finite element model and those by Kihara et al. [21]. Figures 2.11 to 2.14 show the temperature field at different times. It can be concluded from the results presented that the finite element model is fully capable of modelling the transient thermal regimes of weldments and will be extended for performing micro-structural analysis.

TABLE 2.1

ARC EFFICIENCY FOR VARIOUS WELDING PROCESSES AND MATERIALS [14]

MATERIAL	WELDING PROCESS	$\eta_A$
Mild Steel	Submerged-arc, ac	90-99%
	Shielded metal-arc	66-85%
	GMA	66-70%
	GTA, ac	22-48%
	GTA, dc	36-46%
Aluminum	GMA	70-85%
	GTA, ac	21-43%
Tin	GTA, ac	21-28%

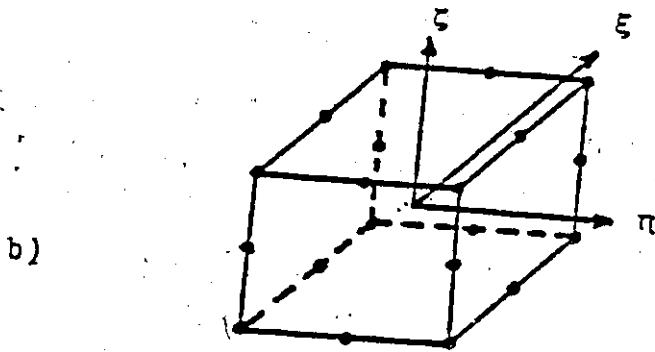
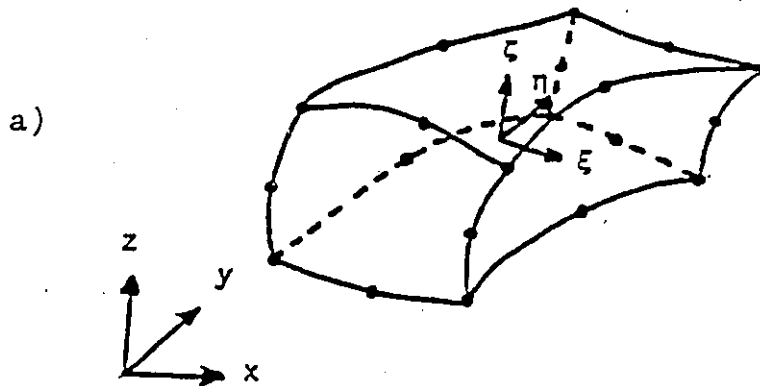


FIG. 2.1 A THREE-DIMENSIONAL ISOPARAMETRIC ELEMENT;  
b) PARENT ELEMENT PARABOLIC.



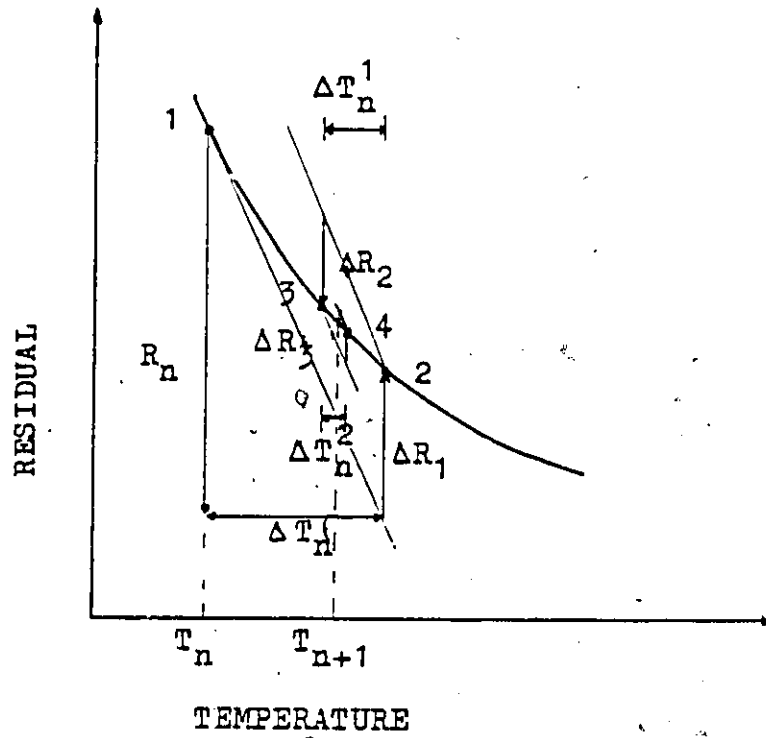


FIG. 2.2 A SCHEMATIC REPRESENTATION OF THE NON-LINEAR ITERATIVE METHOD.

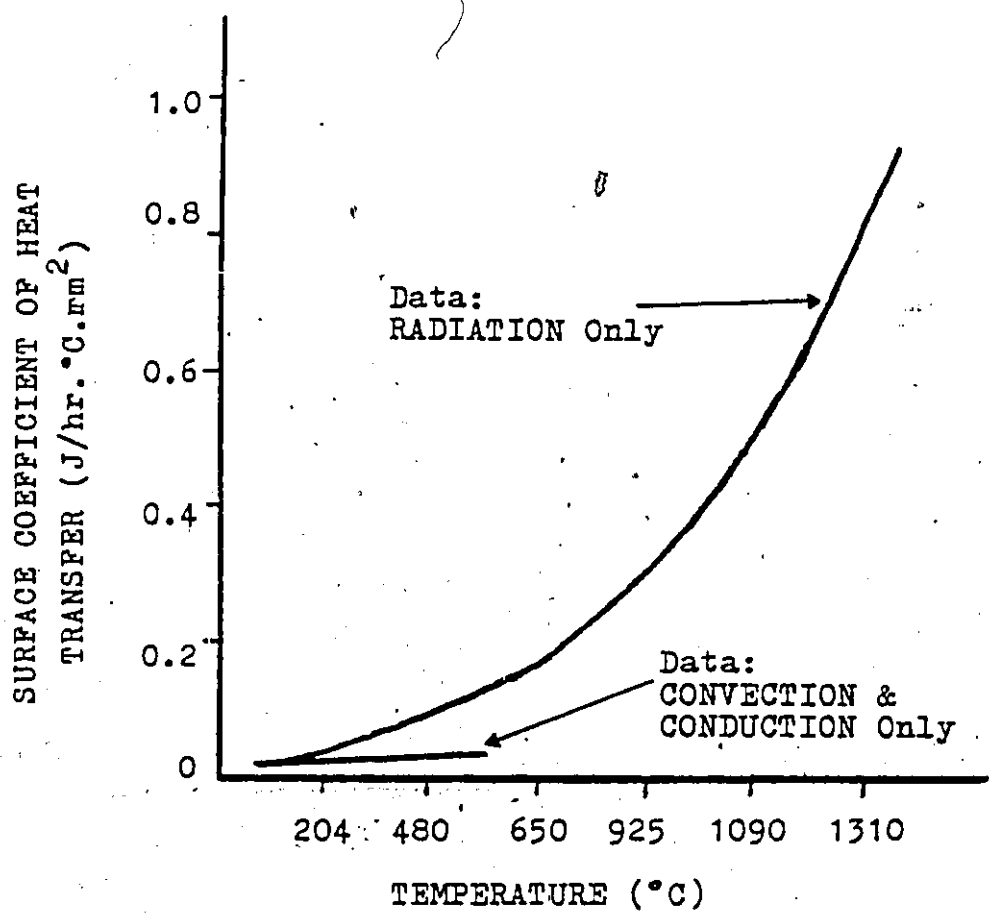


FIG. 2.3 EXPERIMENTAL DATA FOR RADIATION, CONVECTION AND CONDUCTION FOR CARBON STEEL [2].

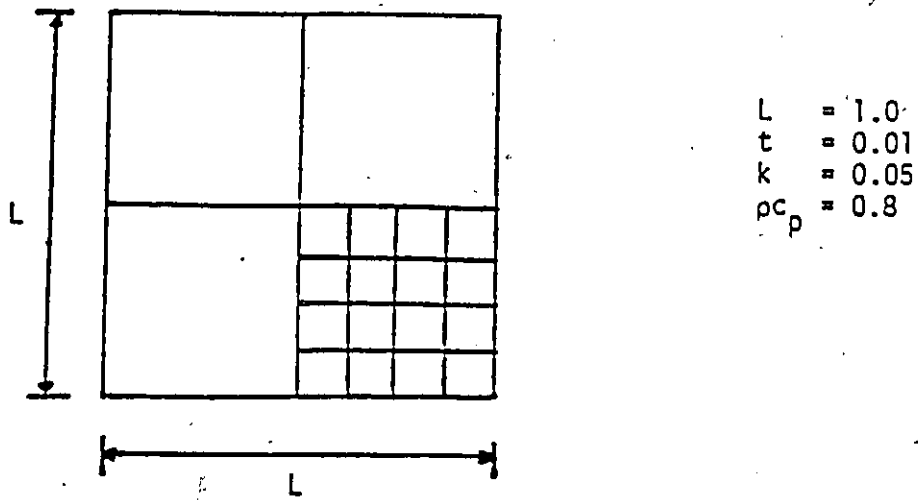


FIG. 2.4 GEOMETRY AND MATERIAL PROPERTIES FOR THE TRANSIENT HEAT FLOW PROBLEM.

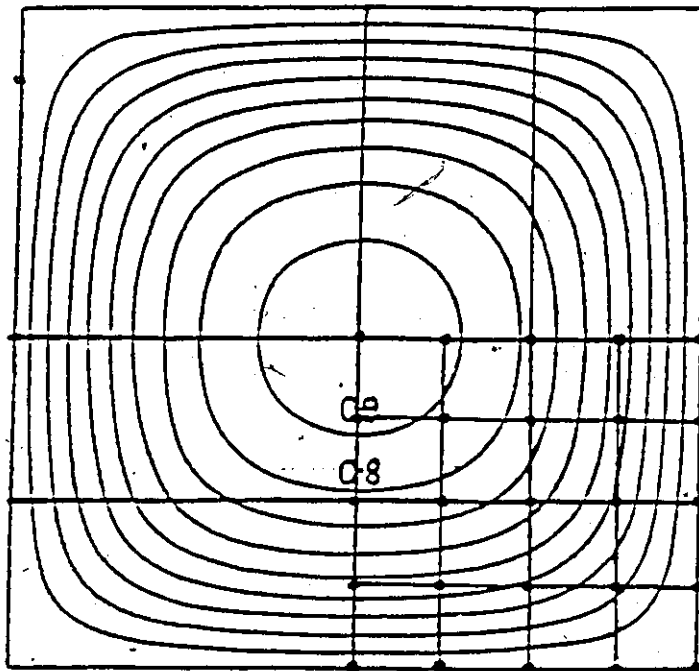


FIG. 2.5 ISOTHERMALS 0.1 - 0.9 FOR A SQUARE PLATE WITH UNIT INITIAL AND ZERO SURFACE TEMPERATURE AT  $t=0.32$  sec. FROM F.E. ANALYSIS & CLOSE FORM SOLUTION.

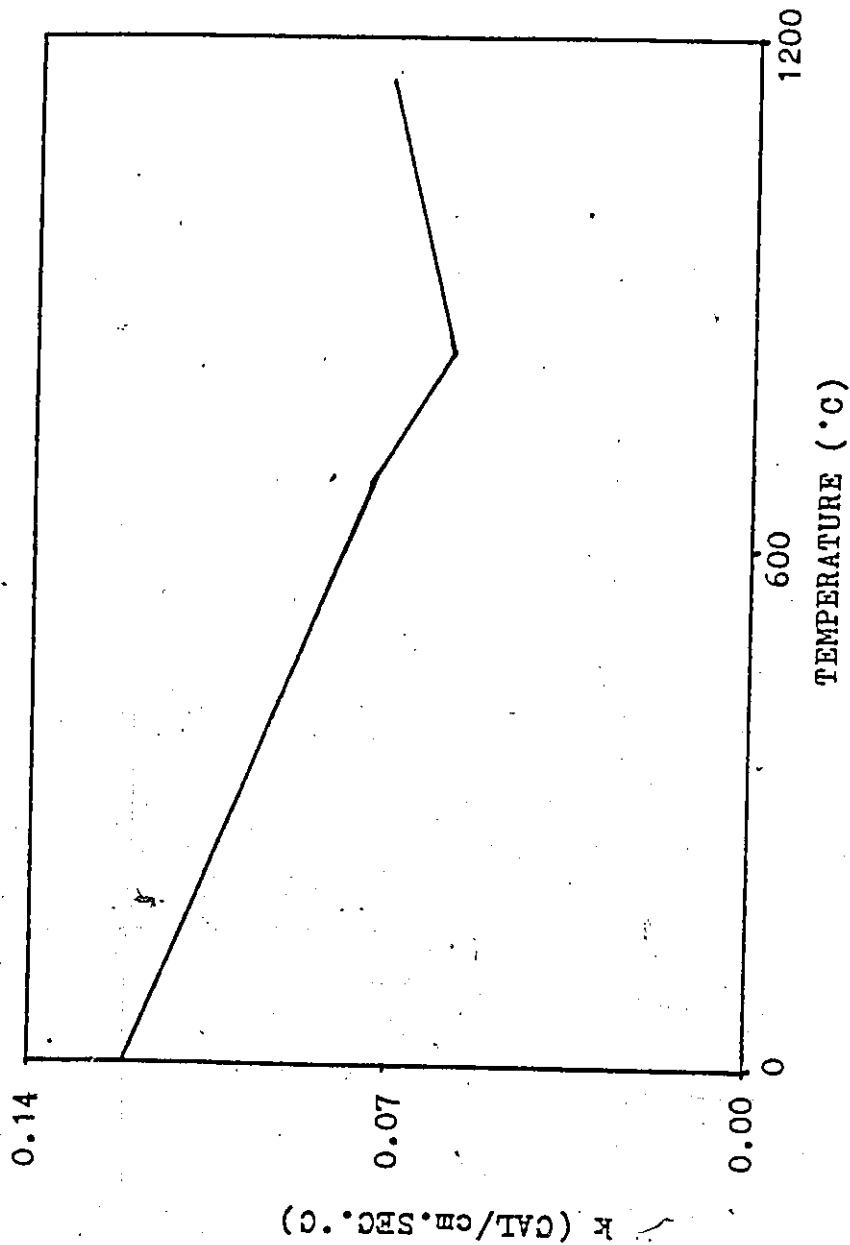


FIG. 2.6 THERMAL CONDUCTIVITY OF MILD STEEL [5].

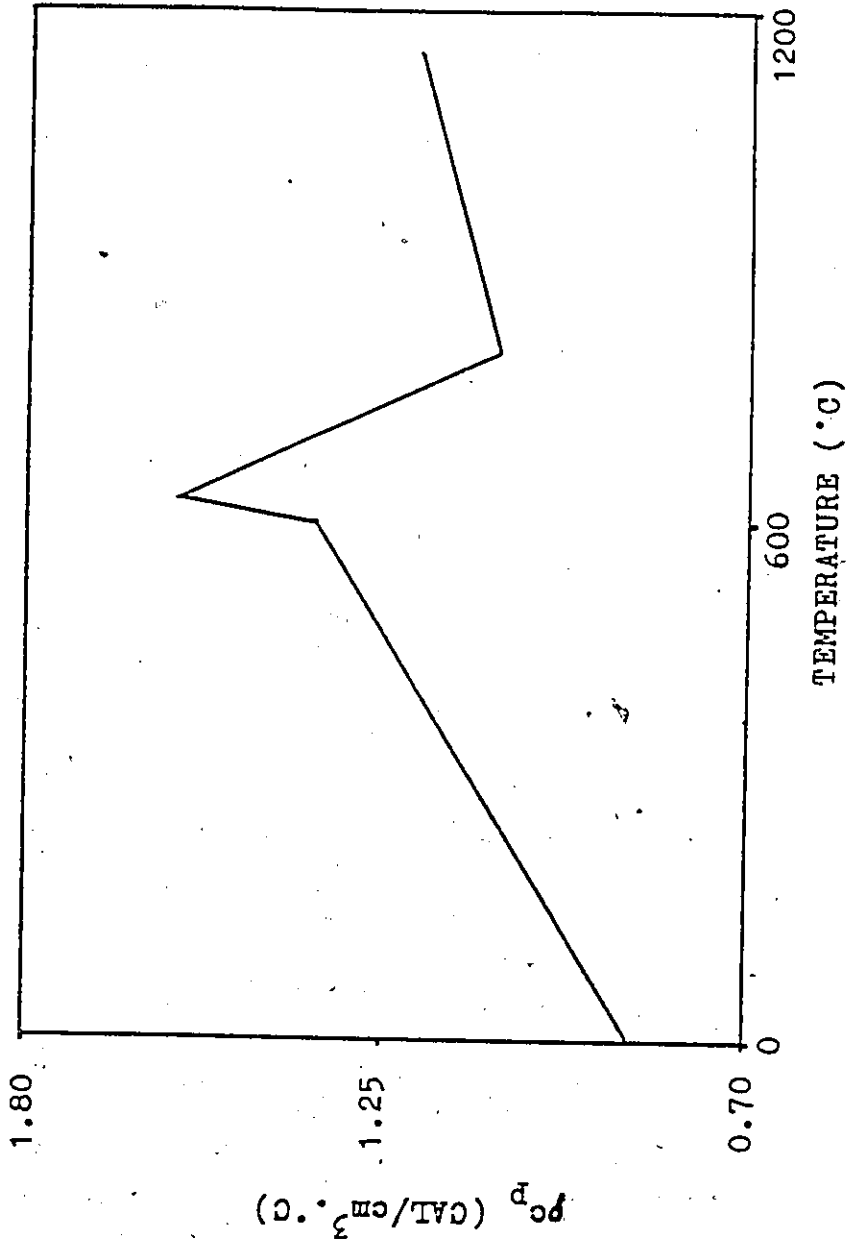


FIG. 2.7 HEAT CAPACITY OF MILD STEEL [5].

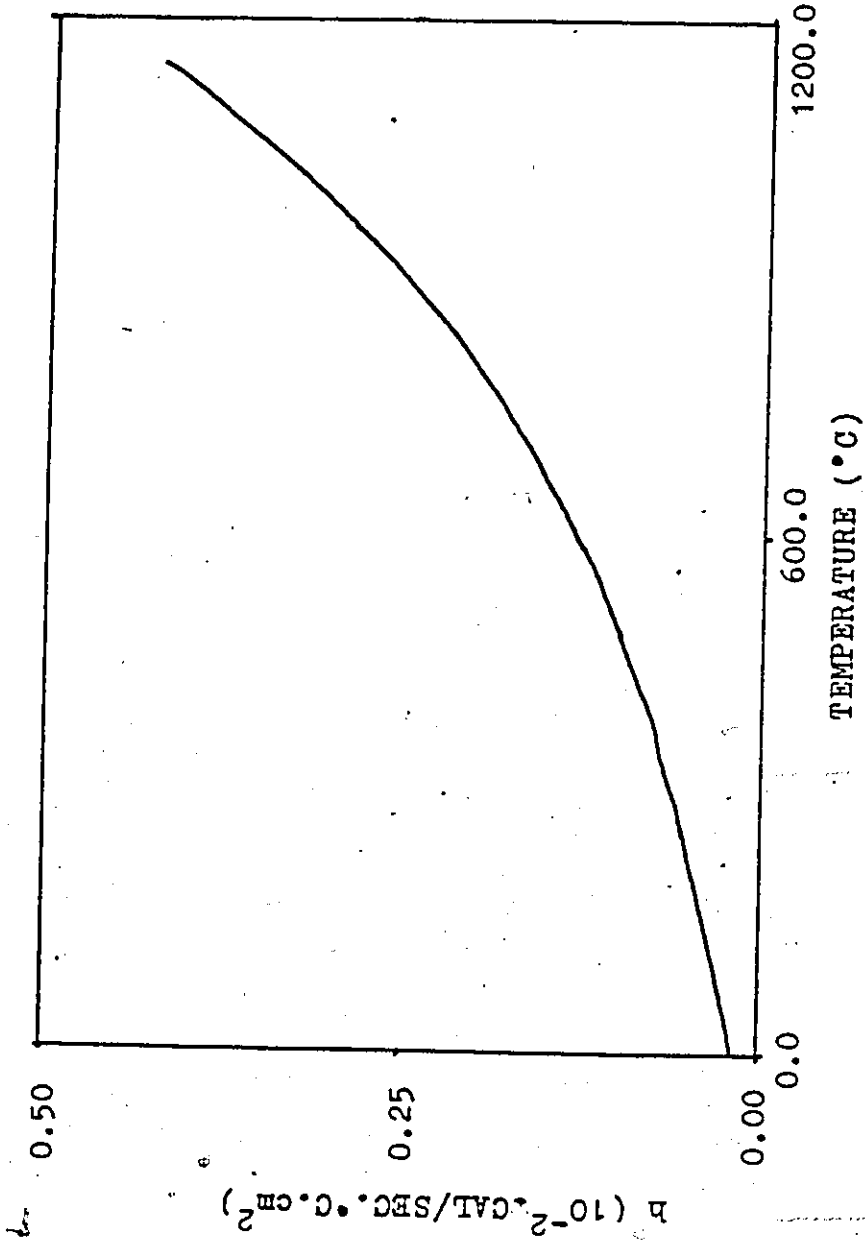


FIG. 2.8 SURFACE COEFFICIENT OF HEAT TRANSFER [9].

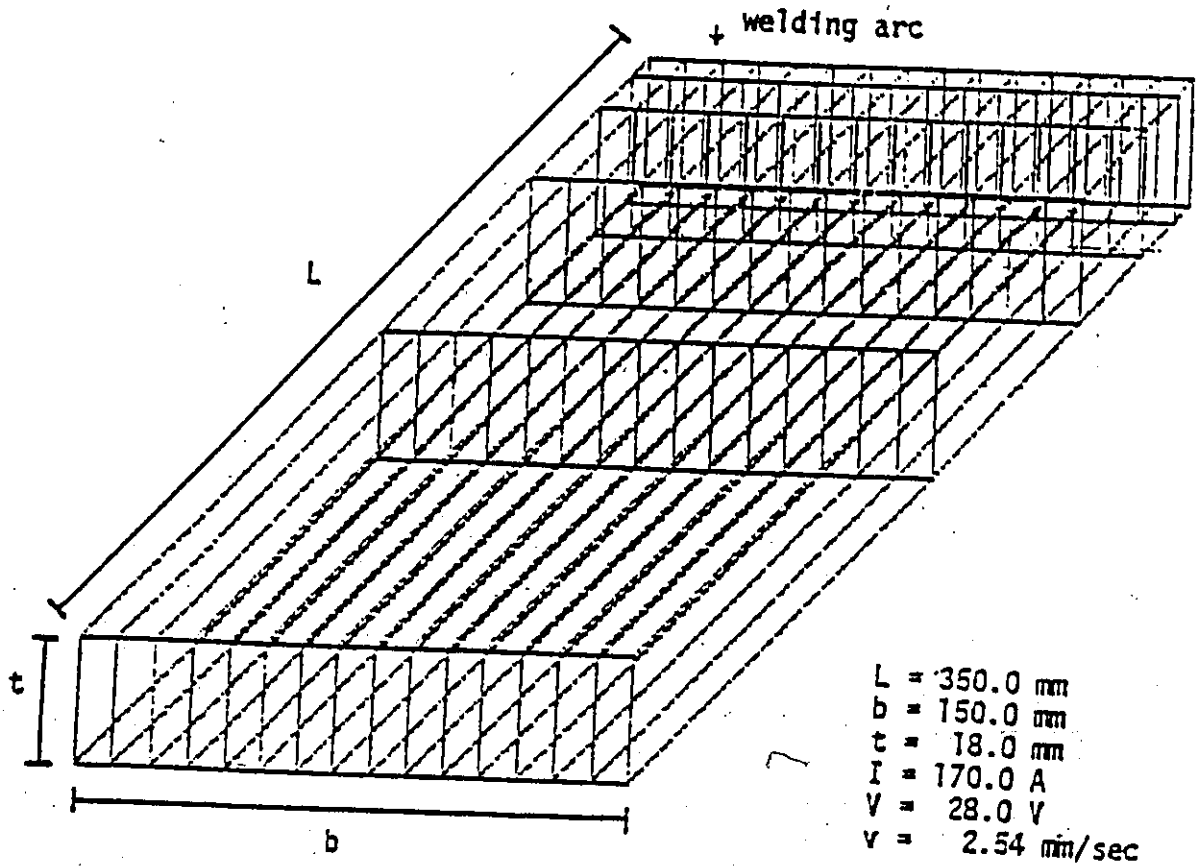


FIG. 2.9 GEOMETRY AND MESH PATTERN OF THE SPECIMEN, AND PROPERTIES OF THE WELDING ARC.

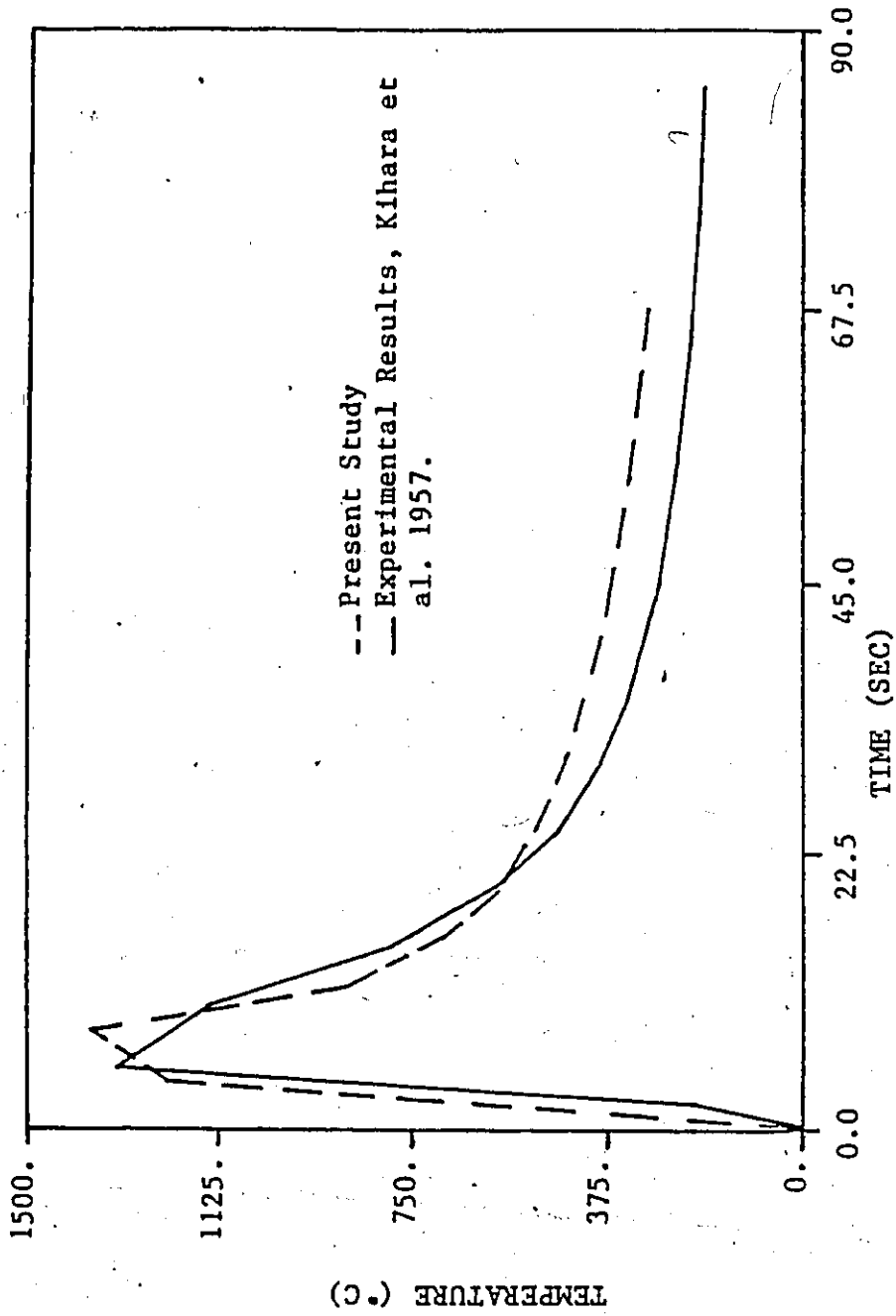


FIG. 2.10 THERMAL CYCLE OF THE HEAT-AFFECTED ZONE OF A BEAD-WELDED SPECIMEN.



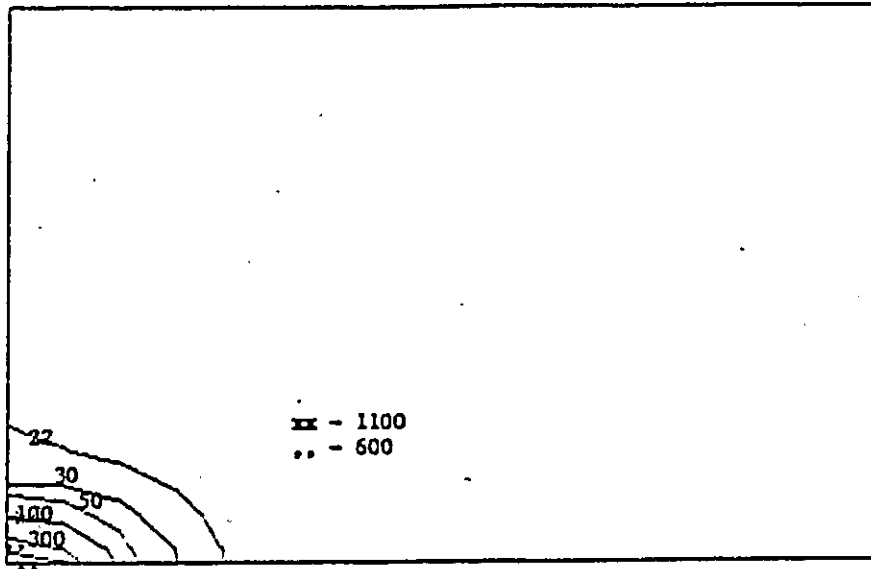


FIG. 2.11 EVOLUTION OF TEMPERATURES ( $^{\circ}$ C) AT  $t=3.94$  sec.

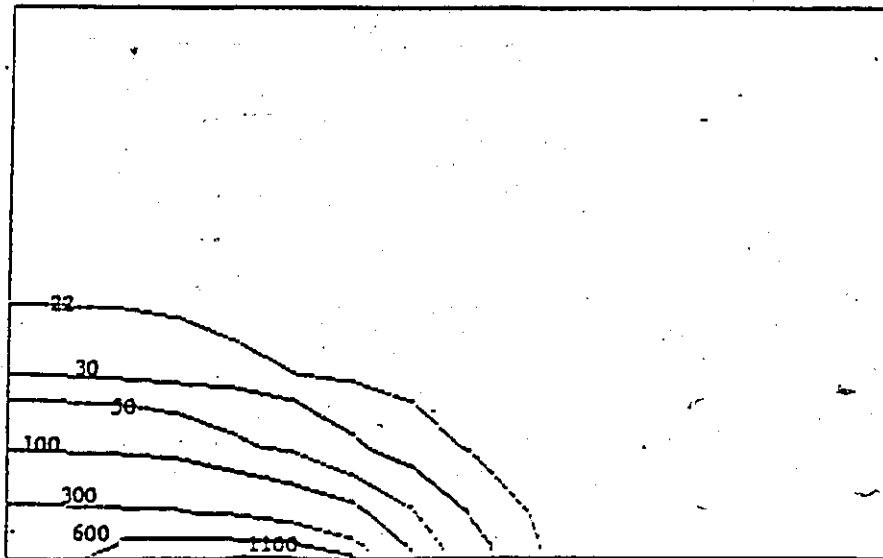


FIG. 2.12 EVOLUTION OF TEMPERATURES ( $^{\circ}$ C) AT  $t=23.62$  sec.

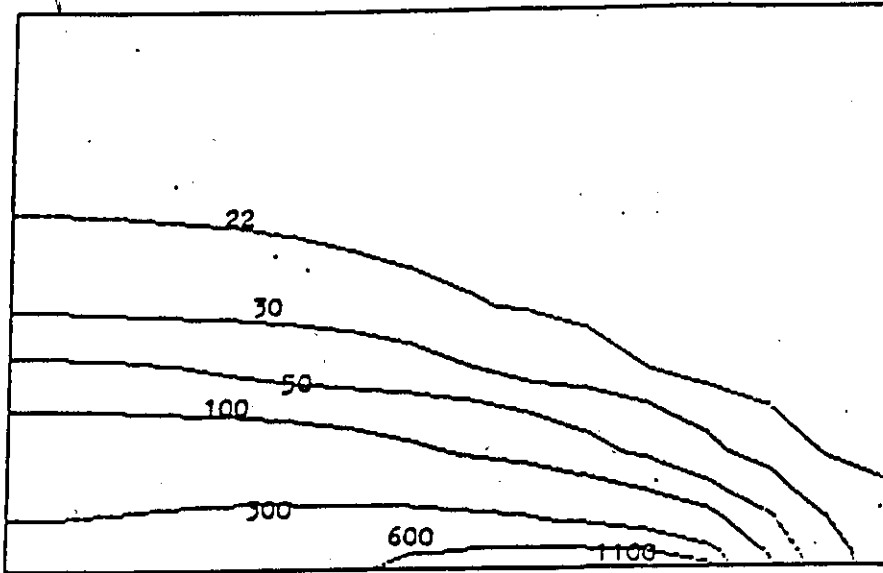


FIG. 2.13 EVOLUTION OF TEMPERATURES ( $^{\circ}\text{C}$ ) AT  $t=47.24$  sec.

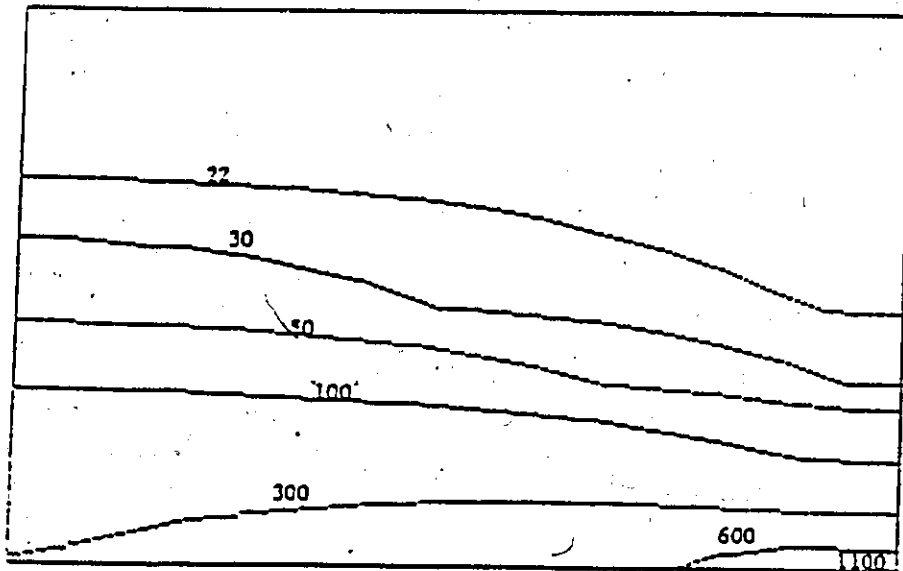


FIG. 2.14 EVOLUTION OF TEMPERATURES ( $^{\circ}\text{C}$ ) AT  $t=66.93$  sec.

## CHAPTER THREE

### MICROSTRUCTURAL ANALYSIS OF AUSTENITIC STEEL

#### 3.1 Introduction

With greater emphasis on the performance of welded structures, there is a need to relate the changes in microstructure to the overall mechanical behaviour. When two steel members are joined by fusion they are subjected to a localized rapid heating and rapid cooling which alters the original microstructural composition of the material. The most affected zone by this process is very close to the weld and is referred to as the heat affected zone (HAZ).

The heat affected zone is a small volume but happens to be the most critical when considering failures. It is composed of different zones as illustrated in figure 3.1, of which the most critical is the grain growth zone. The complexity of the heat affected zone depends mainly on the type of material being welded. To simplify the analysis, only the austenitic stainless steel is considered in this study. During a welding thermal cycle, austenitic stainless steel does not undergo a phase change, and this choice therefore eliminates the recrystallization process. In this case the heat affected zone is made up mainly of the grain growth zone and only modelling of austenite grain growth needs to be considered. However, the model is formulated in such a way so that an extension to involve recrystallization (ferritic steel) is possible.

A mathematical model has been developed to predict the metallurgical changes that occur in austenitic stainless steel due to a welding thermal cycle. Previously, Ashby and Easterling [6] have computed the dissolution temperature of carbides/nitrides based on the metallic and non-metallic composition of the material. They had assumed that the pinning force, which tends to dissolve as the temperature is raised, remains large until the carbides dissolve completely after which it drops to zero. In this study, the suggested model calculates the austenite grain growth according to the value of the pinning force as will be illustrated in this chapter.

### 3.2 Grain Growth

The kinetics of grain growth has been detailed in many textbooks [23] and will not be presented in this thesis. According to Ashby and Easterling [6], the rate of change in the austenite grain size can be approximated by the following equation

$$\frac{d\phi}{dt} = A f(\phi) \exp - \frac{Q}{RT} \quad (3.1)$$

where

- $\phi$  = grain size,
- $f(\phi)$  =  $1/\phi$
- $Q$  = activation energy for grain growth (J/mol),
- $R$  = gas constant,
- $T$  = absolute temperature ( $^{\circ}$ K).

This equation is based on a model which assumes that grain growth is diffusion controlled and that it is driven by the reduction in grain boundary energy. However, it was originally pointed out by Zener [23] that grain boundaries would be held back or pinned by the presence of a second phase inclusion. This force is referred to as the pinning force  $P_A$ . It can be approximated by the following equation if the volume fraction of particles is  $f_v$ , and these are assumed to have the same radius  $r$  and randomly dispersed

$$P_A = \frac{3f_v \sigma_b}{2r} \quad (3.2)$$

where  $\sigma_b$  = grain boundary tension.

To compensate for the pinning of carbides/nitrides, Equation 3.1 is modified to the following form:

$$\frac{d\phi}{dt} = A\{f(\phi) - P[T(t)]\} \exp - \frac{Q}{RT} \quad (3.3)$$

Here  $A$  is referred to as a kinetic constant and can be approximated by the following relation

$$A = 2\sigma_b \Omega \quad (3.4)$$

where  $\Omega$  is the atomic volume and  $P[T(t)]$  the pinning force, and is given by

$$P[T(t)] = \frac{P_A}{\sigma_b} \quad (3.5)$$

In order to calculate the austenite grain growth given by Equation 3.3, one needs to re-express the pinning force as described in the next section.

### 3.3 Pinning Force / Carbide or Nitride Dissolution

The pinning force as given in Equation 3.5 can be rewritten as

$$P[T(t)] = \frac{3f_v}{2r} \quad (3.6)$$

which can be further simplified by assuming that the number of particles per unit volume  $N_v$  remains constant. Then

$$f_v = N_v \frac{4}{3} \pi r^3 \quad (3.7)$$

from which, one can write the radius  $r$  as a function of the volume fraction  $f_v$ . This yields

$$r = \left[ \frac{3 f_v}{4 \pi N_v} \right]^{1/3} \quad (3.8)$$

Substituting Equation 3.8 into Equation 3.6 yields

$$\mathcal{P}[T(t)] = \frac{1}{2}(3f_v)^{2/3}(4\pi N_v)^{1/3} \quad (3.9)$$

This implies that a rate function, which includes the volume fraction and temperature, is required in order to calculate the changes in the pinning force and subsequently the changes in austenite grain sizes. A suitable relation has been proposed by Avrami [18] and is discussed in the next section.

### 3.4 Volume Fraction

Avrami suggested that the dissolution of particles by diffusion could be described by the following relation

$$f_v = f_{v0} \exp - \left[ \frac{(6Dt)^{3/2}}{l^3} \right] \quad (3.10)$$

where

$f_{v0}$  = initial volume fraction

$D$  =  $D_0 \exp-(Q/RT)$ , diffusion coefficient for particle dissolution

$t$  = time

$l$  = particle half-spacing.

In order to compute the pinning force a rate equation is needed. This can be obtained from Equation 3.10 by differentiating it with respect to time, i.e.

$$\frac{\partial f_v}{\partial t} = -\frac{3}{2} f_{v0} \frac{(6D)^{3/2}}{\ell^3} t^{1/2} \exp - \left[ \frac{(6Dt)^{3/2}}{\ell^3} \right] \quad (3.11)$$

To reduce Equation 3.11 to a single variable, using Equation 3.10, time  $t$  as a function of the volume fraction can be written as

$$t^{1/2} = \frac{\ell}{\sqrt{6D}} \text{Log}^{1/3} \left( \frac{f_{v0}}{f_v} \right) \quad (3.12)$$

Now substituting for time (as given in Equation 3.12) into Equation 3.11 yields

$$\frac{\partial f_v}{\partial t} = \frac{-9D}{\ell^2} f_v \text{Log}^{1/3} \left( \frac{f_{v0}}{f_v} \right). \quad (3.13)$$

Equation 3.13 can be further rearranged to

$$\frac{df_v}{f_v \text{Log}^{1/3} \left( \frac{f_{v0}}{f_v} \right)} = \frac{-9D}{\ell^2} dt. \quad (3.14)$$

After integrating both sides of Equation 3.14 the following expression results

$$f_{v,i+1} = \frac{f_{v0}}{\exp \left[ \frac{6D(t^{i+1} - t^i)}{\ell^2} + \text{Log}^{2/3} \frac{f_{v0}}{f_{v,i}} \right]^{3/2}} \quad (3.15)$$



Incremental changes in the volume fraction due to the welding thermal cycle (time and temperature) can now be computed using Equation 3.15. For isothermal conditions, integration of Equation 3.15 leads to Equation 3.10, as expected (Appendix C).

Having established a relationship between the volume fraction and the welding thermal cycle, it is possible to compute the pinning force as given in Equation 3.9 and consequently the changes in the grain sizes as described in the next section (See Appendix C for a more involved formulation).

### 3.5 Finite Element Formulation for Austenite Grain Growth

Having established a relationship between the welding thermal cycle and the particle volume fraction, it is now possible to approximate the value of the pinning force. Equation 3.3 for the grain growth can now be modified to

$$\frac{d\phi}{dt} = A \left[ \frac{1}{\phi} + B \right] \exp - \frac{Q}{RT} \quad (3.16)$$

where

A = kinetic constant

$$B = -\frac{1}{2} (4\pi N \bar{v})^{1/3} (3f_v)^{2/3}$$

The unknown grain size distribution can also be approximated in a manner similar to the temperature field within a finite element which yields

$$\phi = \sum_i N_i \phi_i \quad (3.17)$$

where  $[N]$  are the same interpolation functions as used for the temperature field (Appendix A).

Equation 3.16 can be rearranged to give

$$\frac{\phi d\phi}{1+B\phi} = A \exp - \frac{Q}{RT} dt. \quad (3.18)$$

This, when integrated exactly, yields

$$\left[ \frac{\phi}{B} - \frac{1}{B^2} \text{Log}(1 + B\phi) \right]_{\phi_i}^{\phi_{i+1}} = A \exp - \frac{Q}{RT} (t^{i+1} - t^i) \quad (3.19)$$

Since Equation 3.19 is nonlinear, the Steffensen Method is adopted to solve for the grain size (See Appendix D). Furthermore, it is found that Equation 3.19 is numerically unstable as the pinning force goes to zero (See Appendix E). To eliminate this problem a condition to check the value of the pinning force is imposed and for small values the grain growth equation becomes

$$\frac{d\phi}{dt} = A \frac{1}{\phi} \exp - \frac{Q}{RT} \quad (3.20)$$

This, after rearrangement and integration yields

$$\frac{\phi^2}{2} \Big|_{\phi_i}^{\phi_{i+1}} = A \cdot \exp - \frac{Q}{RT} (t^{i+1} - t^i) \quad (3.21)$$

The above model has been extensively tested and the results are compared with the experimental data available in the literature. However, it is also found that if the kinetic constant A, instead of being a constant, is written as a function of the peak temperature, the model yields improved results. In the function form this is given by

$$A[T_{\text{Peak Temp}}] = \left( \frac{-7}{200} T_{\text{Peak}} + 49.25 \right) \times 10^{-3} \quad (3.22)$$

and has been obtained by using only two experimental values in a rather random manner.

### 3.6 Numerical Examples

Avrami Equation was first tested to check whether it is capable of predicting the proper volume fraction when subjected to a severe thermal cycle. This was accomplished using controlled heating and cooling cycles as shown in Figure 3.2. The corresponding volume fraction is shown in Figure 3.3. It can be observed from Figure 3.3 that during a slow heating cycle, the volume fraction has completely dissolved before the cooling cycle starts. During a fast heating cycle, the volume fraction has barely dissolved before the cooling cycle starts. This illustrates that Avrami

Equation, employed in this study, is predicting proper changes in the volume fraction.

To test the overall microstructural model, the results from the finite element model are checked with the experimental data given by Ashby and Easterling [6] for austenitic stainless steel 316. In their experiment, Ashby and Easterling used a weld simulator in order to control the heating and cooling rate. To simulate the same thermal cycle, the transient Dirichlet boundary condition was utilized, and a sample of the simulated welding thermal cycle is shown in Figure 3.4. Furthermore, the simulated welding thermal cycle is only applied at the face of the welded element and a proper three-dimensional heat flow analysis is performed on the entire member. The size and mesh pattern of the bar used is shown in Figure 3.5.

To check the stability of the proposed model, the grain size distribution along the bar is studied. As shown in Figure 3.6, it can be observed that the distribution is smooth and that no oscillation takes place. Moreover, from the grain size distribution one can approximately predict the grain growth zone as highlighted in the same figure. As anticipated, the heat affected zone or the grain growth zone is small and varies from 0.7 cm to 2.0 cm depending on the peak temperature and the cooling rate.

Ashby and Easterling [6] measured the grain size for four different peak temperatures and for three different cooling time. The cooling time is defined as the time needed for the specimen to cool from  $800^{\circ}\text{C}$  to  $500^{\circ}\text{C}$  and the peak temperature is defined as the highest temperature that the specimen is subjected to. Their

experimental results, along with their analytical results and the two finite element results from the present study, are shown in Figures 3.7 to 3.10. It can be noted from Figure 3.7 that at one extreme, i.e., at low cooling time and low peak temperature, only the finite element results (A as a function of the peak temperature) are in good agreement with the experimental results. Again at the other extreme, by observing the results in Figure 3.10, it can be deduced that at low cooling rate and high peak temperature, only the finite element model (A as a function of the peak temperature) renders better results. Furthermore, at high peak temperature and high cooling rate, none of the analytical models are capable of predicting the proper grain size as depicted in Figure 3.10. The grain sizes observed in experiments are beyond the solid grain sizes that normally occur and poor performances of the models are thought to be due to the grain growth law employed which is limited to solid grain growth.

By observing the results of Figures 3.7 to 3.10, it can be concluded that all three analytical models have predicted the proper grain sizes. However, one of the advantages of the finite element model is that it is also capable of predicting the grain size distribution along the bar as is shown in Figure 3.6. It is also observed from Figure 3.11 that by increasing the peak temperature, while keeping the same cooling time, the curves follow the same path. When the peak temperature is kept constant, while the cooling time changes, it is observed that the curve drops as the cooling time increases.

In conclusion, the microstructural model predicts proper austenite grain size growth for austenitic stainless steel and therefore is adopted in the overall analy-

sis of weld pieces to determine the total deformations and residual stresses due to the welding thermal cycles.

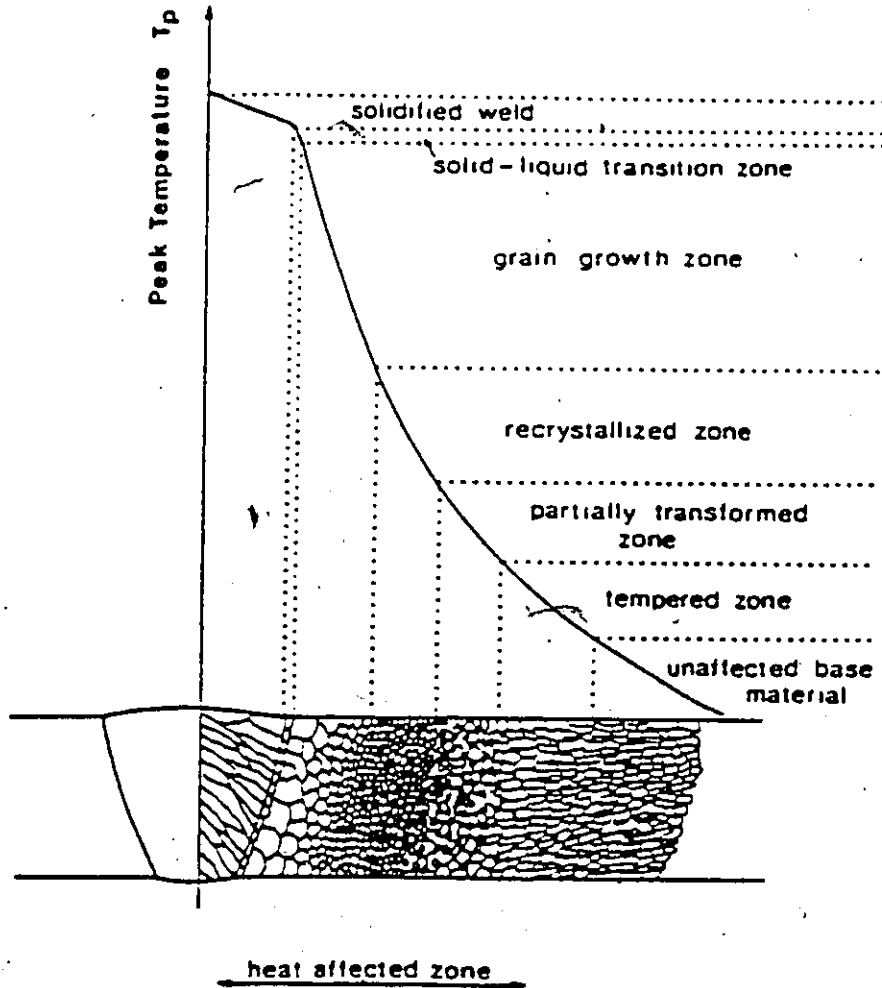


FIG. 3.1 A SCHEMATIC DIAGRAM FOR THE VARIOUS SUB-ZONES OF THE HEAT AFFECTED ZONE [12].

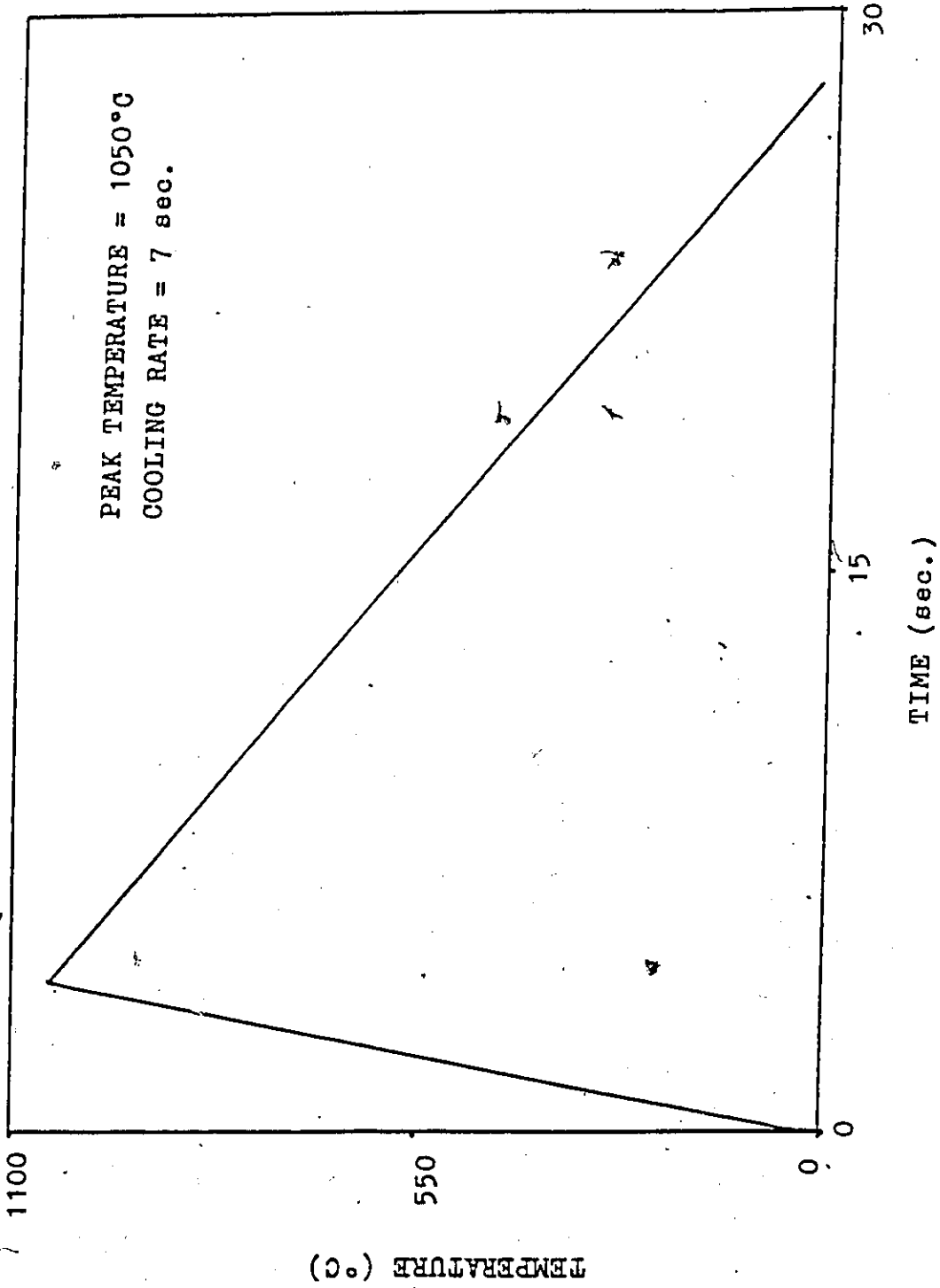


FIG. 3.2 IDEALISED WELD THERMAL CYCLE.



PARTICLE VOLUME FRACTION,  $f_v$

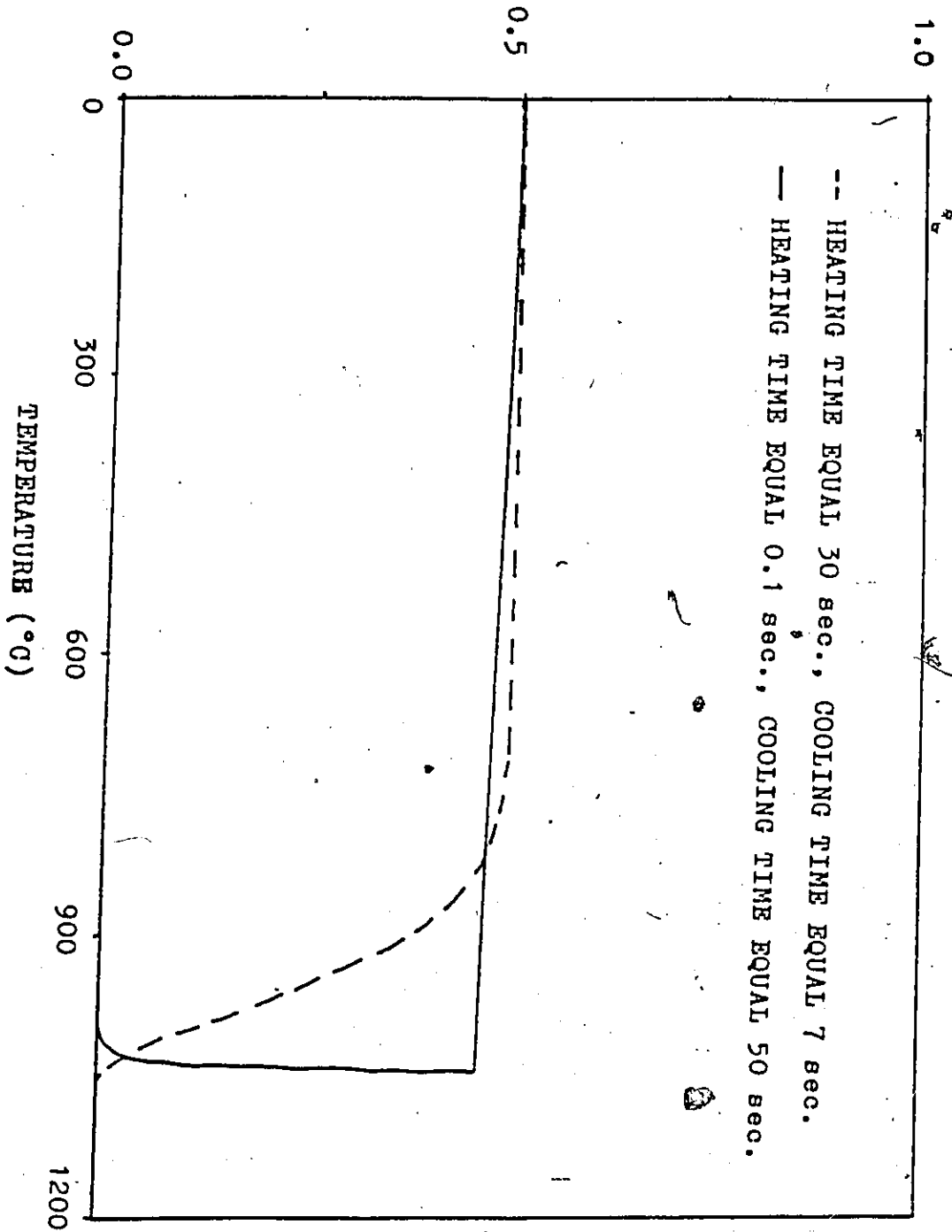


FIG. 3.3 INFLUENCE OF HEATING & COOLING RATE ON PARTICLE VOLUME FRACTION.

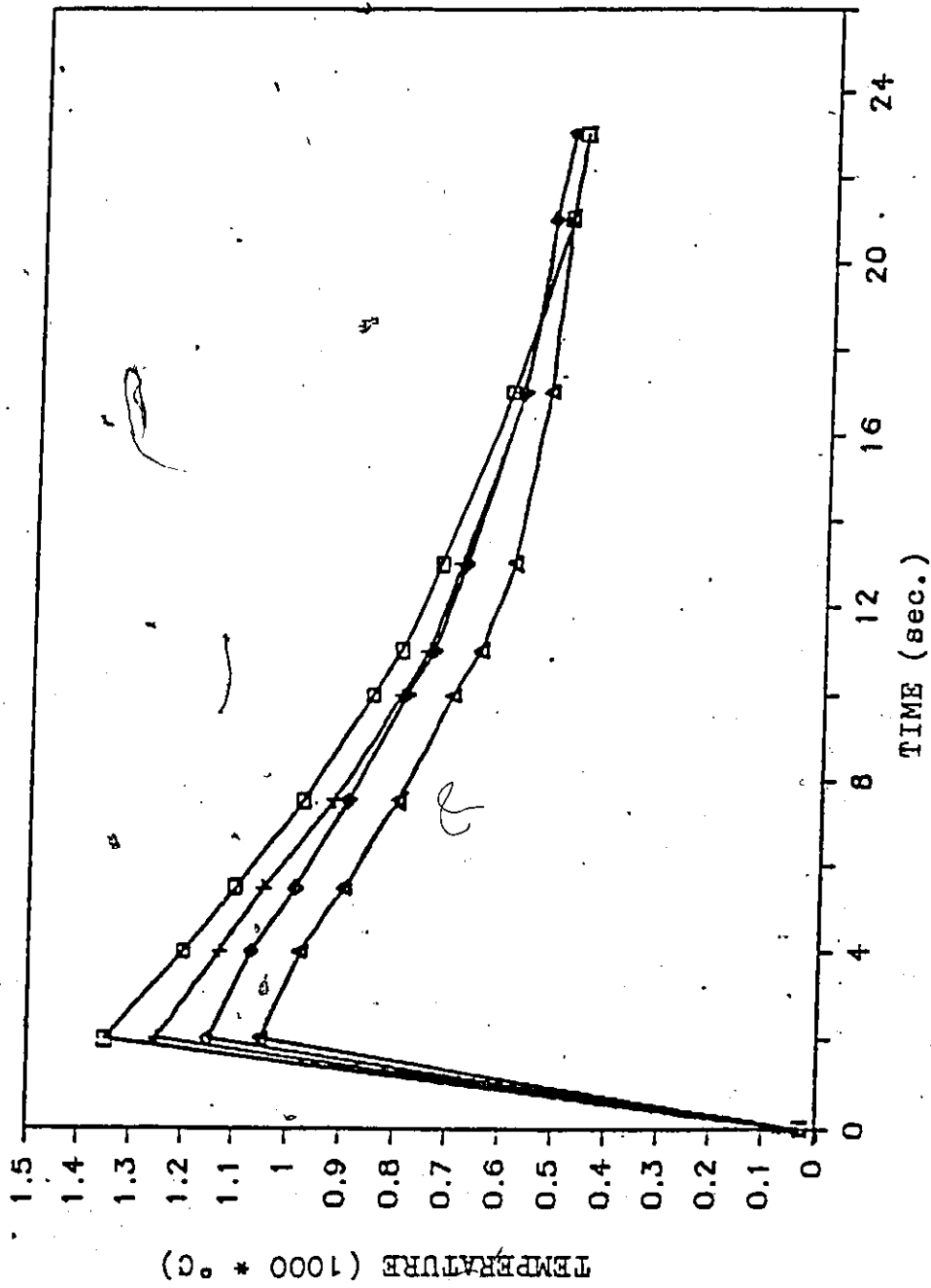


FIG. 3.4 SIMULATED WELDING THERMAL CYCLE

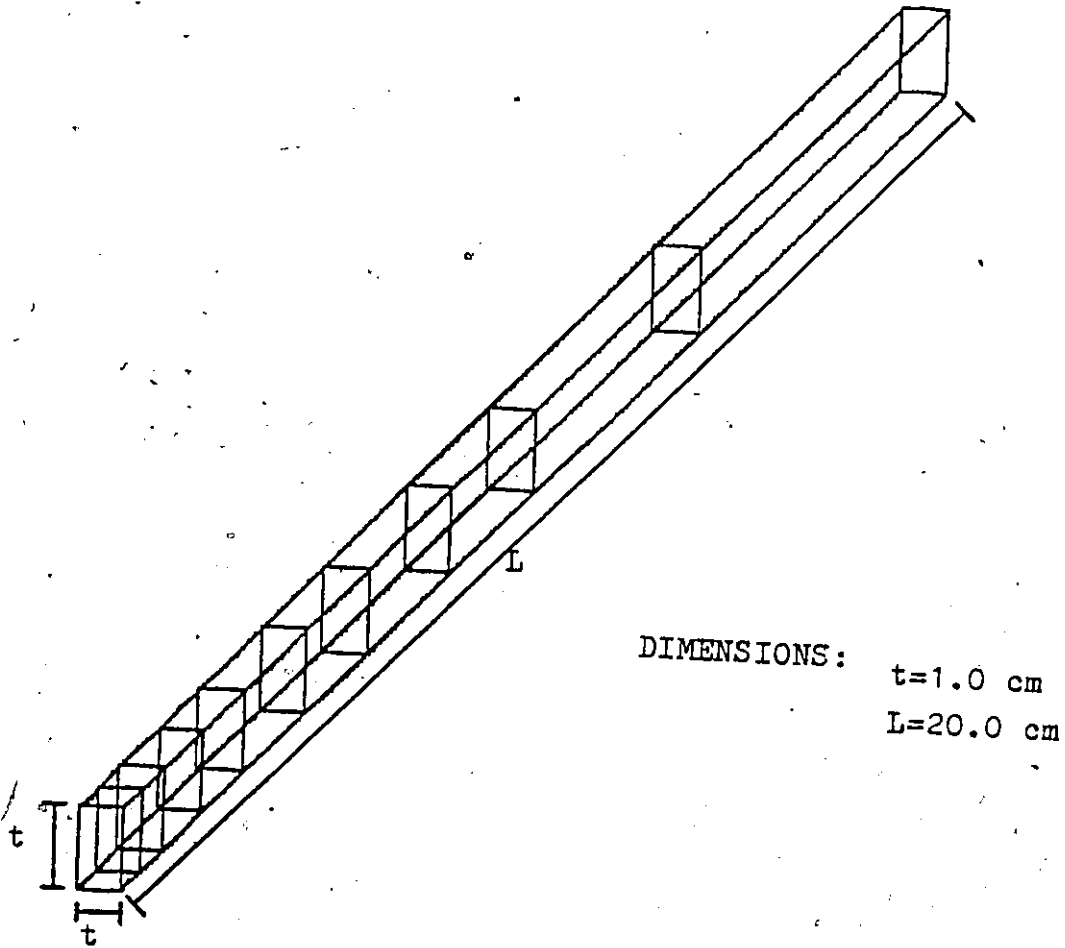


FIG. 3.5 GEOMETRY AND MESH PATTERN USED FOR THE ANALYSIS OF AUSTENITIC STAINLESS STEEL 316.

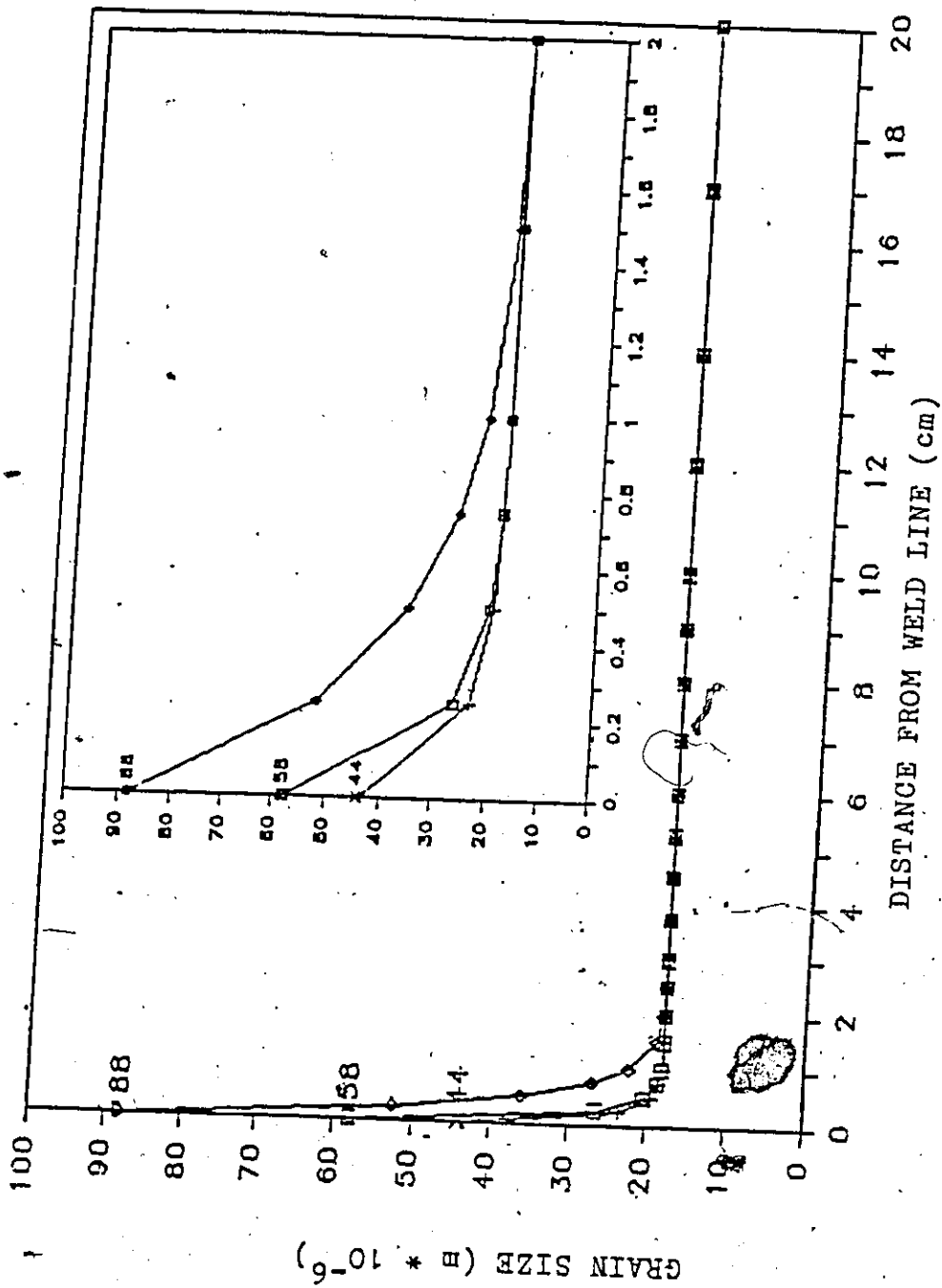


FIG. 3.6 GRAIN SIZE DISTRIBUTION.

B

7

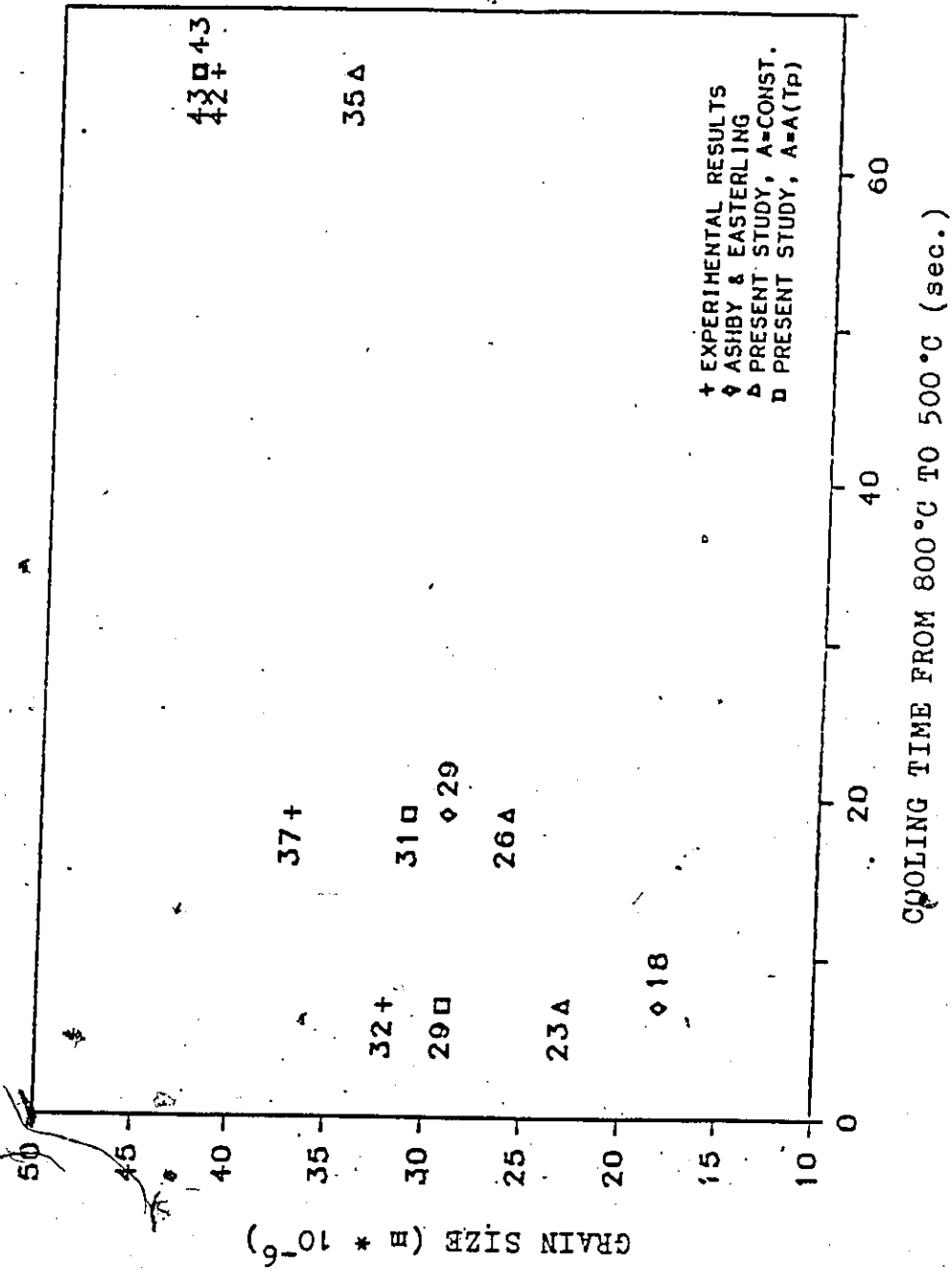


FIG. 3.7 GRAIN GROWTH DIAGRAM FOR A PEAK TEMPERATURE EQUAL 1050°C.

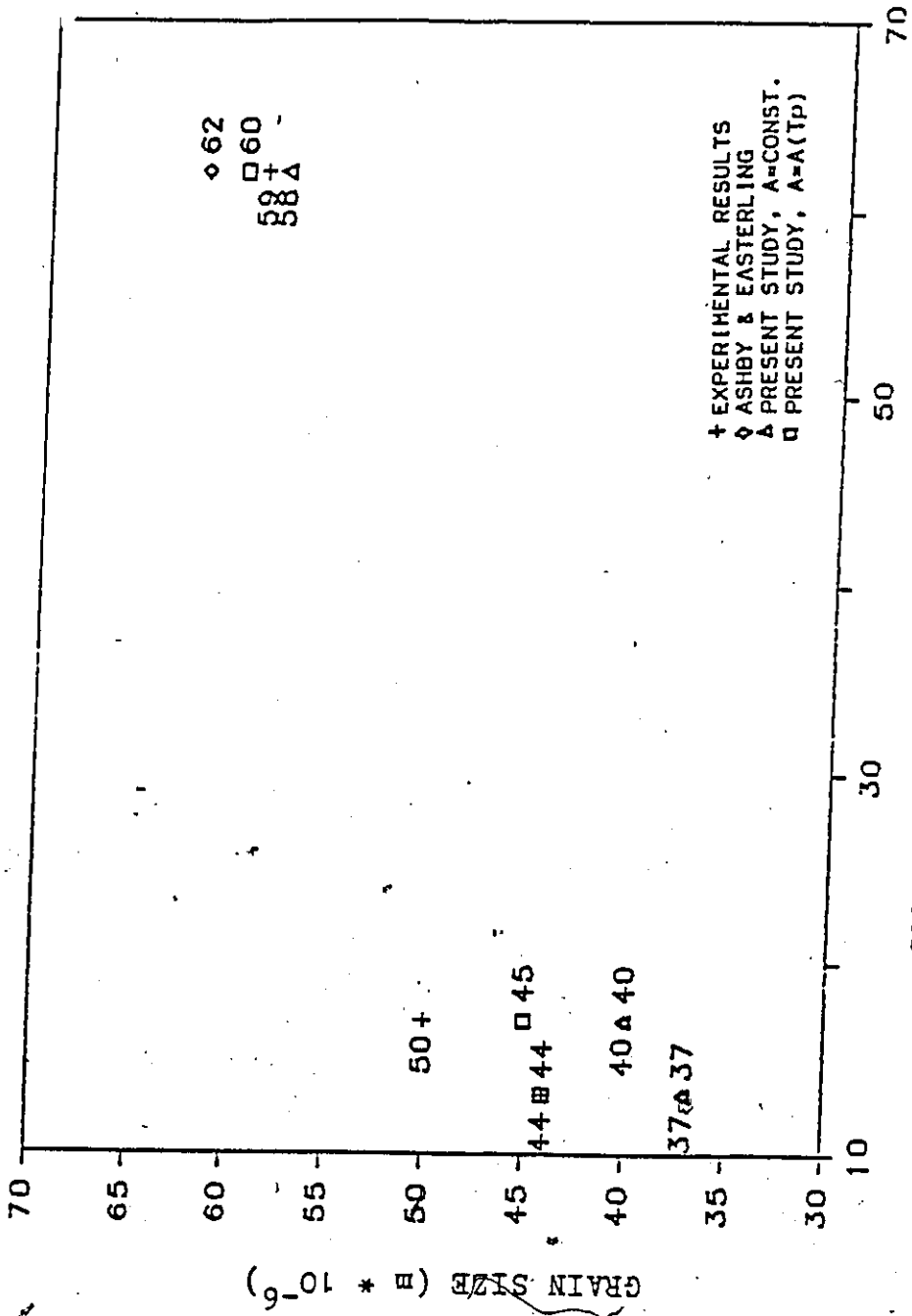


FIG. 3.8 GRAIN GROWTH DIAGRAM FOR A PEAK TEMPERATURE EQUAL 1150°C.

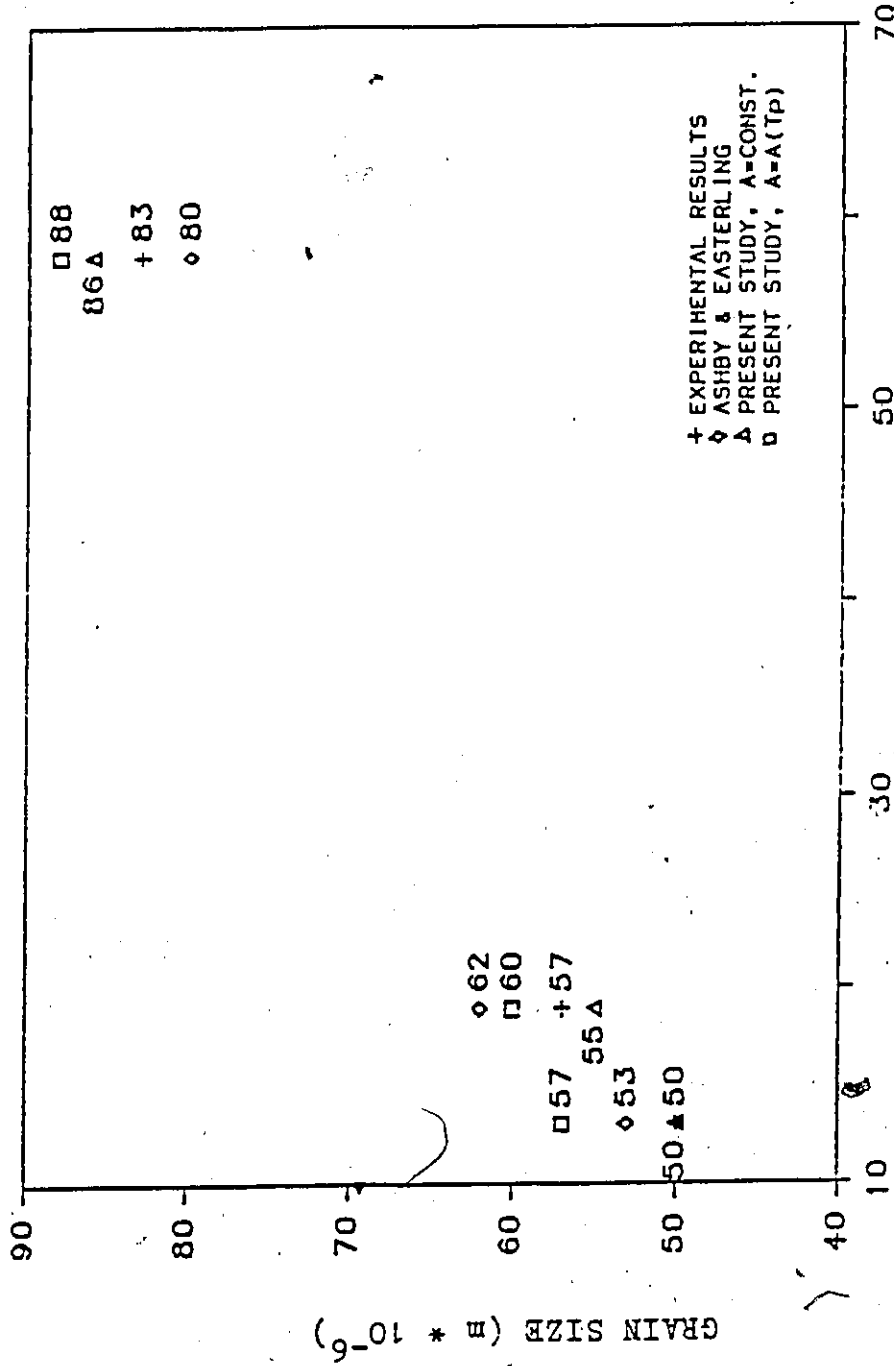


FIG. 3.9 GRAIN GROWTH DIAGRAM FOR A PEAK TEMPERATURE EQUAL 1250°C.  
COOLING TIME FROM 800°C TO 500°C (sec.)

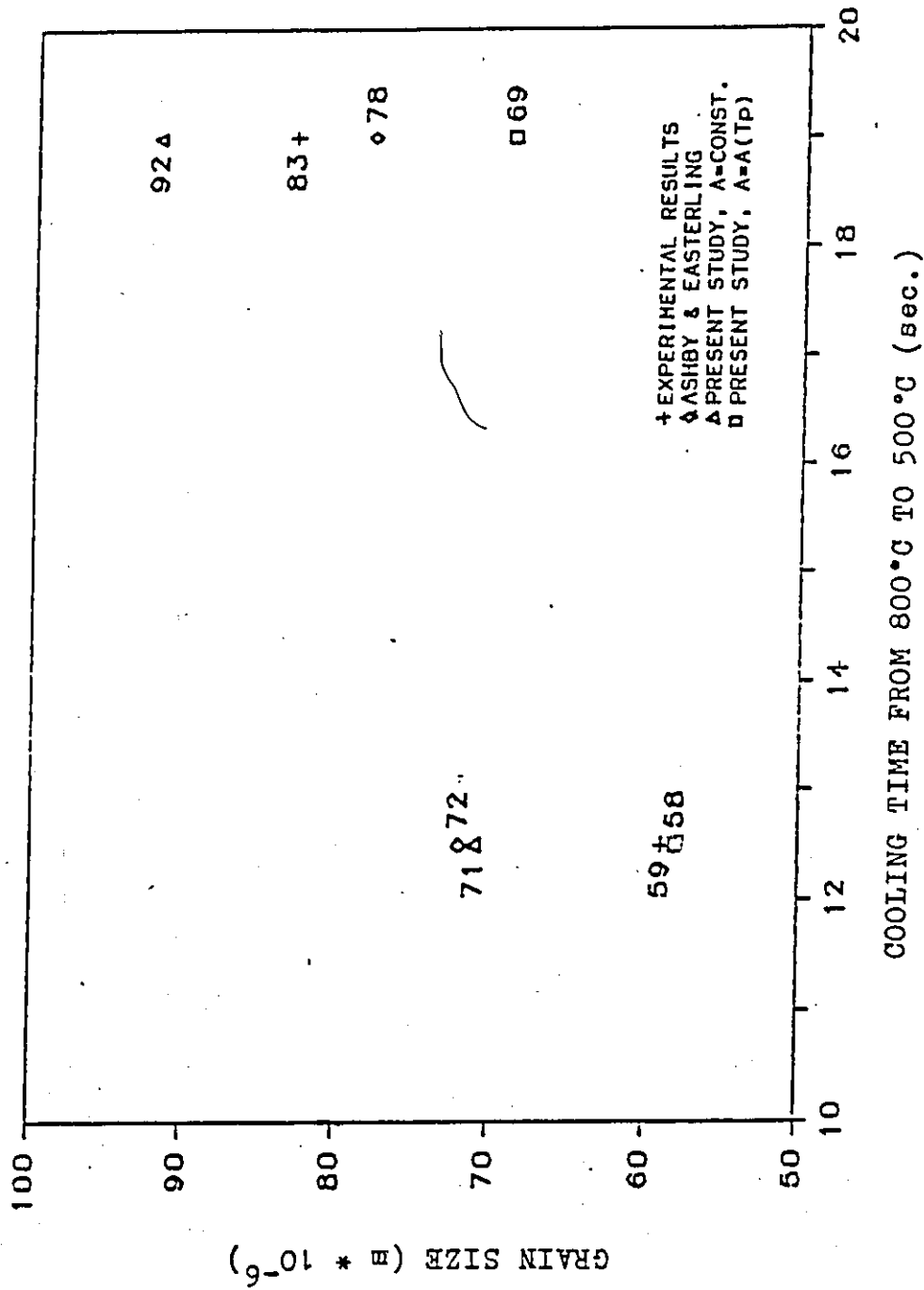


FIG. 3.10 GRAIN GROWTH DIAGRAM FOR A PEAK TEMPERATURE EQUAL 1350°C.



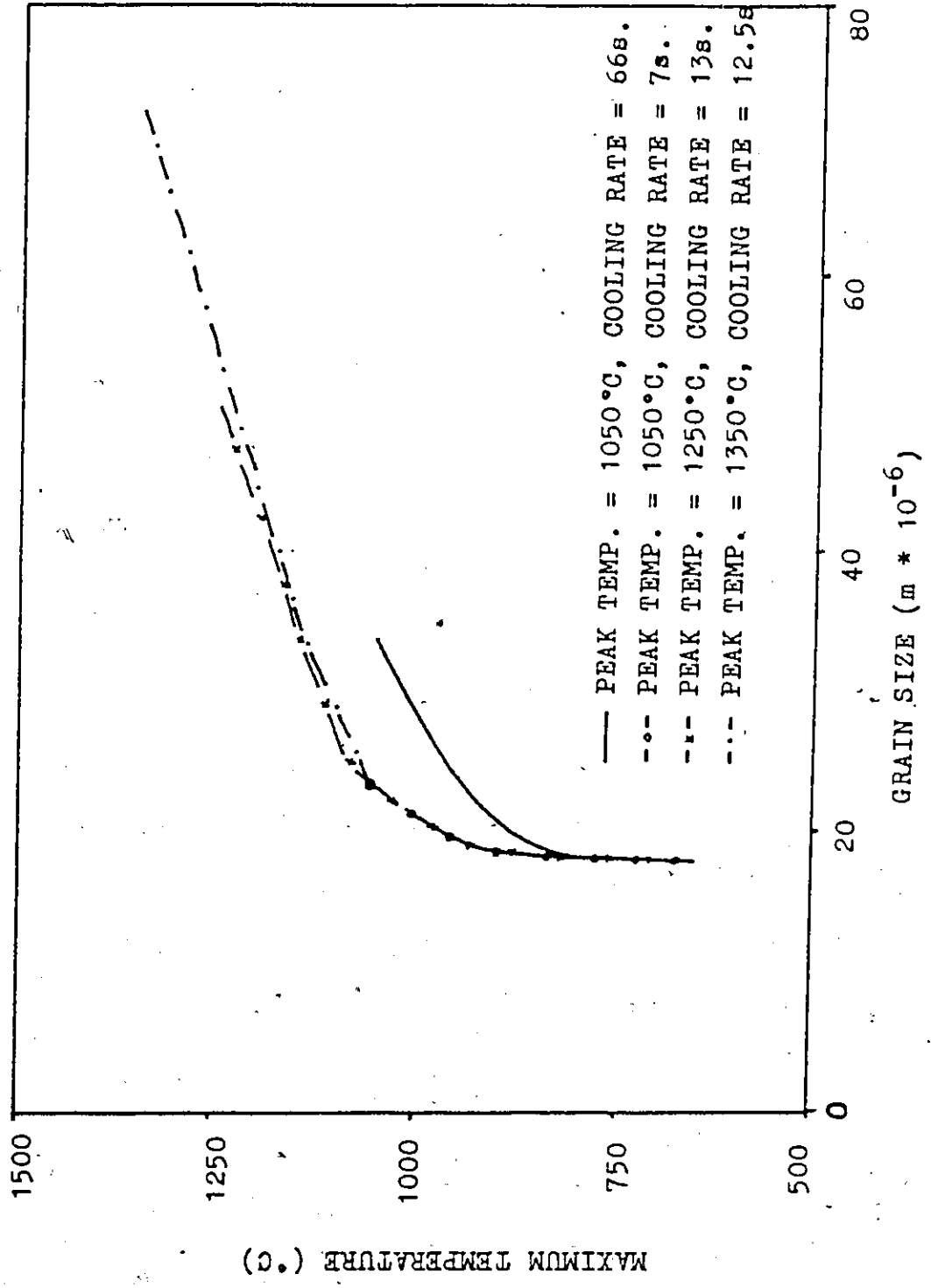


FIG. 3.11 GRAIN SIZE VS. MAXIMUM TEMPERATURE.

## CHAPTER FOUR

# ELASTO-VISCO-PLASTIC FINITE ELEMENT FORMULATION AND APPLICATIONS

### 4.1 Introduction

In reality, continuum mechanics problems have an infinite number of degrees of freedom and frequently have complicated boundary conditions along with non-uniform material properties. These problems are very difficult, if not impossible, to analyze mathematically and one is forced to use numerical techniques. The finite element method, as has been illustrated in chapter two and three, is one of the numerical methods available which discretizes a system into a finite number of degrees of freedom. It is a very powerful analytical tool in the sense that it allows for non-uniform material properties, complicated geometries and boundary conditions.

Because of the complexities involved in loadings, material properties and the boundary conditions which will be present in the analyses of the welded structures, it becomes necessary to employ the finite element method to obtain a reasonable solution. The finite element method proved to be successful in modelling of the welds as reported by Chidiac [11], and is now extended to include the viscous effect which must be taken into account in thermal stress analyses, especially at high temperatures. The nine node isoparametric shell element is employed to model and analyze the thermo-elastic visco-plastic problems. This element, first introduced by

Ahmad et al. [1], is applicable to both thick and thin plates and shells and permits representation of curved boundaries accurately with a minimal computational effort.

Because of the non-linearities involved, once again the principle of virtual work is adopted to obtain the discretized equations of equilibrium. The Newton-Raphson method is used along with the incremental load procedure to solve for the incremental displacements due to thermal changes and the subsequent calculations of strains and stresses for each load level. The displacements are assumed to remain small so as not to significantly alter the original geometry of the structure. The Prandtl-Reuss flow rule and Von-Mises yield criterion have been employed for the visco-plastic analyses. An implicit time stepping formulation is implemented to update the stiffness matrix.

The numerical results for a variety of problems are presented for performance evaluation of the element. These results include elastic, plastic and visco-plastic analyses. Furthermore, the stability and accuracy of the selective integration technique is explored for the non-linear analyses.

#### 4.2 Derivation of Finite Element Equilibrium Equations

In the derivation of the discretized equations of equilibrium, the principle of virtual work has been employed. The equality of the internal virtual work to the external virtual work in going through virtual displacements leads to the following integral equation;

$$\int_V \delta \epsilon_{ij} \sigma_{ij} dV = \int_V \delta u_i f_i dV + \int_S \delta u_i T_i dS \quad (4.1)$$

where

$$\delta \epsilon_{ij} = \delta \{ \epsilon_{xx}, \epsilon_{yy}, \epsilon_{zz}, \epsilon_{xy}, \epsilon_{yz}, \epsilon_{zx} \}, \text{ virtual strains}$$

$$\sigma_{ij} = \{ \sigma_{xx}, \sigma_{yy}, \sigma_{zz}, \sigma_{xy}, \sigma_{yz}, \sigma_{zx} \}, \text{ stress components}$$

$$\delta u_i = \{ \delta U, \delta V, \delta W \}, = \text{virtual displacements}$$

$$f_i = \text{body forces}$$

$$T_i = \text{surface tractions.}$$

The displacements at any point inside a finite element are related to the nodal displacements through the displacement field assumed over the element, and is given by

$$\{u_i\} = [N] \{\delta\} \quad (4.2)$$

where

$$[N] = \text{matrix of shape functions}$$

$$\{\delta\} = \text{nodal displacement degrees of freedom.}$$

Thus, in the absence of initial stresses and initial strains, the stress and strain fields within an element can be obtained in the following manner;

$$\{\epsilon\} = [L]\{U\} = [B]\{\delta\} \quad (4.3)$$

$$\{\sigma\} = [D]\{\epsilon\} = [D][B]\{\delta\} \quad (4.4)$$

where

[B] = strain matrix which relates the nodal displacements to the strain field

[D] = compliance matrix relating strains to stresses.

Substituting Equations 4.2 and 4.3 into Equations 4.1, yields

$$\alpha\{\delta\}^T \left[ \int_V [B]^T [D] [B] dV \right] \{\delta\} = \alpha\{\delta\}^T \left[ \int_V [N]^T \{f\} dV + \int_S [N]^T \{T\} dS \right] \quad (4.5)$$

Since  $\delta\{\delta\}$  is an arbitrary displacement vector, the following discretized equations of equilibrium are obtained;

$$\int_V [B]^T [D] [B] dV \{\delta\} - \int_V [N]^T \{f\} dV + \int_S [N]^T \{T\} dS \quad (4.6)$$

and in matrix form is written as:

$$[K] \{\delta\} = \{F\} \quad (4.7)$$

where the stiffness matrix  $[K]$  is given by

$$[K] = \int_V [B]^T [D] [B] dV \quad (4.8)$$

and the load vector  $\{F\}$  is due to the following;

$$\{F\} = \int_V [N]^T \{f\} dV + \int_S [N]^T \{T\} dS \quad (4.9)$$

### 4.3 Isoparametric Shell Element

The isoparametric shell element, shown in Figure 4.1, was first introduced by Ahmad et al. [1] to avoid numerical difficulties that can be encountered when shells or plates are analysed using a three-dimensional isoparametric element. The formulation of the element has been detailed in previous work [1,11] and only a summary is presented below.

The relationship between the cartesian and the curvilinear coordinates at any point can be written in the following form;

$$\begin{Bmatrix} X \\ Y \\ Z \end{Bmatrix} = \sum_i N_i(\xi, \eta) \frac{(1+\zeta)}{2} \begin{Bmatrix} X \\ Y \\ Z \end{Bmatrix}_{\text{top}} + \sum_i N_i(\xi, \eta) \frac{(1-\zeta)}{2} \begin{Bmatrix} X \\ Y \\ Z \end{Bmatrix}_{\text{bottom}} \quad (4.10)$$

where  $\xi$  and  $\eta$  are the in-plane curvilinear coordinates of the middle surface, and  $\zeta$  is the linear coordinate along the depth of the element. Also,  $N_i$  are the interpolation functions and are listed in Appendix A. A parabolic distribution is employed and is believed to render fairly accurate results. After having established the relationship between the two sets of coordinates, it is convenient to operate with the curvilinear basis.

The shell element under consideration has five degrees of freedom per node, three displacements and two rotations. There are two  $(u, v)$  for in-plane action and three  $(w, \alpha, \beta)$  for out-of-plane action. The element, therefore, has forty five degrees of freedom.

The element displacement field can be written in the form

$$\begin{Bmatrix} U \\ V \\ W \end{Bmatrix} = \sum_i N_i(\xi, \eta) \begin{Bmatrix} U \\ V \\ W \end{Bmatrix} + \sum_i N_i(\xi, \eta) \frac{\zeta}{2} t_i [\Phi] \begin{Bmatrix} \alpha \\ \beta \end{Bmatrix} \quad (4.11)$$

where

$\{U, V, W\}$  = displacement components of the parent element in the global X,

Y, and Z directions

$\{u, v, w, \alpha, \beta\}$  = displacement field at the middle surface of the deformed shell element in the local coordinates system

$[\phi]$  = matrix of directional vectors.

The matrix  $[\phi]$  contains the unit vectors  $\bar{V}_{1i}$  and  $\bar{V}_{2i}$  which, together with the thickness vector  $\bar{V}_{3i}$ , form an orthogonal system [See Appendix B]. The thickness vector is given by

$$\bar{V}_{3i} = \begin{Bmatrix} X \\ Y \\ Z \end{Bmatrix}_{\text{top}} - \begin{Bmatrix} X \\ Y \\ Z \end{Bmatrix}_{\text{bottom}} \quad (4.12)$$

For small deformations, the strain field is given by

$$\begin{Bmatrix} \epsilon_{x'x'} \\ \epsilon_{y'y'} \\ \epsilon_{z'z'} \\ \epsilon_{x'y'} \\ \epsilon_{y'z'} \\ \epsilon_{z'x'} \end{Bmatrix} = \begin{Bmatrix} \frac{\partial u'}{\partial x'} \\ \frac{\partial v'}{\partial y'} \\ \frac{\partial w'}{\partial z'} \\ \frac{\partial u'}{\partial y'} + \frac{\partial v'}{\partial x'} \\ \frac{\partial v'}{\partial z'} + \frac{\partial w'}{\partial y'} \\ \frac{\partial w'}{\partial x'} + \frac{\partial u'}{\partial z'} \end{Bmatrix} \quad (4.13)$$



which after proper manipulations leads to the desired relationship between the displacement degrees of freedom at the nodes and the strains at any point inside the element;

$$\{\epsilon'\} = [B_i][\theta]^T \begin{Bmatrix} U_i \\ V_i \\ W_i \end{Bmatrix} + \frac{t_i}{2} [([B_i] + [C_i])][\theta]^T [\phi] \begin{Bmatrix} \alpha_i \\ \beta_i \end{Bmatrix} \quad (4.14)$$

where

$$[B_i] = \begin{bmatrix} B_1 & 0 & 0 \\ 0 & B_2 & 0 \\ B_2 & B_1 & 0 \\ 0 & 0 & B_1 \\ 0 & 0 & B_2 \end{bmatrix} \quad (4.15a)$$

and

$$B_1 = G_{11} N_{i,\xi} + G_{12} N_{i,\eta}$$

$$B_2 = G_{21} N_{i,\xi} + G_{22} N_{i,\eta}$$

$N_{i,\xi}$  = derivative of  $N_i$  with respect to  $\xi$  and  $i$  is the local element node number;

$$[C_i] = \begin{bmatrix} 0 & 0 & 0 \\ 0 & 0 & 0 \\ 0 & 0 & 0 \\ C_1 & 0 & 0 \\ 0 & C_1 & 0 \end{bmatrix} \quad (4.15b)$$

$$C_1 = G_{33} N_i$$

For more information, refer to Chidiac [11].

After obtaining the strain-displacement relationship above, the stresses can be related to strains using the generalized Hooke's Law in the following manner which also accounts for initial stresses and initial strains;

$$\begin{Bmatrix} \tau_{x'x'} \\ \tau_{y'y'} \\ \tau_{z'z'} \\ \tau_{x'y'} \\ \tau_{y'z'} \\ \tau_{z'x'} \end{Bmatrix} = [D] \left[ \{\epsilon'\} - \{\epsilon_0'\} \right] + \{\sigma_0'\} \quad (4.16)$$

where

$\{\epsilon_0'\}$  = initial strains

$\{\sigma_0\}$  = initial stresses

$[D]$  = elasticity matrix.

The elasticity matrix  $[D]$  is given by

$$[D] = \frac{E}{1-\nu^2} \begin{bmatrix} 1 & & & & & \\ \nu & 1 & & & & \\ 0 & 0 & 0 & & & \\ 0 & 0 & 0 & \frac{1-\nu}{2} & & \\ 0 & 0 & 0 & 0 & \frac{1-\nu}{2K} & \\ 0 & 0 & 0 & 0 & 0 & \frac{1-\nu}{2K} \end{bmatrix} \quad (4.17)$$

In Equation 4.18, E and  $\nu$  are modulus of elasticity and Poisson's ratio, respectively. The linear displacements across the depth of a plate or shell result in constant transverse shear strain. However, this distribution is known to be nearly parabolic. To compensate for this, the factor K has been included in Equation 4.18 above. The value of k is taken to be 1.2, which is the ratio of the maximum to the average shear strain energy.

Both the stiffness matrix in Equation 4.8, and the load vector in Equation 4.9, because of the complexities of the integrands, require numerical integration over the volume of an element. The Gaussian-quadrature scheme is used with three

integration points in each of the three directions. It is pointed that for elastic analyses, only two integration points are needed along the depth in order to integrate exactly.

The numerical analogue for integration in Equation 4.8, using the jacobian transformation, takes the following form

$$[K] = \int_{-1}^{+1} \int_{-1}^{+1} \int_{-1}^{+1} [B]^T [D] [B] \|J\| d\xi d\eta d\zeta \quad (4.18)$$

where the jacobian matrix is given by

$$[J] = \begin{bmatrix} \frac{\partial x}{\partial \xi} & \frac{\partial y}{\partial \xi} & \frac{\partial z}{\partial \xi} \\ \frac{\partial x}{\partial \eta} & \frac{\partial y}{\partial \eta} & \frac{\partial z}{\partial \eta} \\ \frac{\partial x}{\partial \zeta} & \frac{\partial y}{\partial \zeta} & \frac{\partial z}{\partial \zeta} \end{bmatrix} \quad (4.19)$$

and the determinant of the jacobian matrix is given by

$$\|J\| = \frac{\partial(x, y, z)}{\partial(\xi, \eta, \zeta)} \quad (4.20)$$

The weighted functions and the locations of the numerical integration points employed are listed in Table 4.1.

#### 4.4 Constitutive Equations for Elasto-Plastic Analysis

Based on the experimental evidence as reported in the literature, a bilinear stress-strain curve has been adopted for the elasto-plastic material behaviour that has a linear strain hardening branch. Moreover, to perform plastic analysis, a yield surface  $F$  must be defined so that the stresses have to satisfy the following criterion

$$F(\sigma, K) = 0 \quad (4.21)$$

Equation 4.21 states that  $F$  is a function of both the stresses and strain hardening and at the same time dictates that no plastic deformations will take place as long as  $F$  is less than zero. For  $F$  equal to zero, plastic deformations may occur, in which case continuation of the initial elastic behaviour is no longer valid.

There are many valid yield criteria that are applicable to metals. The Von-Mises criterion with an associated flow rule is adopted for this study. By restricting the analysis to associated flow rule, the plastic strain increments are defined by

$$d\epsilon^P = \lambda \frac{\partial F}{\partial \sigma} \quad (4.22)$$

According to the Prandtl-Reuss flow rule, the total strain increment is given by

$$d\epsilon = d\epsilon^e + d\epsilon^p \quad (4.23)$$

The relation between the elastic strain increment  $\{d\epsilon^e\}$  and the stress increment  $\{d\sigma\}$  can be written as

$$\{d\epsilon^e\} = [D]^{-1} \{d\sigma\} \quad (4.24)$$

Substituting of Equations 4.22 and 4.24 into Equation 4.23 gives the total strain increments as

$$\{d\epsilon\} = [D]^{-1} \{d\sigma\} + \lambda \left\{ \frac{\partial F}{\partial \sigma} \right\} \quad (4.25)$$

For plasticity to occur, Equation 4.21 must be satisfied, this yields

$$dF = \sum_i \frac{\partial F}{\partial \sigma_i} d\sigma_i + \frac{\partial F}{\partial K} dK = \left\{ \frac{\partial F}{\partial \sigma} \right\}^T \{d\sigma\} + A\lambda = 0 \quad (4.26)$$

where  $A = -\frac{\partial F}{\partial K} dK \cdot \frac{1}{\lambda}$  (4.27)

The parameter A is equal to the strain hardening modulus  $H'$ , i.e. the slope of the effective stress plastic strain curve

$$A = H' = \frac{d\bar{\sigma}}{d\bar{\epsilon}^p} = \frac{E \cdot E_T}{E - E_T} \quad (4.28)$$

Where  $E_T$  is the tangent modulus. In matrix form, one can write Equations 4.25 and 4.26 as

$$\begin{Bmatrix} d\epsilon \\ 0 \end{Bmatrix} = \begin{bmatrix} D^{-1} & \left\{ \frac{\partial F}{\partial \sigma} \right\} \\ \left\{ \frac{\partial F}{\partial \sigma} \right\}^T & -A \end{bmatrix} \begin{Bmatrix} d\sigma \\ \lambda \end{Bmatrix} \quad (4.29)$$

In order to determine the elasto-plastic stress strain relationship of the following form

$$\{d\sigma\} = [D_{ep}] \{d\epsilon\} \quad (4.30)$$

from Equation 4.29, first multiply the first set of Equation 4.29 by  $\left\{ \frac{\partial F}{\partial \sigma} \right\}^T [D]$  to obtain

$$\begin{aligned} \left\{ \frac{\partial F}{\partial \sigma} \right\}^T [D] \{d\epsilon\} &= \left\{ \frac{\partial F}{\partial \sigma} \right\}^T \{d\sigma\} + \left\{ \frac{\partial F}{\partial \sigma} \right\}^T [D] \left\{ \frac{\partial F}{\partial \sigma} \right\} \lambda \\ \Rightarrow \left\{ \frac{\partial F}{\partial \sigma} \right\}^T \{d\sigma\} &= \left\{ \frac{\partial F}{\partial \sigma} \right\}^T [D] \{d\epsilon\} - \left\{ \frac{\partial F}{\partial \sigma} \right\}^T [D] \left\{ \frac{\partial F}{\partial \sigma} \right\} \lambda \end{aligned} \quad (4.31)$$

Then substitution of Equation 4.31 into the second set of Equation 4.29 yields

$$\left\{ \frac{\partial F}{\partial \sigma} \right\}^T [D] \{d\epsilon\} - \left\{ \frac{\partial F}{\partial \sigma} \right\}^T [D] \left\{ \frac{\partial F}{\partial \sigma} \right\} \lambda - A \lambda = 0$$

$$\Rightarrow \lambda = \frac{\left\{ \frac{\partial F}{\partial \sigma} \right\}^T [D] \{d\epsilon\}}{\left\{ \frac{\partial F}{\partial \sigma} \right\}^T [D] \left\{ \frac{\partial F}{\partial \sigma} \right\} + A} \quad (4.32)$$

Now expand Equation 4.25 and use Equation 4.32 to obtain

$$\{d\epsilon\} = [D]^{-1} \{d\sigma\} + \frac{\left\{ \frac{\partial F}{\partial \sigma} \right\} \left\{ \frac{\partial F}{\partial \sigma} \right\}^T [D] \{d\epsilon\}}{\left\{ \frac{\partial F}{\partial \sigma} \right\}^T [D] \left\{ \frac{\partial F}{\partial \sigma} \right\} + A} \quad (4.33)$$

Substitute Equation 4.28 into 4.25 to yield

$$\{d\sigma\} = \left[ [D] - \frac{[D] \left\{ \frac{\partial F}{\partial \sigma} \right\} \left\{ \frac{\partial F}{\partial \sigma} \right\}^T [D]}{\left\{ \frac{\partial F}{\partial \sigma} \right\}^T [D] \left\{ \frac{\partial F}{\partial \sigma} \right\} + H} \right] \{d\epsilon\} \quad (4.34)$$

Hence, when the load exceeds the yield limit, the elasto-plastic compliance matrix  $[D_{ep}]$  to be used is given by

$$[D_{ep}] = [D] - [D] \frac{1}{\left\{ \frac{\partial F}{\partial \sigma} \right\}^T [D] \left\{ \frac{\partial F}{\partial \sigma} \right\} + H} \left\{ \frac{\partial F}{\partial \sigma} \right\} \left\{ \frac{\partial F}{\partial \sigma} \right\}^T [D] \quad (4.35)$$



The formulation of the elasto-plastic matrix above and adopted partly for this study was introduced by Yamada et al. [34] and Zienkiewicz et al. [39].

From the Huber-von-Mises yield condition with an associated flow rule, the yield surface is given by

$$F = \sqrt{3J_2} - \sigma_y = \bar{\sigma} - \sigma_y \quad (4.36)$$

$$J_2 = \frac{1}{2} S_{ij} S_{ij} \quad (4.37)$$

where  $J_2$  is the second stress invariant, and  $S_{ij}$  represent the deviatoric stresses.  $\sigma_y$  denotes the uniaxial yielding stress and  $\bar{\sigma}$  represent the effective stress.

Since the material properties used are isotropic, according to the adopted yield criterion, yielding will occur when the effective stress is equal to or greater than the yield stress. Also note that the deviatoric stresses are given by

$$S_{ij} = \sigma_{ij} - \delta_{ij} \sigma_m \quad (4.38)$$

and

$$\sigma_m = \frac{1}{3} \sigma_{ii} = \text{first stress invariant.}$$

After substituting for  $\bar{\sigma}$  in Equation 4.36, the following can be obtained

$$\left\{ \frac{\partial F}{\partial \sigma} \right\}^T = \frac{3}{2\bar{\sigma}} S_{ij} \quad (4.39)$$

Having defined all of the terms, one can now compute the elasto-plastic compliance matrix as given in Equation 4.35. This constitutive equation will be used only when the effective stress at an integration point exceeds the yield stress.

Time-dependent material effects and plastic flow must be taken into account in thermal stress analyses, especially at high temperatures. However, the constitutive relations developed in this section do not take viscous flow into consideration and therefore a viscoplastic formulation is also required and is discussed in Section 4.6. The solution procedure for the elasto-plastic analysis is discussed next.

#### 4.5 Numerical Algorithm for Elasto-Plastic Formulation

For non-linear behaviour, the principle of virtual displacements and the incremental load technique are employed to obtain the discretized equations of equilibrium at each load increment. Within each load increment, the incremental displacements are computed, and then the strains and stresses. When the behaviour becomes non-linear, the Newton-Raphson iterative approach is employed to approach equilibrium. This approach is shown schematically in Figure 4.2.

The following equilibrium equations must be satisfied at any load level,

$$\{\psi(\delta)\} = \int_V [B]^T \{\sigma\} dV - \{R\} = 0 \quad (4.40)$$

where  $\{\psi(\delta)\}$  is the unbalanced load vector or the residual vector and  $\{R\}$  is the

applied load vector. Hence, the residual load vector for the  $m^{\text{th}}$  iteration during the  $n^{\text{th}}$  load increment is computed from

$$\{\psi_n^m\} = \int_V [B]^T \{\sigma_n^m\} dV - \{R_n\} = 0 \quad (4.41)$$

Using the Newton-Raphson iterative approach, the resulting iterative equation is given by

$$\{\psi_n^{m+1}\} = \{\psi_n^m\} + [K_T(\sigma_n^m)] \{\Delta \delta_n^m\} = 0 \quad (4.42)$$

in which  $[K_T(\sigma_n^m)]$  is the tangential stiffness matrix. This matrix is formulated for every element using twenty seven integration points. The elasto-plastic compliance matrix is used for each integration point where the effective stress has exceeded the yield stress.

Having obtained the residual load, the incremental displacements are computed from

$$\{\Delta \delta_n^m\} = -[K_T(\sigma_n^m)]^{-1} \{\psi_n^m\} \quad (4.43)$$

The incremental strains and stresses at any point within an element are then computed from

$$\{\Delta \epsilon_n^m\} = [B] \{\Delta \delta_n^m\} \quad (4.44)$$

$$\{\Delta\sigma_n^m\} = [D_{ep}]\{\Delta\epsilon_n^m\} \quad (4.45)$$

The matrix  $[D_{ep}]$  is the elasticity matrix if no yielding is taking place and the elasto-plastic compliance matrix if yielding has occurred. The strain matrix  $[B]$  needs to be evaluated only once due to the fact that the geometric non-linearities are neglected.

The frontal solution technique, Hinton et al. [16], is adopted to solve the discretized equations of equilibrium. The frontal technique was first introduced by Irons and has since enjoyed wide reputation as being efficient and inexpensive. It is designed to minimize the core storage requirement and the number of arithmetic operations. The algorithm of the method is summarized in Figure 4.3. For more information refer to Hinton et al. [16].

The steps used in the algorithm for non-linear analysis are summarized below.

1. After the Newton-Raphson iterative approach has converged for the  $(n-1)^{th}$  load increment in the  $m^{th}$  iteration, consider  $(\psi_{n-1}^m)$  to be the resulting residual load. After the first iteration for the  $n^{th}$  load increment, the displacement increment is given by

$$[K_T(\sigma_n^0)]\{\Delta\delta_n^1\} = -\{\psi_n^0\} + \{\Delta R_n^1\} \quad (4.46)$$

$$\{\psi_n^0\} - \{\psi_{n-1}^m\}$$

2. The displacements are then updated

$$\{\delta_n^1\} = \{\delta_n^0\} + \{\Delta\delta_n^1\} \quad (4.47)$$

3. From  $\{\Delta\delta_n^1\}$ , the nodal displacements  $\{\Delta\delta_{ne}^1\}$  are extracted and for each element, the following steps are performed;

- a) Compute the incremental strains and stresses,

$$\{\Delta\epsilon_{ne}^1\} = [B]\{\Delta\delta_{ne}^1\} \quad (4.48)$$

$$\{\Delta\sigma_{ne}^1\} = [D_{ep}]\{\Delta\epsilon_{ne}^1\} \quad (4.49)$$

- b) Update both the stresses and strains.

$$\{\epsilon_{ne}^1\} = \{\epsilon_{ne}^0\} + \{\Delta\epsilon_{ne}^1\} \quad (4.50)$$

$$\{\sigma_{ne}^1\} = \{\sigma_{ne}^0\} + \{\Delta\sigma_{ne}^1\} \quad (4.51)$$

- c) Compute the effective stress  $\bar{\sigma}$  in Equation 4.36 to check whether yielding has occurred at the particular integration point. If the effective stress is smaller than, or equal to the yield limit, the elasticity matrix in Equation 4.17 is used; and if

it is greater than the yield stress, the elasto-plastic compliance matrix  $[D_{ep}]$  in Equation 4.35 is used.

d) Compute the new stiffness matrix using Equation 4.18 based on the information in c) above.

e) Compute the residual load vector

$$\begin{aligned} \{\psi_{ne}^1\} &= \{P_{ne}^1\} - \{R_{ne}^1\} \\ &= \int_V [B]^T \{\sigma_{ne}^1\} dV - \{R_{ne}^1\} \end{aligned} \quad (4.52)$$

where  $\{P_{ne}^1\}$  = load due to the internal stresses,

$\{R_{ne}^1\}$  = total external load applied.

f) Solve for the incremental displacement vector.

4. Repeat steps 2 to 3 until the incremental solution has converged within a desired tolerance which is computed by

$$\gamma = \frac{\{\Delta \delta_n^m\}^T \{\psi_n^m\}}{\{\Delta \delta_n^1\}^T \{\psi_n^1\}} \leq \gamma_s \quad (4.53)$$

and

$$\{\psi_n^m\} = \int_V [B]^T \{\sigma_n^m\} dV - \{R_n\}$$

$\{\Delta \delta_n^m\} =$  incremental displacement for the  $m^{\text{th}}$  iteration during the  $n^{\text{th}}$  load increment.

i.e., the internal energy of the  $m^{\text{th}}$  increment (i.e., the amount of work done by the out-of-balance loads on the displacement increments) is compared to the internal energy of the first increment [7].

$\gamma_s$  is the specified value of  $\gamma$  for convergence.

5. Once the condition specified in Equation 4.53 is met, the next load increment is applied.


#### 4.6

#### Constitutive Equations for Elastic Visco-Plastic Analysis

From experimental evidence the viscoplastic strain rates depend not only on the current state of stress but also on the temperature, i.e.

$$\dot{\epsilon}^{VP} = F(\sigma, T) \tag{4.54}$$

In this study, the following visco-plastic rate equation is proposed;


$$\dot{\epsilon}^{VP} = F(\sigma, T, S)$$

(4.55)

where

- $\sigma$  = equivalent stress
- $T$  = temperature
- $S$  = microstructural state.

The function  $F$  in Equation 4.55 is assumed to be a product of three individual functions of single variables, i.e.

$$\dot{\epsilon}^{VP} = F_1(\sigma) F_2(T) F_3(S)$$

(4.56)

For metals, the power law as suggested by Norton has been widely used and thus has been adopted in this study for its simplicity, i.e.

$$F_1(\sigma) = A \sigma^n$$

(4.57)

where  $A$  and  $n$  are material constants. For the temperature function,  $F_2(T)$ , the Arrhenius type expression is used which is fundamental to all thermally activated rate processes, i.e.

$$F_2(T) = \exp - \frac{Q}{RT}$$

(4.58)



where

- Q = activation energy
- R = gas constant
- T = absolute temperature.

For the structure function,  $F_3(S)$ , its influence on the viscoplastic strain rate is not well understood. It has been suggested by Frost and Ashby [15] that either the structure is constant, i.e.

$$F_3(S) = S_0 \quad (4.59)$$

or it is steady state and can be a function of space so

$$F_3(S) = \frac{dS}{dt} = 0 \quad (4.60)$$

Both expressions can be employed to model the effect of microstructure state on the viscoplastic strain rates. In this study, Equation 4.59 is adopted which yields the following viscoplastic strain rate expression;

$$\dot{\epsilon}^{vp} = AS_0^n \exp\left(-\frac{Q}{RT}\right) \quad (4.61)$$

Although the variation in microstructure state (grain size) does not appear to

influence the visco-plastic strain rate explicitly, its effect still indirectly included through the stress field as will be shown in the next chapter.

Now to define the relation between the visco-plastic strain components, Zienkiewics and Corneau [37] have used the classical plasticity theory to define a plastic potential,  $Q(\sigma)$ , and to write as

$$\frac{d}{dt} \epsilon^{vp} = \gamma \langle \phi(F) \rangle \frac{\partial Q}{\partial \sigma} \quad (4.62)$$

in which  $\gamma$  is the fluidity parameter which control the plastic flow rate. Similar to the plastic analysis, visco-plastic flow takes place only if the effective stress is greater than the yield stress and to ensure this the following conditions should be incorporated;

$$\begin{aligned} \langle \phi(F) \rangle &= 0 \quad \text{if } F < 0 \\ \langle \phi(F) \rangle &= \phi(F) \quad \text{if } F \geq 0 \end{aligned} \quad (4.63)$$

In Equation 4.62  $\langle \phi \rangle$  is used to denote a specific function. There exist different choices for function  $F$  for metallic creep, the power law by Norton (Equation 4.57) has been shown to render good results and is introduced in Equation 4.62 in the following manner;

$$\frac{d}{dt} \epsilon^{vp} = \gamma \langle \phi(F^N) \rangle \frac{\partial Q}{\partial \sigma} \quad (4.64)$$

where 
$$F = \frac{(\bar{\sigma} - \sigma_y)}{\sigma_y} = \frac{\sqrt{3J_2} - \sigma_y}{\sigma_y} \quad (4.65)$$

It should be noted that the Von Mises-Huber yield law given in Equation 4.36 is has been incorporated in Equation 4.65. By restricting the analysis to associated flow rule, the components of the visco-plastic strain rate can be expressed as follows

$$\dot{\epsilon}_{ij}^{VP} = \gamma \left\langle \phi \left( \frac{\bar{\sigma} - \sigma_y}{\sigma_y} \right)^n \right\rangle \frac{\partial F}{\partial \sigma_{ij}} \quad (4.66)$$

where

$$\frac{\partial F}{\partial \sigma_{ij}} = \frac{\partial F}{\partial J_2} \frac{\partial J_2}{\partial \sigma_{ij}} = \frac{3}{2\sigma} S_{ij}$$

Therefore, Equation 4.66 becomes

$$\dot{\epsilon}_{ij}^{VP} = \gamma \left\langle \left( \frac{\bar{\sigma} - \sigma_y}{\sigma_y} \right)^n \right\rangle \frac{3}{2\sigma} S_{ij} \quad (4.67)$$

By relating the equivalent viscoplastic strain rate given in Equation 4.67 to the proposed viscoplastic strain rate given in Equation 4.61, one can determine the fluidity parameter. To do this, the effective viscoplastic strain rate is computed as follows;

$$\dot{\epsilon}^{VP} = \sqrt{\frac{2}{3} \dot{\epsilon}_{ij}^{VP} \dot{\epsilon}_{ij}^{VP}} = A S_0 \left( \frac{\bar{\sigma} - \sigma_y}{\sigma_y} \right)^n \exp - \frac{Q}{RT} \quad (4.68)$$

This yields

$$\gamma = A S_0 \exp - \frac{Q}{RT} \quad (4.69)$$

Substituting Equation 4.69 into Equation 4.68 yields

$$\begin{aligned} \dot{\epsilon}_{ij}^{VP} &= A S_0 \exp - \frac{Q}{RT} \left\langle \left( \frac{\bar{\sigma} - \sigma_y}{\sigma_y} \right)^n \right\rangle \frac{3}{2} \frac{1}{\bar{\sigma}} t_{S_{ij}} \\ &= \gamma R_{ijkl} t_{\sigma_{kl}} \end{aligned} \quad (4.70)$$

where

$$t_{\gamma} = A S_0 \exp - \frac{Q}{RT} \left\langle \left( \frac{\bar{\sigma} - \sigma_y}{\sigma_y} \right)^n \right\rangle \frac{3}{2} \frac{1}{\bar{\sigma}} \quad (4.71)$$

$R_{ijkl}$  = constant stress operator matrix and has the following form

$$= \begin{bmatrix} 2/3 & -1/3 & -1/3 & 0 & 0 & 0 \\ & 2/3 & -1/3 & 0 & 0 & 0 \\ & & 2/3 & 0 & 0 & 0 \\ \text{Symmetric} & & & 2 & 0 & 0 \\ & & & & 2 & 0 \\ & & & & & 2 \end{bmatrix} \quad (4.72)$$

With the viscoplastic strain rate stated at time  $t$  above, one can proceed to determine the total strain rate field. Again, using Prandtl-Reuss flow rule, one can write the total strain at time  $t+\Delta t$  as

$$\underline{\epsilon}^{t+\Delta t} = \underline{\epsilon}^{t+\Delta t e} + \underline{\epsilon}^{t+\Delta t VP} + \underline{\epsilon}^{t+\Delta t th} \quad (4.73)$$

where

$$\underline{\epsilon}^{t+\Delta t e} = \text{elastic strain at time } t+\Delta t$$

$$\underline{\epsilon}^{t+\Delta t VP} = \text{viscoplastic strain at time } t+\Delta t$$

$$\underline{\epsilon}^{t+\Delta t th} = \text{thermal strain at time } t+\Delta t$$

$$= \alpha (T^{t+\Delta t} - T^t) \underline{\epsilon}^{th}$$

$t + \Delta t_T$  = temperature at time  $t + \Delta t$ .

The total viscoplastic strain can be expressed as

$$\underline{\epsilon}^{VP}_{t+\Delta t} = \underline{\epsilon}^{VP}_t + \Delta \underline{\epsilon}^{VP} \quad (4.74)$$

where  $\Delta \underline{\epsilon}^{VP}$  is the incremental viscoplastic strain. Using a truncated Taylor's series along with an implicit scheme,  $\Delta \underline{\epsilon}^{VP}$  for the  $k+1$  iteration, can be expressed as follow

$$\Delta \underline{\epsilon}^{VP}_{k+1} = \Delta t_k \left[ \underline{\epsilon}^{VP}_{k+1} + \frac{\partial^{t+\theta \Delta t} \underline{\epsilon}^{VP}_k}{\partial^{t+\Delta t} \sigma_k} \Delta \sigma_k \right] \quad (4.75)$$

where  $\underline{\epsilon}^{VP}_{t+\theta \Delta t}$  is expanded as given below

$$\underline{\epsilon}^{VP}_{t+\theta \Delta t} = (1-\theta) \underline{\epsilon}^{VP}_t + \theta \underline{\epsilon}^{VP}_{t+\Delta t} \quad (4.76)$$

and

$$\Delta \sigma_k = \sigma_{k+1} - \sigma_k$$

Having defined the implicit format of the viscoplastic strain increment, one can

determine the second term in Equation 4.75. Since the first part of Equation 4.76 does not vary with the updated stress field, the derivative of Equation 4.76 with respect to  $t+\Delta t_{\sigma}$  yields

$$\begin{aligned} \frac{\partial^{t+\Delta t} \underline{\epsilon}_{vp}}{\partial^{t+\Delta t} \sigma} &= \partial \left[ \frac{\partial^{t+\Delta t} \underline{\epsilon}_{vp}}{\partial^{t+\Delta t} \sigma} \right] \\ &= 0 + \partial \left[ \frac{\partial^{t+\Delta t} \gamma_R}{\partial^{t+\Delta t} \sigma} t+\Delta t_{\sigma} + t+\Delta t \gamma_R \right] \end{aligned} \quad (4.77)$$

The first term of Equation 4.77 is determined as follow

$$\begin{aligned} \frac{\partial^{t+\Delta t} \gamma}{\partial^{t+\Delta t} \sigma} &= \frac{\partial}{\partial^{t+\Delta t} \sigma} \left[ \frac{3}{2} A S_0 \exp - \frac{Q}{RT} \right. \\ &\quad \left. \frac{1}{t+\Delta t_{\sigma}} \left( \frac{t+\Delta t_{\sigma} - t+\Delta t_{\sigma y}}{t+\Delta t_{\sigma y}} \right)^n \right] \\ &= \frac{9}{4} A S_0 \exp - \frac{Q}{RT} \left[ \frac{-1}{(t+\Delta t_{\sigma})^3} \left( \frac{t+\Delta t_{\sigma} - t+\Delta t_{\sigma y}}{t+\Delta t_{\sigma y}} \right)^n \right. \\ &\quad \left. + \frac{n}{t+\Delta t_{\sigma y} (t+\Delta t_{\sigma})^2} \left( \frac{t+\Delta t_{\sigma} - t+\Delta t_{\sigma y}}{t+\Delta t_{\sigma y}} \right)^{n-1} \right] \end{aligned}$$

$$\underline{R}^{t+\Delta t}_{\sigma} \quad (4.78)$$

Substituting the results of Equation 4.78 into Equation 4.77, and then into Equation 4.75, the total viscoplastic strain at time  $t+\Delta t$  can be expressed as follow

$$\begin{aligned} \underline{\epsilon}^{t+\Delta t}_{VP} = \underline{\epsilon}^t_{VP} + \Delta t \left[ (1-\theta) \underline{\epsilon}^t_{VP} + \theta \underline{\epsilon}^{t+\Delta t}_{VP} + \theta \left\{ A S_0 \exp - \frac{Q}{RT} \right. \right. \\ \left. \left. \left[ \frac{1}{(t+\Delta t_{\sigma})^3} \left( \frac{t+\Delta t_{\sigma} - t+\Delta t_{\sigma y}}{t+\Delta t_{\sigma y}} \right)^n + \frac{n}{t+\Delta t_{\sigma y} (t+\Delta t_{\sigma})^2} \right. \right. \right. \\ \left. \left. \left. \left( \frac{t+\Delta t_{\sigma} - t+\Delta t_{\sigma y}}{t+\Delta t_{\sigma y}} \right)^{n-1} \right\} \underline{R}^{t+\Delta t}_{\sigma} \cdot (t+\Delta t_{\sigma} - t_{\sigma}) \right] \quad (4.79) \end{aligned}$$

Rearranging Equation 4.73, the elastic strain can be obtained as follow

$$\underline{\epsilon}^{t+\Delta t}_e = \underline{\epsilon}^{t+\Delta t} - \underline{\epsilon}^{t+\Delta t}_{VP} - \underline{\epsilon}^{t+\Delta t}_{th} \quad (4.80)$$

Now substituting Equation 4.75 into Equation 4.80 and rearranging, the following is obtained

$$\underline{\epsilon}^{t+\Delta t}_{\sigma} = D \underline{\epsilon}^{t+\Delta t}_e = D \left[ \underline{\epsilon}^{t+\Delta t} - \underline{\epsilon}^{t+\Delta t}_{th} - \underline{\epsilon}^{t+\Delta t}_{VP} - \Delta t \theta \underline{\epsilon}^{t+\Delta t}_{VP} - \right]$$



$$\Delta t \frac{\partial^{t+\theta\Delta t} \underline{\underline{\epsilon}}^{vp}}{\partial^{t+\Delta t} \underline{\underline{\sigma}}} \left( {}^{t+\Delta t} \underline{\underline{\sigma}} - {}^t \underline{\underline{\sigma}} \right) \quad (4.81)$$

This implies

$$\begin{aligned} {}^{t+\Delta t} \underline{\underline{\sigma}} (\underline{\underline{I}} + \underline{\underline{D}}^{t+\Delta t} \underline{\underline{M}}) = \underline{\underline{D}} \left[ {}^{t+\Delta t} \underline{\underline{\epsilon}} - {}^{t+\Delta t} \underline{\underline{\epsilon}}^{th} - {}^t \underline{\underline{\epsilon}}^{vp} \right. \\ \left. - \Delta t \frac{\partial^{t+\theta\Delta t} \underline{\underline{\epsilon}}^{vp}}{\partial^{t+\Delta t} \underline{\underline{\sigma}}} + {}^{t+\Delta t} \underline{\underline{M}} \frac{{}^t \underline{\underline{\sigma}}}{\partial^{t+\Delta t} \underline{\underline{\sigma}}} \right] \quad (4.82) \end{aligned}$$

$$\text{Where } \underline{\underline{M}} = \Delta t \frac{\partial^{t+\theta\Delta t} \underline{\underline{\epsilon}}^{vp}}{\partial^{t+\Delta t} \underline{\underline{\sigma}}} \quad (4.83)$$

From Equation 4.82 the viscoplastic compliance matrix can be expressed by the following relation,

$$\underline{\underline{D}}^{vp} = (\underline{\underline{I}} + \underline{\underline{D}}^{t+\Delta t} \underline{\underline{M}})^{-1} \underline{\underline{D}} \quad (4.84)$$

In the thermal stress analysis, one has to determine the updated stress state and the equivalent viscoplastic strain rate as given in Equation 4.70 after a time increment  $\Delta t$ . In order to satisfy Equation 4.70 an iterative approach is implemented using an implicit formulation. The stress field at time  $t+\Delta t$  and for the  $n+1^{\text{th}}$  iteration is given as follow

$$\begin{aligned}
 {}^{t+\Delta t}\sigma_{n+1} = & \underline{D}_n^{vp} \left[ {}^{t+\Delta t}\underline{\epsilon} - {}^{t+\Delta t}\underline{\epsilon}^{th} - {}^t\underline{\epsilon}^{vp} - \Delta t \left\{ (1-\theta) {}^t\underline{\dot{\epsilon}}^{vp} \right. \right. \\
 & \left. \left. + \theta {}^{t+\Delta t}\underline{\dot{\epsilon}}^{vp} - \theta {}^{t+\Delta t}\underline{M}_n \right\} \right] \quad (4.85)
 \end{aligned}$$

which after expansion yields

$$\begin{aligned}
 {}^{t+\Delta t}\sigma_{n+1} = & \underline{D}_n^{vp} \left[ {}^{t+\Delta t}\underline{\epsilon} - {}^{t+\Delta t}\underline{\epsilon}^{th} - {}^t\underline{\epsilon}^{vp} - \Delta t \left\{ (1-\theta) {}^t\underline{\dot{\epsilon}}^{vp} \right. \right. \\
 & \left. \left. + \theta {}^{t+\Delta t}\underline{\dot{\epsilon}}^{vp} - \theta {}^{t+\Delta t}\underline{M}_n \right\} \right] \quad (4.86)
 \end{aligned}$$

The solution procedure for the viscoplastic analysis is discussed in the next section.

#### 4.7 Numerical Algorithm for the Elastic Visco-Plastic Formulation

The essential steps in the solution process are similar to those presented in Section 4.5. The procedure adopted for the viscoplastic analysis is similar to the one presented by Kanchi et al. [20], but has been modified to obtain the updated stress field after each time increment. The algorithm, for updating stresses and strains using the constitutive model presented in Section 4.6, is for use within a load increment. It is now incorporated into the overall finite element modelling using the incremental load procedure.

1. At time  $t$ , the overall equilibrium of the structure is reached where  $\underline{t}_u$ ,  $\underline{t}_\sigma$ ,  $\underline{t}_\epsilon$ ,  $\underline{t}_\epsilon^{vp}$  and  $\underline{t}_R$  are known, the following are then computed;

- a) Using Equation 4.18, compute the stiffness matrix

$$\underline{t}_K = \int_V \underline{B}^T \underline{t}_D^{vp} \underline{B} dV$$

- b) Using Equation 4.70, compute the viscoplastic strain rate

$$\underline{t}_\epsilon^{vp} = \underline{t}_\gamma \underline{R} \underline{t}_\sigma$$

2. The incremental displacement field is computed using the following equation

$$\Delta \underline{t}_u = - \left[ \begin{matrix} \underline{t}_K \\ \underline{t}_T \end{matrix} \right]^{-1} \underline{t}_\psi$$

$$\text{where } \underline{t}_\psi = \int_V \underline{B}^T \underline{t}_\sigma dV - \underline{t} + \Delta \underline{t}_R \quad (4.87)$$

3. From  $\{\Delta \underline{t}_u\}$ , the element nodal displacements  $\{\Delta \underline{t}_\delta_e\}$  are extracted and the following steps are performed:

- a) compute the incremental strains and stresses

$$\Delta^t \underline{\epsilon}_e = \underline{B} \Delta^t \underline{\delta}_e \quad (4.88)$$

$$\Delta^t \underline{\sigma}_e = {}^t \underline{D}^{vp} \Delta^t \underline{\epsilon}_e \quad (4.89)$$

b) update strains and stresses for time  $t+\Delta t$

$${}^{t+\Delta t} \underline{\epsilon}_e = {}^t \underline{\epsilon}_e + \Delta^t \underline{\epsilon}_e \quad (4.90)$$

$${}^{t+\Delta t} \underline{\sigma}_e = {}^t \underline{\sigma}_e + \Delta^t \underline{\sigma}_e \quad (4.91)$$

c) calculate the viscoplastic strain rate according to the updated stress field

$${}^{t+\Delta t} \underline{\dot{\epsilon}}^{vp} = {}^{t+\Delta t} \underline{\gamma} \underline{R} {}^{t+\Delta t} \underline{\sigma} \quad (4.92)$$

d) using the updated viscoplastic strain rate above, recalculate the updated stress field using Equation 4.86.

e) repeat steps c) and d) until the updated stress field and the viscoplastic strain rate correspond to each other.

4. Calculate the unbalanced load vector;

$${}^{t+\Delta t}\underline{\psi} = \int_V \underline{B}^T {}^{t+\Delta t}\underline{\sigma} dV - {}^{t+\Delta t}\underline{R} \quad (4.93)$$

5. Repeat steps 1 to 4 until the incremental solution has converged within a desired tolerance  $\gamma_s$  which is given in Equation 4.54
6. Once the tolerance specified in Equation 4.54 is met, apply the next load increment and repeat all steps 1 to 5 until the entire load history has been achieved. The algorithm presented above is diagrammatically presented in Figure 4.4.

#### 4.8 Numerical Examples

The performances of the nine node isoparametric shell element were tested for both plastic and viscoplastic analyses. Further, the effect of reduced integration scheme beyond the yield limit was explored on both thick and thin plates. Finally the stability of both the implicit and explicit scheme employed for the viscoplastic analysis was explored.

In the first example, the plate was simply supported and subjected to uniform distributed load. The geometry and material properties are given in Figure 4.5. The results were compared to a Heterosis element that employs Mindlin plate theory with both layered and non-layered approach by Owen et al. [28]. The results are shown in Figure 4.6. As can be observed, the element response beyond the elastoplastic range, without the reduced integration, is in good agreement with the results

given by Owen et al. [28]. The reduced integration results in an unacceptably stiffer response beyond the elastic limit.

The results from the nine node shell element were then compared with the nonconforming rectangular, thin plate bending element given by Mirza et al. [25] and Stanton and Schmit [31], for a simply supported square plate under uniform distributed load. The geometry and material properties are shown in Figure 4.7. The results are shown in Figure 4.8. Again, the response, without the reduced integration, is in good agreement with that obtained using the rectangular, plate bending element and an unacceptably stiffer response resulting for the reduced integration beyond the elastic limit. It should be noted that the nine-node isoparametric shell element is a conforming element.

To test the stability and accuracy of the viscoplastic formulation, a statically determinate structure was first analyzed as shown in Figure 4.9. The plate is simply supported on one side and is subjected to a uniform stress field along the opposite side. The material properties are also given in the figure. Only in-plane action was tested and the results for both the implicit and explicit schemes are shown in Figure 4.10. Further, a statically indeterminate structure was also tested and the results were compared to those given by INDAP [13]. The geometry and material properties of the square plate are shown in Figure 4.11. Again, only the in-plane action was tested due to the limitations of INDAP. The results of the explicit scheme are shown in Figure 4.12. The implicit scheme results where  $\theta$  is taken equal to 0.5 are shown in Figure 4.13. These results suggest that the formulation is proper and stable and that the element response is accurate.

In conclusion, the reduced integration technique employed to suppress the shear strain modes is only applicable in the linear elastic range. Due to the poor performance of the nine node, isoparametric shell element beyond the elastic limit, the selective integration is not recommended for an elasto-plastic or a visco-plastic analysis. Based on very good responses for elastic visco-plastic analyses, it is concluded that the isoparametric shell element is acceptable and is adopted for performing thermo-elastic visco-plastic analyses of welded structures.

---

TABLE 4.1  
SAMPLING POINTS AND WEIGHTING FACTORS IN GAUSS-LEGENDRE  
NUMERICAL INTEGRATION

---

Number of Points	Sampling Points	Weighting Factors
2	+ 0.57735 02691 89626	1.00000 00000 00000
	- 0.57735 02691 89262	1.00000 00000 00000
3	+ 0.77459 66692 41483	0.55555 55555 55556
	0.00000 00000 00000	0.88888 88888 88889
	- 0.77459 66692 41483	0.55555 55555 55556

---



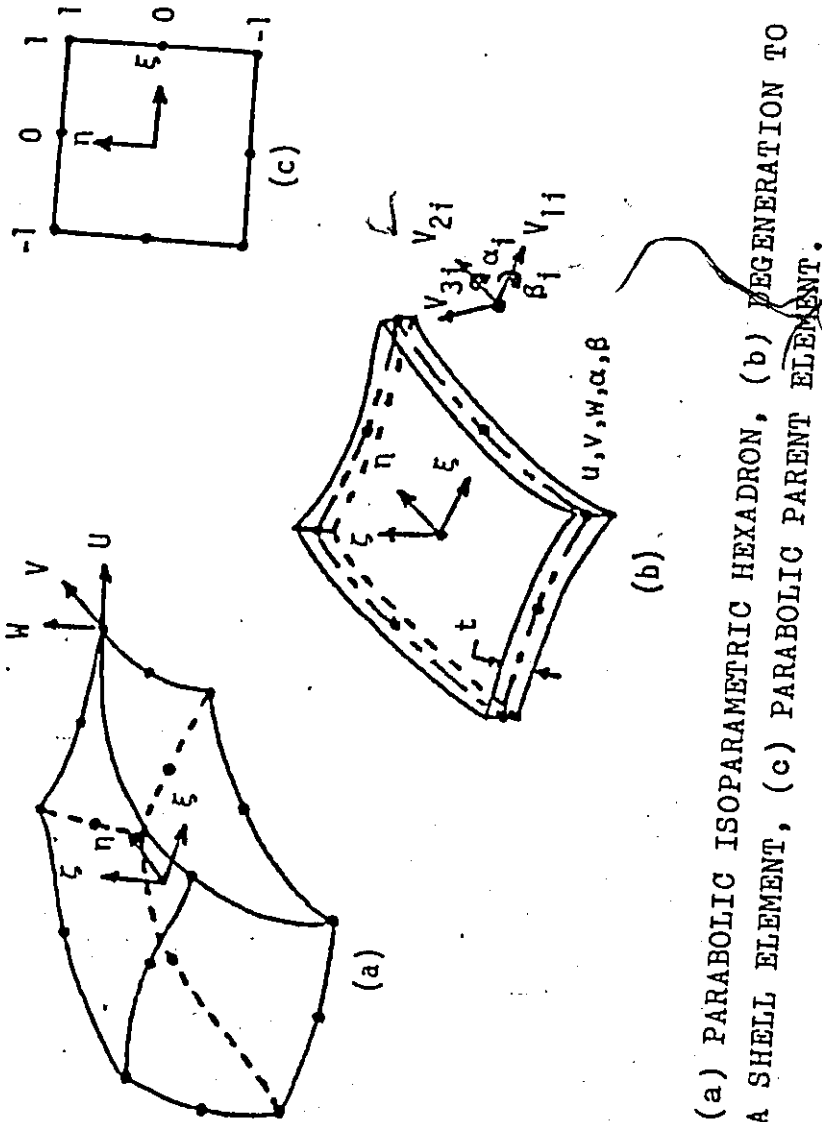


FIG. 4,1 (a) PARABOLIC ISOPARAMETRIC HEXADRON, (b) DEGENERATION TO A SHELL ELEMENT, (c) PARABOLIC PARENT ELEMENT.

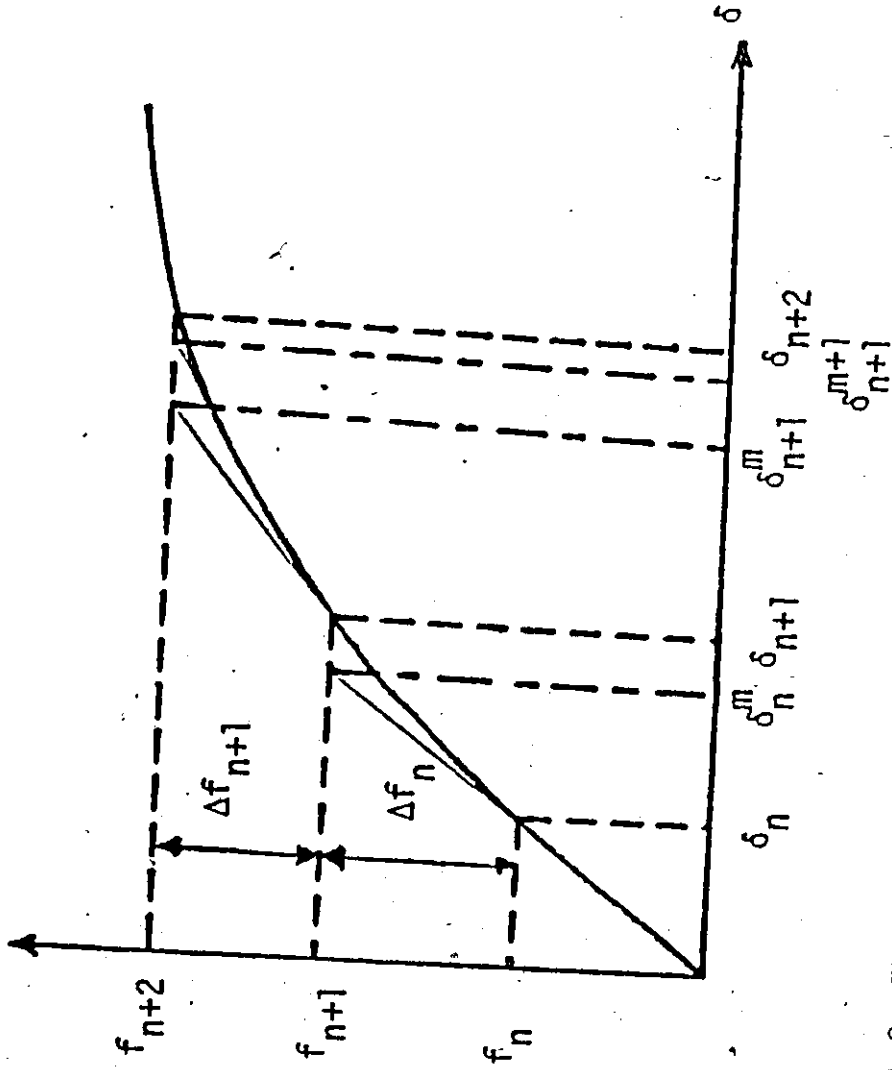


FIG. 4.2 INCREMENTAL LOAD ANALYSIS WITH NEWTON RAPHSON ITERATIONS.

☆

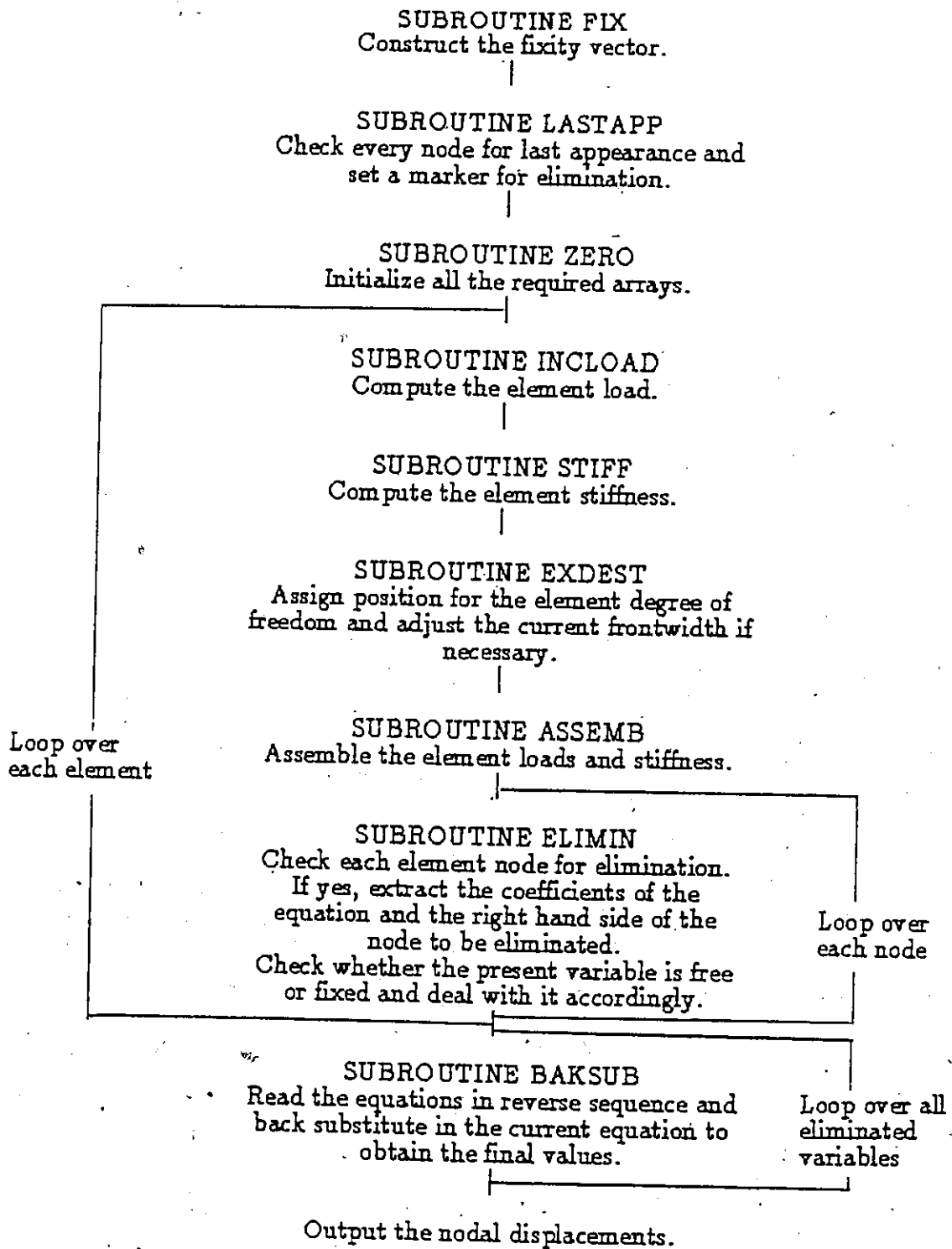


FIG. 4.3 OPERATION SEQUENCE FOR THE FRONTAL SOLVER.

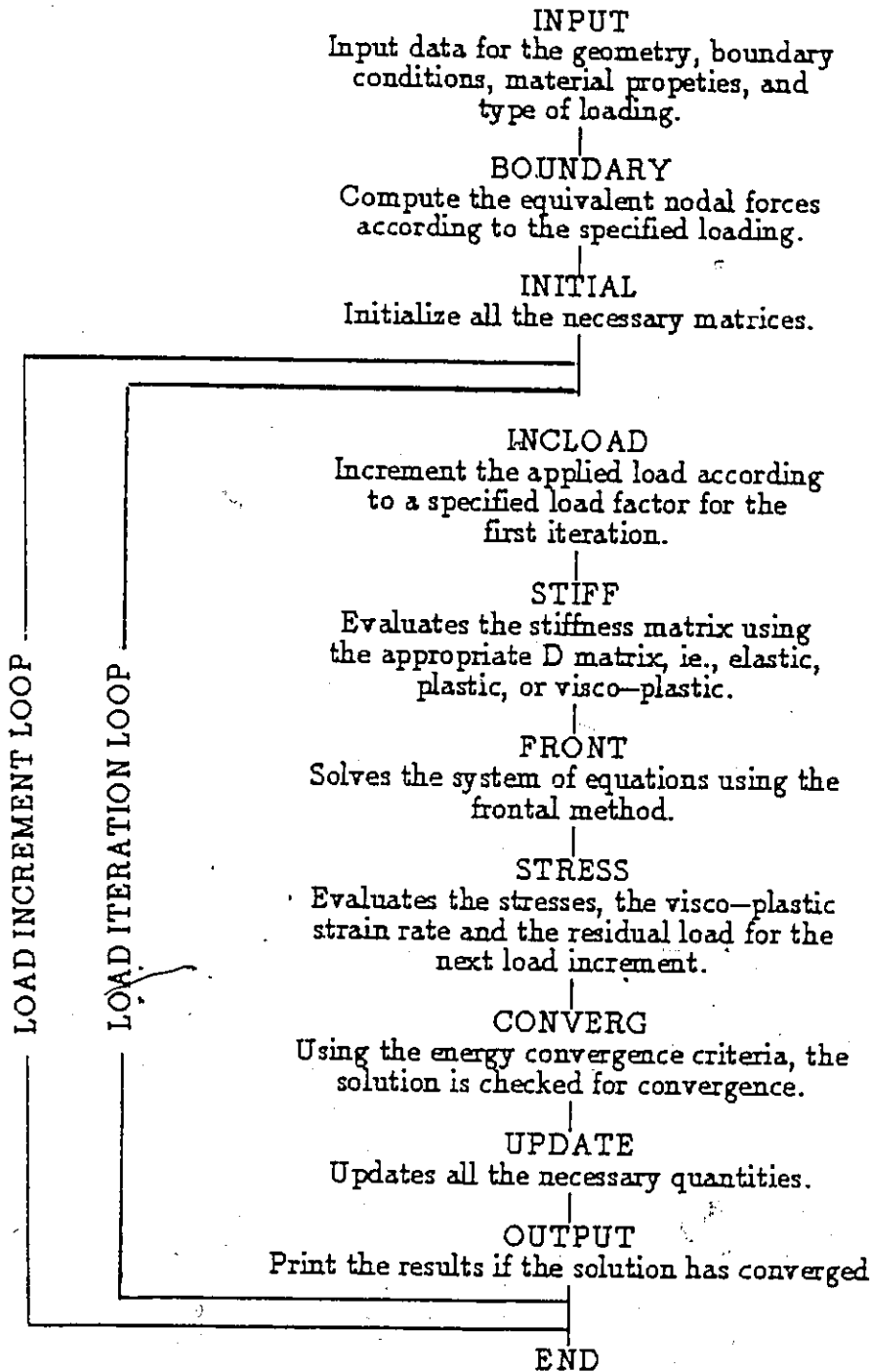


FIG. 4.4 FLOW CHART FOR THE ELASTIC VISCO-PLASTIC ANALYSIS PROGRAM.

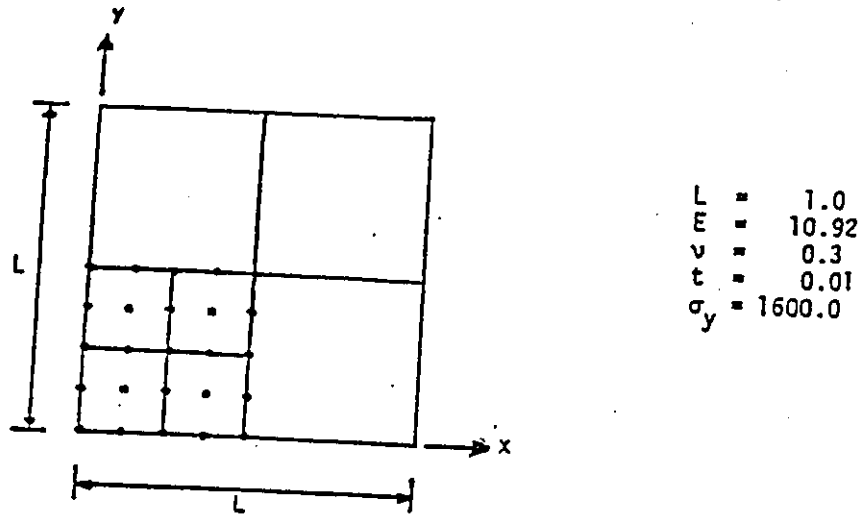


FIG. 4.5 GEOMETRY & MATERIAL PROPERTIES OF SIMPLY SUPPORTED PLATE (THICK PLATE ANALYSIS).

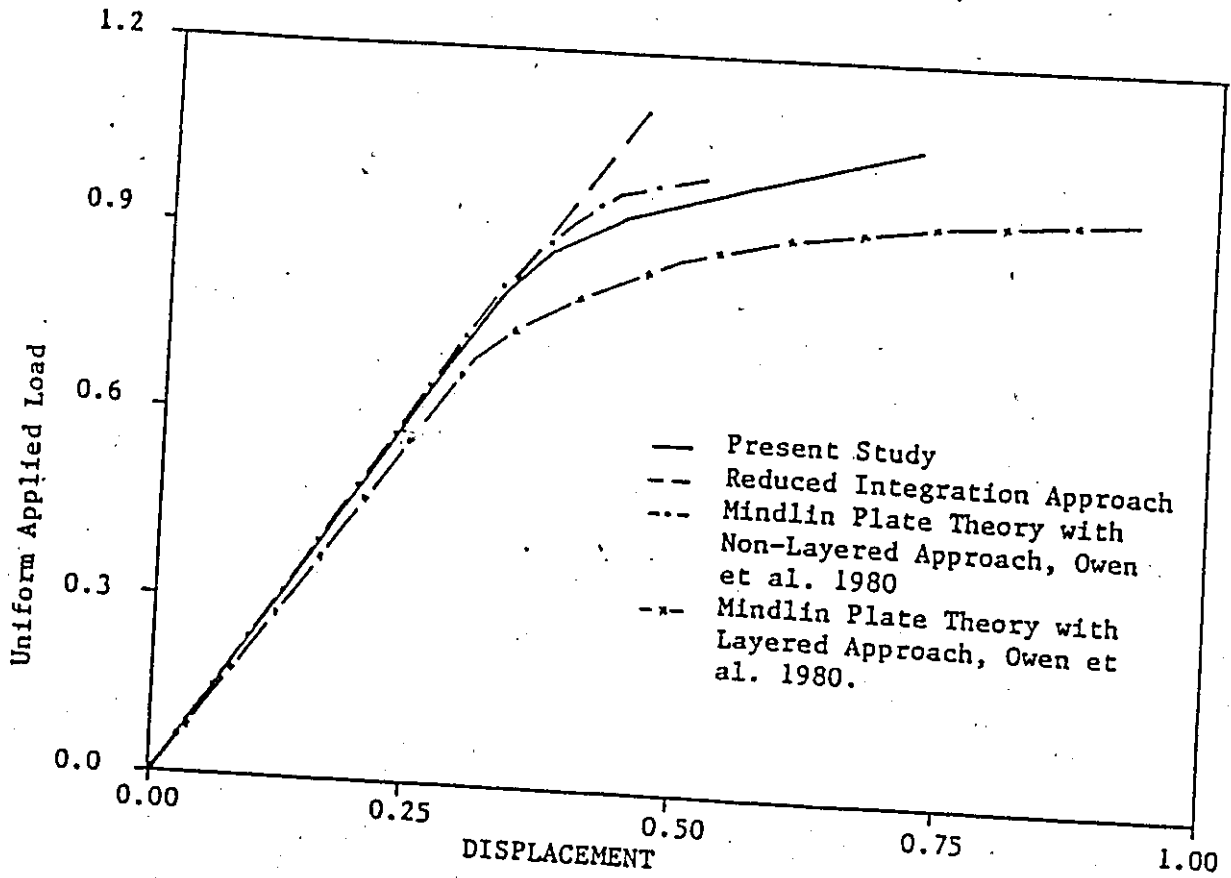


FIG. 4.6 LOAD DISPLACEMENT CURVE.

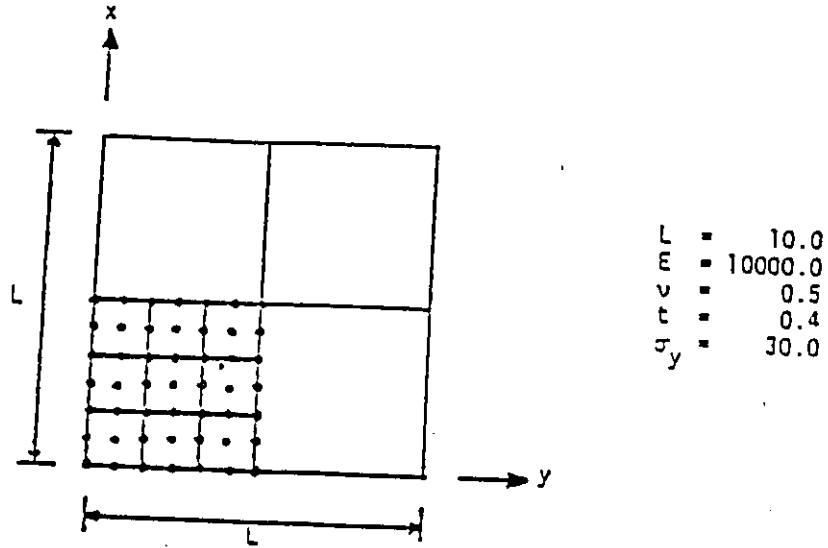


FIG. 4.7 GEOMETRY & MATERIAL PROPERTIES OF SIMPLY SUPPORTED PLATE (THIN PLATE ANALYSIS).

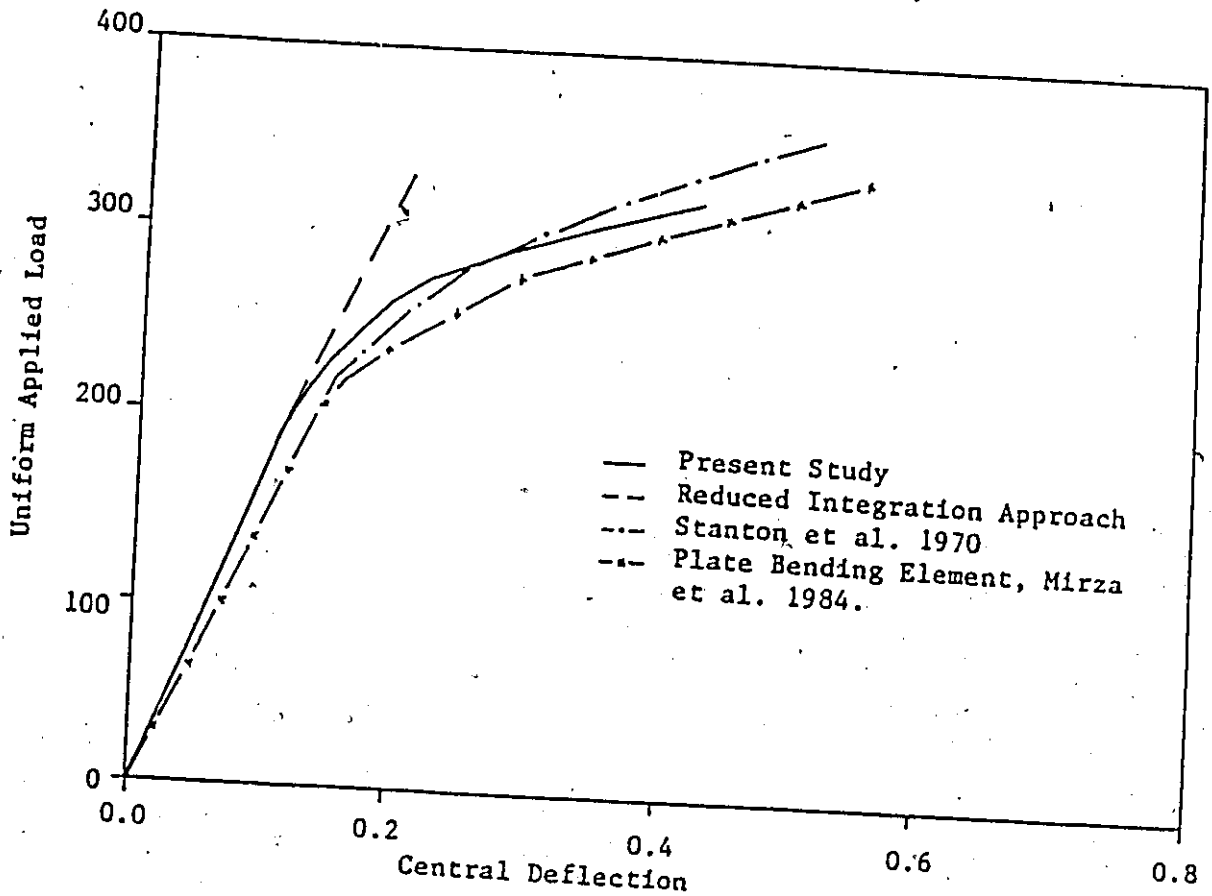
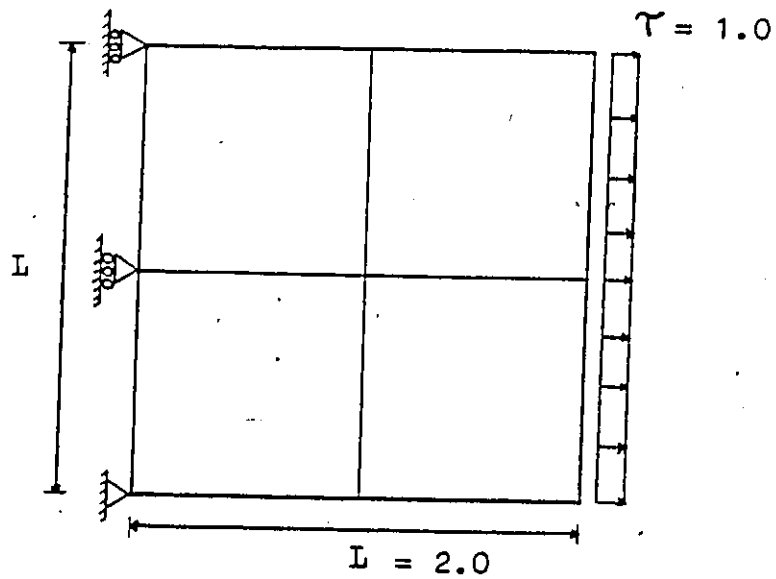


FIG. 4.8 LOAD DISPLACEMENT CURVE.



PROPERTIES:  $E = 10^6$   
 $\nu = 0.3$   
 $A = 10^{-7}$   
 $n = 6$   
 $Y = 0.0$

FIG. 4.9 GEOMETRY AND MESH PATTERN FOR THE DETERMINATE STRUCTURE.

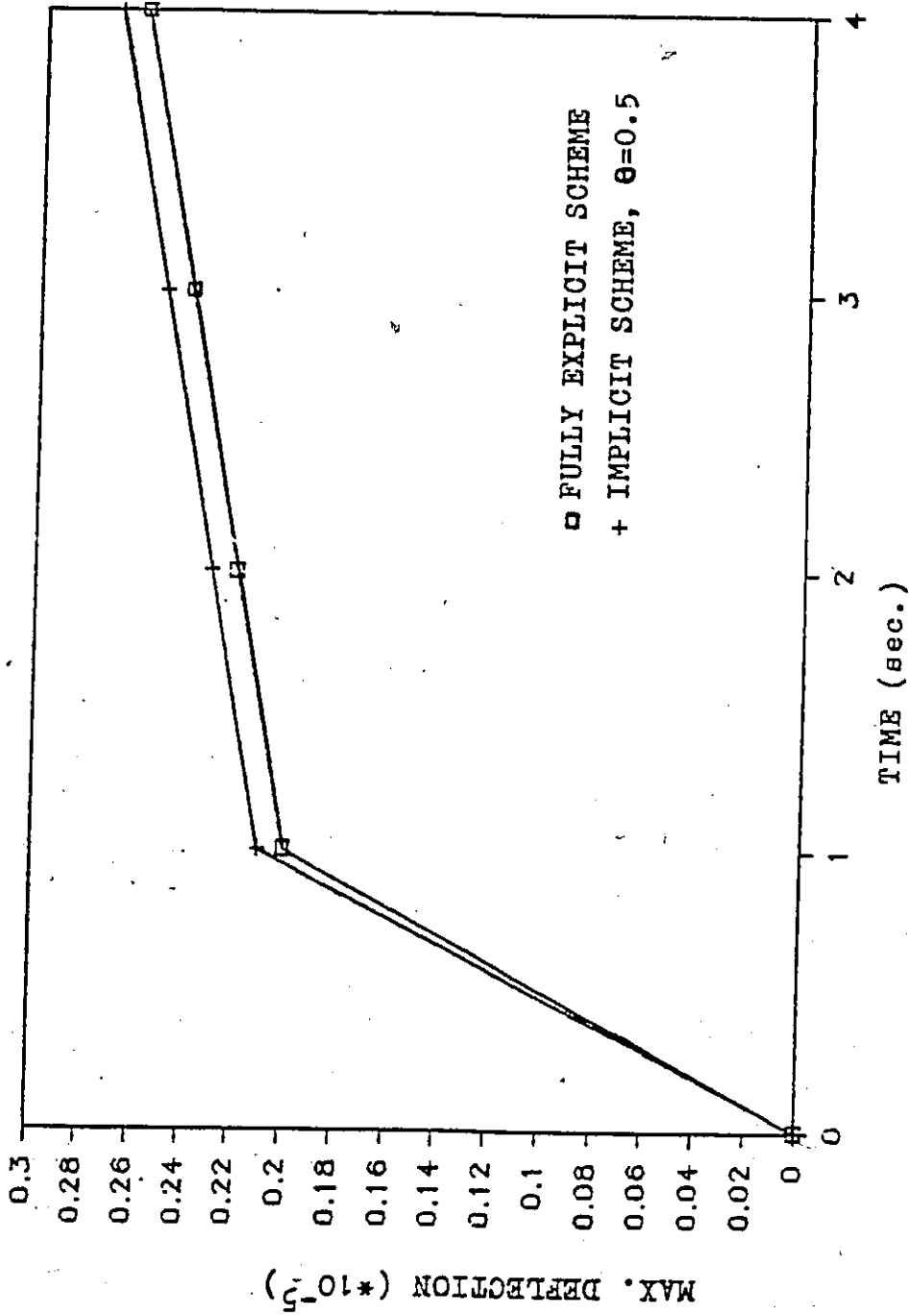
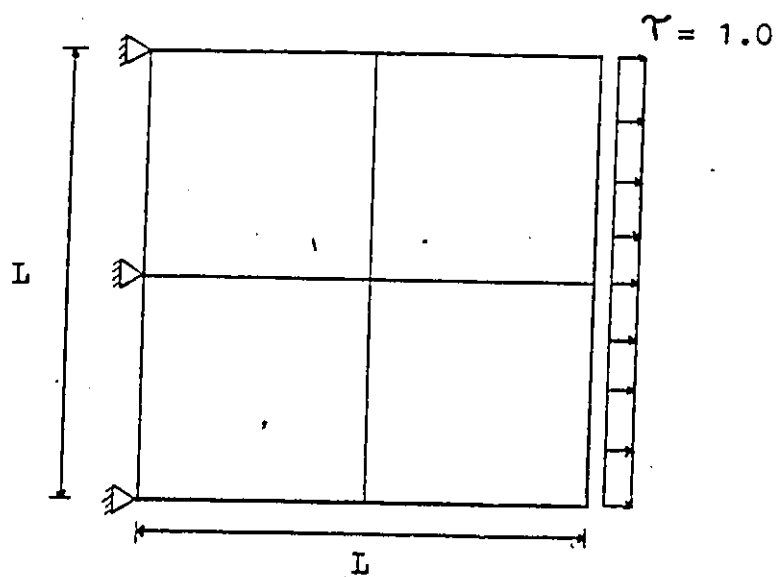


FIG. 4.10 TIME VS. MAXIMUM DEFLECTION.





PROPERTIES:  $L = 2.0$   
 $E = 10^6$   
 $\nu = 0.3$   
 $A = 10^{-7}$   
 $n = 6$   
 $\gamma = 0.0$

FIG. 4.11 GEOMETRY AND MESH PATTERN FOR THE INDETERMINATE STRUCTURE.

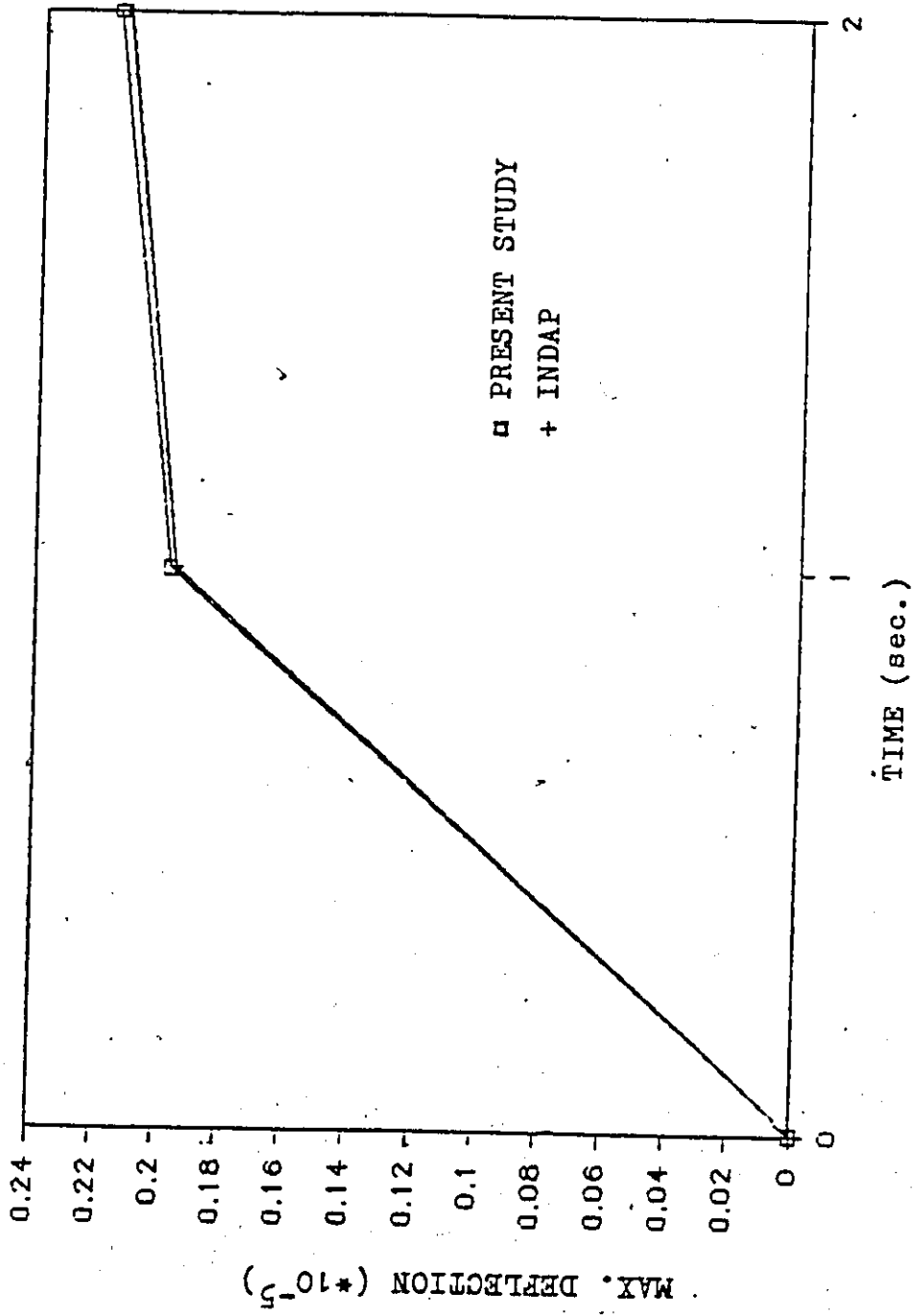


FIG. 4.12 TIME VS. MAXIMUM DEFLECTION (FULLY EXPLICIT,  $\theta = 0.0$ ).

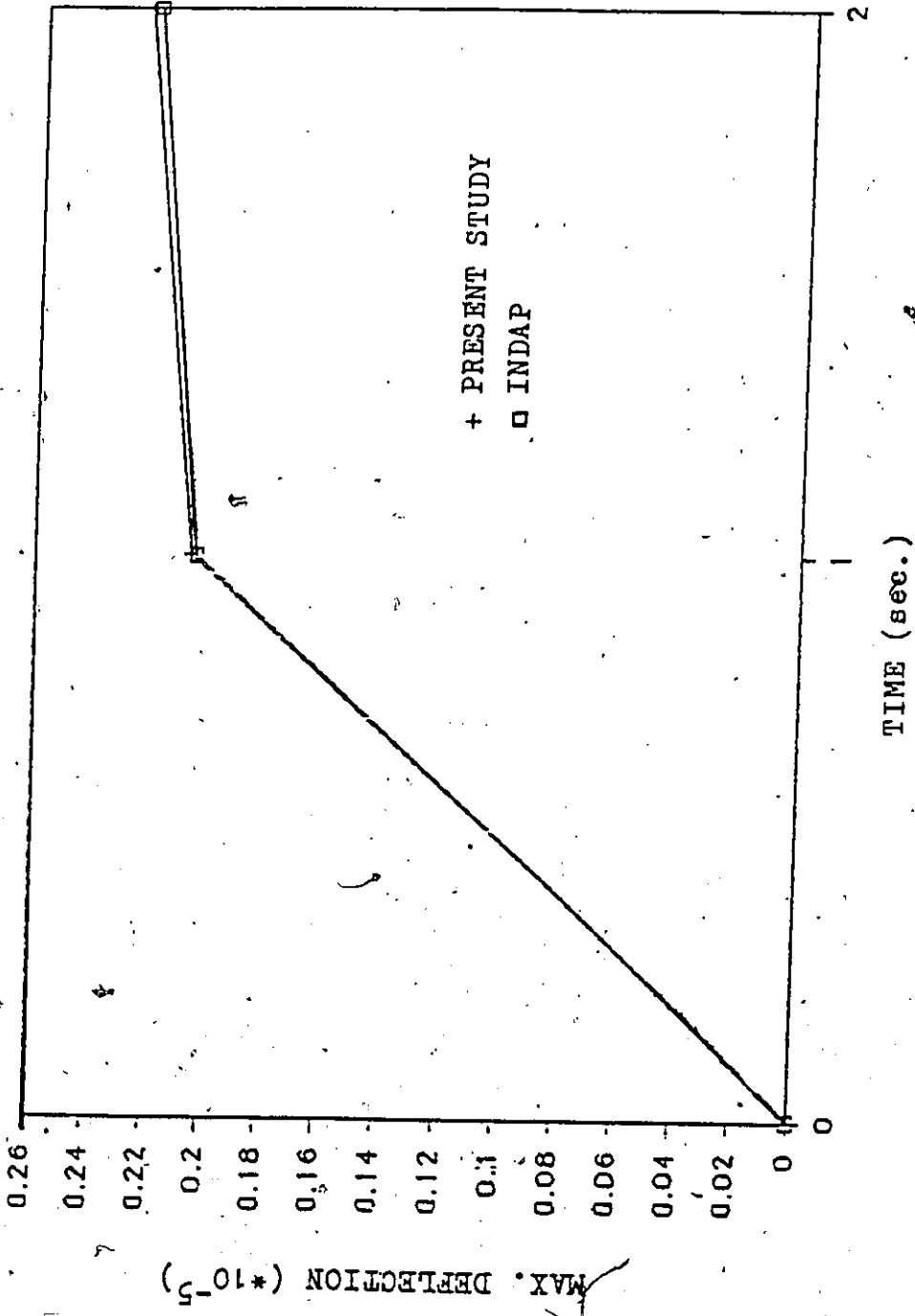


FIG. 4.13 TIME VS. MAXIMUM DEFLECTION (IMPLICIT SCHEME,  $\theta = 0.5$ ).

## CHAPTER FIVE

### EFFECTS OF MICRO-STRUCTURE ON THE MACRO-STRUCTURAL ANALYSIS FOR AUSTENITIC STAINLESS STEEL

#### 5.1 Introduction

In the discussion of the constitutive equations for the elastic visco-plastic analysis, it was realized that it is very difficult to incorporate the effects of micro-structure on the visco-plastic strain rate. The problem arose due to lack of experimental data for determining the relation between the grain size and the viscoplastic strain rate. To overcome this limitation, it was assumed that its effect is negligible and a constant was added to the visco-plastic strain rate function.

In 1955, The Hall-Petch equation [23] was introduced. Based on the experimental data, they found that the grain size plays a significant role in determining the magnitude of the yield strength. Furthermore, Norstrom [27] and Tobler et al. [33] reported recently that the data from their experiments were in good agreement with the Hall-Petch equation. To incorporate the effects microstructural changes, in general, and the grain size in particular, the Hall-Petch equation has been adopted in this study.

5.2 Influence of Temperature on Yield Stress of AISI 316L Austenitic Stainless Steel

Norstrom [27] conducted various experiments to determine effects of temperature on the yield stress of AISI 316L austenitic stainless steel. His specimens consisted of 50 kg laboratory ingots whose chemical compositions are given in Table 5.1. The ingots were hot rolled to a thickness of 18mm and then heat-treated at 1100° C for 20 minutes and then water quenched. This process resulted in recrystallized microstructures. Following that, the specimens were cold-rolled to a thickness of 12mm. To obtain different grain size distributions, the specimens were differently heat-treated. The first one was heated at 1000° C for 10 minutes and then water quenched. The second specimen was heated at 1100° C for 30 minutes and then water quenched, and the third specimen was heated at a temperature of 1200° C for 60 minutes and then water quenched. The light microscopy was used to study the microstructure of the specimens and the average line-intercept value measured for austenitic grain boundaries was taken as the austenitic grain size.

The yield stress was taken as the 0.2% proof stress. Its value, for the temperature range 20 to 600° C after annealing at 1100° C for 30 minutes and then water quenched, is given in Figure 5.1. From Figure 5.1, it can be observed that despite variation in the chemical composition, the yield stress values for the three specimens exhibit parallel trends. It is also shown that by increasing the nitrogen content of AISI 316L, the yield stress increases. However the influence of nitrogen on the yield stress is ignored in this study. Furthermore, as the temperature increases the yield stress decreases as expected. This effect was also observed by Tobler et al.

5.3 Influence of Grain Size on the Yield Stress of AISI 316L Austenitic Stainless Steel

Using the same experimental procedure and the same specimens, Norstrom [27] had conducted more experiments to determine the effects of grain size on the yield stress. Figure 5.2 illustrates the effect of grain size on the yield stress at 20° C, 300° C, and 600° C. At all three temperatures the value of the yield stress increases with decreasing grain size. This is in accord with the Hall-Petch equation given by,

$$\sigma_y = \sigma_i + K/\phi^{1/2} \quad (5.1)$$

where  $\sigma_i$  refers to the flow strength in the absence of grain boundaries and K is the slope of  $\sigma_y$  versus  $\phi^{-1/2}$  plot and indicates the grain boundary dependence of the yield stress.

As noted by Tobler et al. [33], the experimental data relating the effect of grain size to the yield stress of austenitic stainless steel is very limited and therefore very judicious use is necessary. They used Norstrom's [27] experimental data and at the same time adjusted the effect of nitrogen to 0.04 percent weight. The results are shown in Figure 6.6 and indicate that both  $\sigma_i$ , the friction stress, and k, the Hall-Petch parameter, are temperature dependent. Furthermore, the slope k is strongly temperature dependent at low temperatures and is independent of temperature when

the temperature is greater or equal to room temperature. These experimental data clearly indicate that the grain size plays a significant role in determining the magnitude of the yield stress.

#### 5.4 Yield Stress Incorporating Microstructure

Based on the experimental data given by Norstrom [27] and Tobler et al. [33] as has been discussed, it is justifiable to use the Hall-Petch equation given in Equation 5.1 for determination of the yield stress. This implies that the yield stress is a function of both temperature and grain size, i.e.,

$$\sigma_y = \sigma_y(T, \phi) \quad (5.2)$$

In Section 4.5, it was stated that the viscoplastic analysis is performed if and only if the effective stress is greater than or equal to the yield stress. This implies that although, the effect of microstructure is not directly incorporated into the constitutive equations, it certainly controls the macro-structural analysis. Again, for lack of more experimental data, it is decided to use Equation 5.2 to incorporate the effect of micro-structure in the present study.

TABLE 5.1

COMPOSITION OF STEELS INVESTIGATED (wt.-%) [27]

Steel	C	Si	Mn	P	S	Cr	Mo	Ni	N
A	0.022	0.56	1.42	0.012	0.015	17.9	2.8	14.2	0.05
B	0.024	0.61	1.41	0.012	0.015	17.8	2.8	14.3	0.11
C	0.027	0.62	1.41	0.013	0.016	18.0	2.7	14.1	0.18



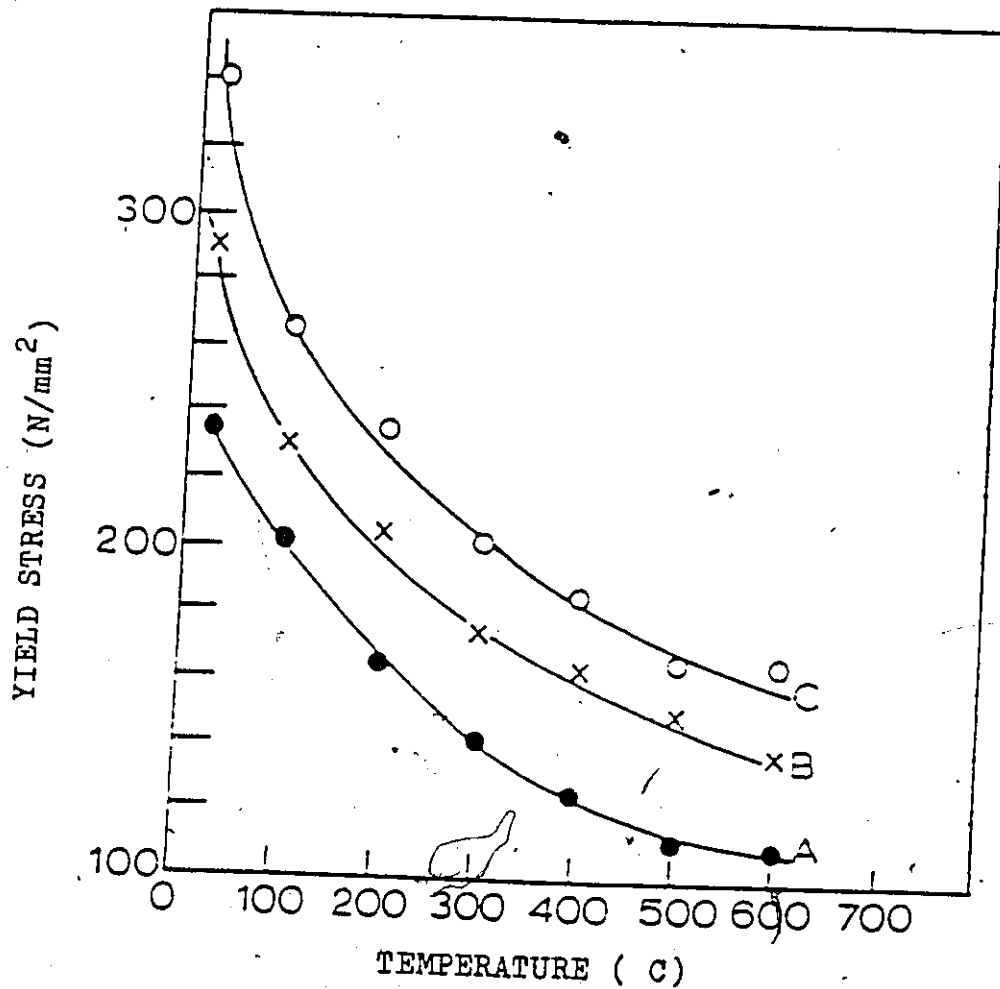


FIG. 5.1 INFLUENCE OF TEMPERATURE ON THE YIELD STRESS

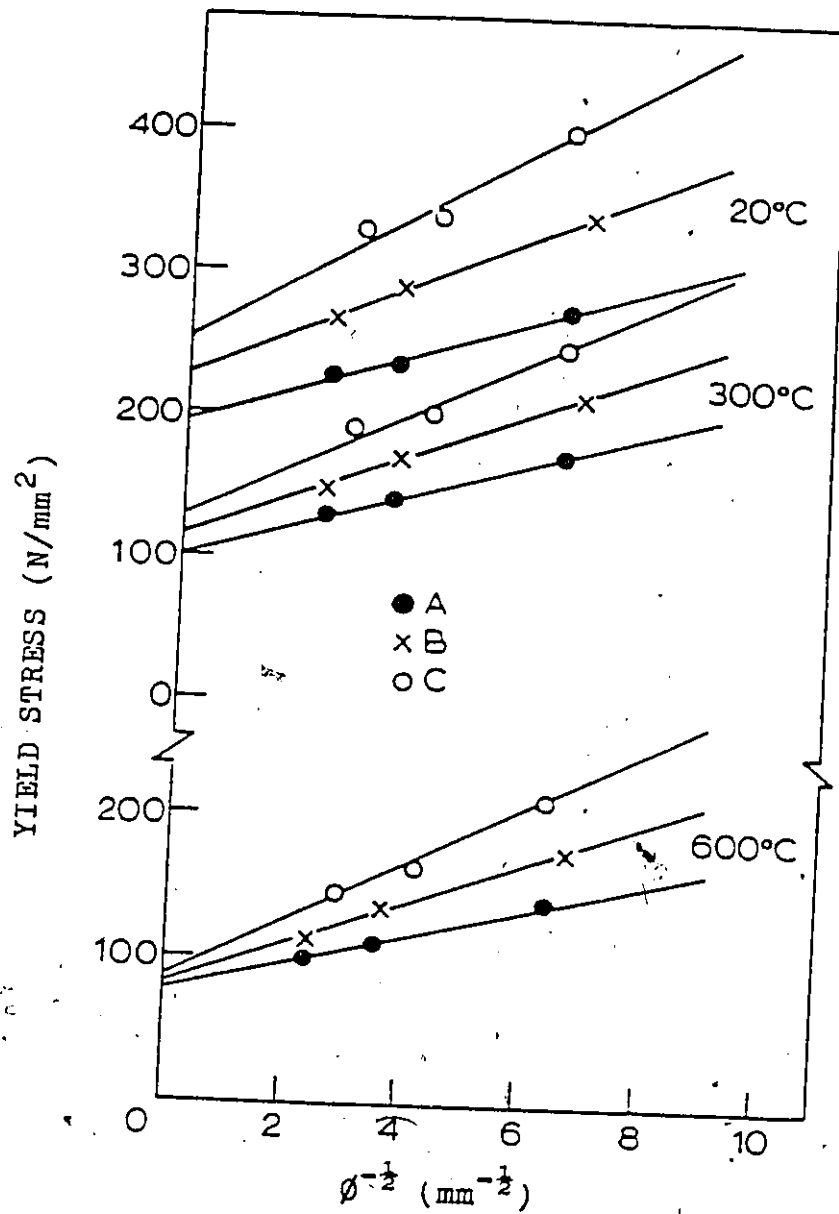


FIG. 5.2 INFLUENCE OF AUSTENITE GRAIN SIZE,  $\phi$ , ON THE YIELD STRESS AT 20°C, 300°C AND 600°C

## CHAPTER SIX

### MICRO/MACRO-STRUCTURAL ANALYSIS OF AUSTENITIC STAINLESS STEEL WELDMENTS

#### 6.1 Introduction

In the previous chapters, a stable and accurate thermo-elastic visco-plastic model has been presented and is capable of modelling a welding thermal cycle, the micro-structural changes, and the overall macro-structural response. The finite element model developed rendered good results, regarding various components, in comparison to experimental data and analytical results available in the literature. To check the overall accuracy and to demonstrate practical uses of the model, a bead-on-edge and a heat-on-edge welds are studied. Hwang [17] performed two experiments, bead-on-edge and heat-on-edge welds, on stainless steel 308 and reported results for the thermal cycle, the transient temperature field, the transient central deflection and the thermal strains. These experimental results are used for comparison purposes.

In this chapter, the transient heat flow analysis is carried out to model the thermal cycle and the transient temperature field due to a heat-on-edge weld and a bead-on-edge weld. The micro-structural changes due to the thermal cycle are determined and the distribution of the grain growth is computed. The elastic visco-

plastic analysis is carried out for bead-on-edge weld to demonstrate the accuracy and stability of the proposed macro-structural model. The transient central deflection, the thermal strains and stresses are, therefore, only presented for the bead-on-edge weld. The analytical results from the proposed finite element model are compared to Hwang's experimental and analytical results.

## 6.2 Experimental Studies

In order to demonstrate the accuracy, the stability, and the practical use of the proposed finite element model, data from an experimental study are required. Few researchers have studied, experimentally, the residual stresses due to a welding thermal cycle in high strength steel and low carbon steel [17,21]. However due to the constraint imposed, ignoring of recrystallization in the micro-structural model, a complete analysis can only be performed on austenitic stainless steel. Hwang [17] has conducted a complete experiment on austenitic stainless steel 308 and his experimental data are used in this study for comparison purposes.

The objective of Hwang's experiment was to measure temperature and strain changes that occur during welding. The temperature field was measured using thermocouples and the strain field was measured by strain gages placed on the surface of the specimen. Figure 6.1 shows the geometry of the specimens, 122 cm long by 10.2 cm wide by 1.3 cm thick, along with the experimental setup. There were three single-strain gages and three thermo-couples placed on the centreline of the speci-

men. Two more gages were placed 30.5 cm away from the centre of the specimen in order to measure the thermal strains at locations other than the centre. The specimens were welded by bead-on-edge with GMA process and by heat-on-edge with GTA process. The specimen is a 308 type stainless steel which is a high alloy steel and its chemical composition is shown in Table 6.1. The thermal and mechanical properties of austenitic stainless steel 316 are shown in Figures 6.2 to 6.7 and are used instead of austenitic stainless steel 308 due to the lack of material properties at elevated temperatures.

### 6.3 Numerical Example of Bead-on-Edge Weld

#### 6.3.1 Analysis of Bead-on-Edge Weld

The first specimen studied is that of weldment using a bead-on-edge with a GMA process which is the gas metal arc welding. It is assumed that the heat is distributed equally between the two welded pieces and hence allows the use of symmetry in the analysis to follow, i.e. only one half of the plate needs to be analyzed.

#### 6.3.2 Thermal Cycle

The finite element mesh for the three-dimensional heat flow analysis is shown in Figure 6.8 along with the properties of the welding arc (GMA process). As can be observed, the size of the elements are small near the weld and increases drastically away from it. This discretization is necessary to reproduce the high temperature gradients in the region near the weld, and otherwise can lead to numerical

instability, particularly oscillations. The plate is subdivided into 48 elements along the length, 6 elements across the width, and one element across the depth. This subdivision is based mainly on experience keeping in mind the problem of numerical instability. Since only one welding pass is considered, one element across the depth is believed sufficient for the analysis of this welded plate.

The maximum temperatures reached across the width (i.e. away from the weld) at the centreline from both the finite element model and the experimental study are shown in Figure 6.9. The evolution of temperature through contours at different times is shown in Figures 6.10 to 6.15. The transient temperature at 2.54 cm away from the welding edge, observed experimentally and computed analytically, is shown in Figure 6.16.

It can be concluded from comparison of results in Figure 6.9 that the finite element model is predicting well the maximum temperature reached in the specimen. This implies that the material properties employed are good representative of the specimen and that the modelling of the boundary conditions, particularly heat input and dissipation, is quite correct. From Figures 6.10 to 6.15, it is concluded that the model is very stable which is also justified by the fact that there are no oscillations observed. Furthermore, by examining Figure 6.16, which is the transient thermal response, it can be concluded that the welding arc model proposed for both, the heating and cooling rates, is adequate.

### 6.3.3 Grain Growth

Based on the mathematical model presented in Chapter Three, the austenite grain growth is computed due to the bead-on-edge weld and the final grain distribution along the distance away from the welding edge is shown in Figure 6.17. There are no experimental results available to compare with the finite element results. However, it can still be concluded that the distribution is smooth and that the method is stable. This fact is demonstrated through smooth transition that can be observed from region near the welded edge to about half a centimeter away where after there is no grain growth. This also approximates the extent of the heat affected zone (grain growth zone).

### 6.3.4 Finite Element Modelling of Macro-Structural Analysis

The effect of both the welding thermal cycle and the micro-structural changes is investigated using the proposed macro-structural model. The mesh pattern and the visco-plastic material properties adopted for this study are shown in Figure 6.18. The thermal load, which is mainly the thermal expansion and contraction, is applied as discussed in Chapter Four and is incorporated through use of twenty seven integration points per element. The temperature field is incorporated in a similar manner, i.e. temperatures at the integration points.

The plate is supported at the corners as shown in Figure 6.18. It is believed to be a good boundary representation of the experimental setup. To reduce the size of the numerical problem, it is decided to perform the elastic visco-plastic

analysis on only half of the plate due to symmetry. Two cases can be considered in the modelling of the welded edge boundary; a free surface type boundary and a contact type boundary. Neither one represents the boundary condition precisely since the plates are not restrained ahead of the welding arc and are indeed joined together behind it. A free surface type boundary is appropriate to model the boundary ahead of the welding arc because of the gap and is employed in this study. The difficulty arises in the modelling of the boundary behind the welding arc, especially after the weld has solidified. In general this is a very complex boundary condition and also involves out-of-plane displacements. However, it is assumed that the out-of-plane displacements are small enough to be ignored. This assumption allows to model the welded boundary as a contact surface. This is thought to be reasonable due to the fact that inclusion of transverse out-of plane displacements will result in extraordinary computational effort and cost. With the simplification introduced above and the complexities that would otherwise prevail, the mixed boundary conditions introduced are thought to best represent the welded plate and hence are employed in this study.

The material properties given in Figure 6.18 and employed for the visco-plastic model are according to Frost and Ashby [15]. These are based on the experimental results. Again it should be noted that all of the material properties used are for austenitic stainless steel 316 and not 308 which was used in the experimental setup by Hwang [17]. The difference in the material properties is supposed to be not significant and the errors introduced are believed to be within the bounds of the finite element model employed.



### 6.3.5 Thermo-Elastic Visco-Plastic Analysis

The transient central deflections at point A in Figure 6.18, observed experimentally and computed analytically, are shown in Figure 6.19. The transient thermal strains, at 2.54 centimeter and 4.45 centimeter away from the welded edge and along the centreline, observed experimentally and computed analytically, are shown in Figures 6.20 and 6.21, respectively. The longitudinal residual stresses computed after 76.2 seconds and 139.7 seconds along the line perpendicular to the weld are shown in Figure 6.22. Also the transverse residual stresses computed after 76.2 and 139.7 seconds along the line perpendicular to the weld are shown in Figure 6.23.

It appears from Figure 6.19 that the finite element results from the present model correlate much better with the experimental results than Hwang's [17] analytical results. The maximum deflection computed from the proposed model is slightly less than the experimentally observed values whereas Hwang's prediction is much smaller, almost half its magnitude. A comparison of the time history for the central deflection obtained from the proposed finite element model with those obtained experimentally and analytically by Hwang indicates that the response is in very good agreement from 0 to 40 seconds and after about 110 seconds with the experimental results. The discrepancy observed between 40 and 110 seconds is considered to be due to larger time interval employed in the analysis, especially larger tolerances for the convergence criterion, and due to the slight differences in the material properties adopted. It appears that while the larger residual loads were carried to the following loading intervals, some self correction eventually led to more

accurate results for response beyond 110 seconds. It must be due to the fact that beyond this time (110 seconds), the time interval sizes used are adequate. The more relaxed tolerance for convergence was used to prevent the high computing cost. However, it can be concluded that the proposed finite element model is capable of predicting a reasonable accurate time-dependent response.

Figure 6.20 shows the predicted transient longitudinal thermal strains at 2.54 centimeter away from the welded edge along the centreline. By examining the figure, it can be observed that Hwang's analytical model yields much smaller thermal strains whereas the present finite element model predicts values for thermal strains that are of the same magnitude as those observed experimentally. Although, the finite element model overestimates the magnitude of the thermal strains initially, perhaps due to larger time intervals, the overall transient response correlates quite well with the experimental results. As the specimen cools off, the strains from the proposed finite element model are slightly smaller than the experimental values. While the possible sources of errors in the finite element model have been identified before, the possible errors in strain measurements at elevated temperatures ( in the neighbourhood of  $250^{\circ}\text{C}$  ) can also explain the discrepancy mentioned above.

By examining Figure 6.22, at 4.45 centimeter away from the welded edge, the finite element model predicts larger thermal strains initially and slightly smaller as the specimen cools off. There is also a slight oscillation between 55 and 75 seconds and is believed to be due to the relaxed convergence criteria. Again the analytical results computed by Hwang are much smaller than the one observed experimentally. For clarification purposes, the finite element model employed by Hwang does not

compensate for material non-linearities, particularly plasticity or visco-plasticity. Once again, it can be stated that the present finite element results correlate well with the experimental data keeping in mind that there are experimental errors and their magnitudes are not known.

Although, there are no experimental results available to check the magnitude of the longitudinal residual stresses ( $\tau_{xx}$ ) shown in Figure 6.22, the profile obtained is very reasonable and appears to be similar to those reported in the literature [5,21,25] for several material types. The value of the yield stress at room temperature is about 500 MPa and the maximum computed residual stress using the present elastic visco-plastic is 420 MPa. This confirms that the residual stresses in the austenitic stainless steel of type 308 weldments can be of comparable magnitude to the yield stress.

The change in the transverse stress ( $\tau_{yy}$ ) distribution along the line perpendicular to the welded edge with time is shown in Figure 6.23. Once again, there are no experimental data available for comparison. Again, the profile is similar to those reported in the literature [5,21,24]. The maximum value computed for the transverse stress is about half that of the yield stress. This value is slightly large compared to those reported in the literature, Ref. [24].

From the results presented above, it can be concluded that the elastic visco-plastic model proposed is very adequate and the boundary conditions employed, especially along the welded edge, are reasonably good representation of the real boundary.

## 6.4 Numerical Example of Heat-on-Edge Weld

### 6.4.1 Analysis of Heat-on-Edge Weld

The second specimen studied is that of weldment using a heat-on-edge with a GTA process which is the gas tungsten arc welding. Again, it is assumed that the heat is distributed equally and therefore, with the use of symmetry, only one half of the plate is analyzed.

### 6.4.2 Thermal Cycle

The finite element mesh for the three-dimensional heat flow analysis is similar to the bead-on-edge weld as shown in Figure 6.8 along with the properties of the welding arc (GTA process). The maximum temperatures reached across the width (i.e. away from the weld) at the centreline from both the finite element model and the experimental study are shown in Figure 6.24. The evolution of temperature field at different times is shown in Figures 6.25 to 6.30. The transient temperature at 2.54 cm away from the welding edge, observed experimentally and computed analytically, is shown in Figure 6.31.

By examining Figure 6.24, the results obtained from the finite element model are again in good agreement with those measured experimentally (Hwang [17]) by both the liquid indicator and the thermocouple. Also from Figures 6.25 to 6.30, it can be concluded that the model is stable. The evolution of temperature around the

arc is slightly different from that for the bead-on-edge weld. For the bead-on-edge weld, the arc speed is almost twice as fast as that for the heat-on-edge weld. As a consequence, most of the heat remained behind the arc whereas for the heat-on-edge, it can be observed that some of the heat managed to propagate ahead of the arc. Therefore, the speed of the arc affects the temperature distribution.

By observing Figure 6.31, it can be concluded that the modelling of the heating and cooling rate is proper. Furthermore, the molten zone is ignored in this study, and the results obtained for both the heat-on-edge and bead-on-edge weld indicate that although it is a very turbulent zone, it does not significantly alter the peak temperature in the area close to the weld. This conclusion is again based on the good correlation between the peak temperatures computed analytically and those measured experimentally. Finally, the modelling of the welding arc as a heat per unit area is reasonable and very accurate.

#### 6.4.3 Grain Growth

Again, based on the mathematical model presented in Chapter Three, the austenite grain growth are computed due to the heat-on-edge weld and the final grain distribution along the distance away from the welding edge is shown in Figure 6.32. It can be concluded from the figure that the model is stable. The results appear to be in the right direction since the austenite grain size from the heat-on-edge weld is larger with a larger peak temperature than the bead-on-edge weld. Once again, the distribution is smooth and the method is stable as was for the bead-

on-edge. Also the size of the heat affected zone (grain growth zone) is observed to be slightly larger for the heat-on-edge weld.

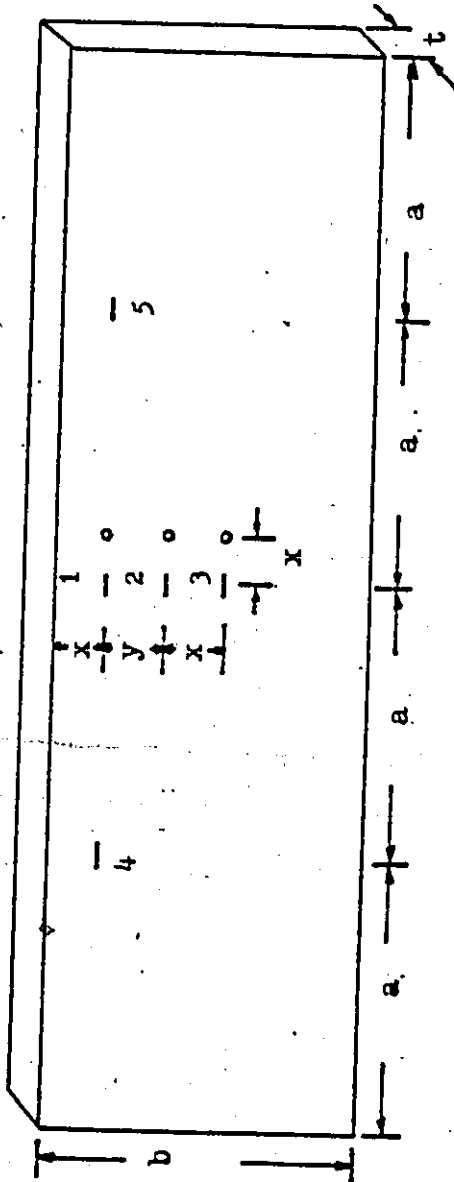
TABLE 6.1

CHEMICAL COMPOSITION OF 308 TYPE STAINLESS STEEL  
AS GIVEN BY HWANG [17].

---

Cr	Ni	C	Mn	Si	P	S
17/21	10/12	0.08	2.0	1.0	0.045	0.030

---



DIMENSIONS:  $a = 30.48$  cm  
 $b = 10.16$  cm  
 $t = 1.27$  cm  
 $x = 2.54$  cm  
 $y = 1.91$  cm

— SINGLE GAGES  
o THERMOCOUPLES

FIG. 6.1 SPECIMEN PREPARATIONS FOR 308 STAINLESS STEEL [17].



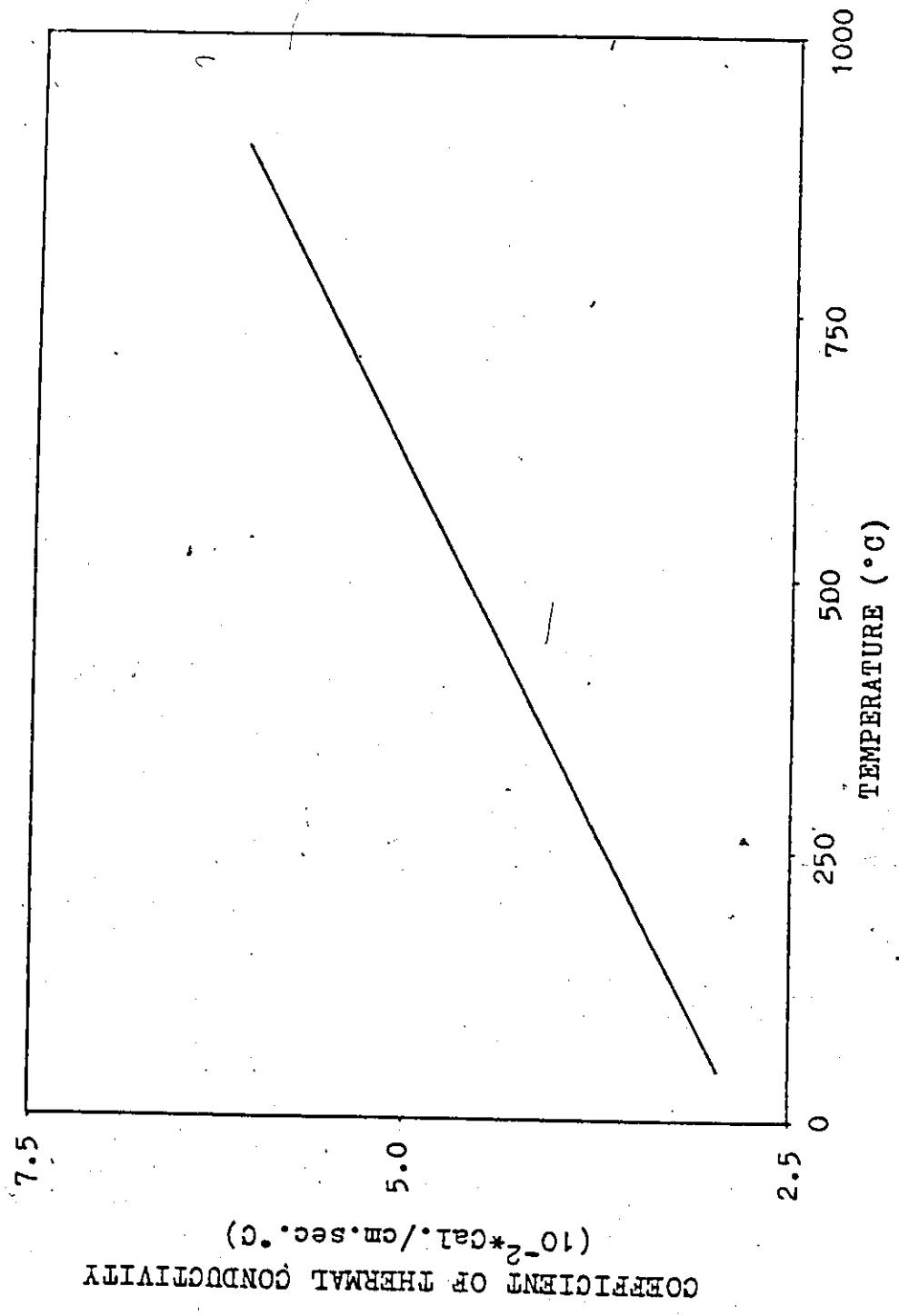


FIG. 6.2 THERMAL CONDUCTIVITY OF STAINLESS STEEL (Type 316) [24].

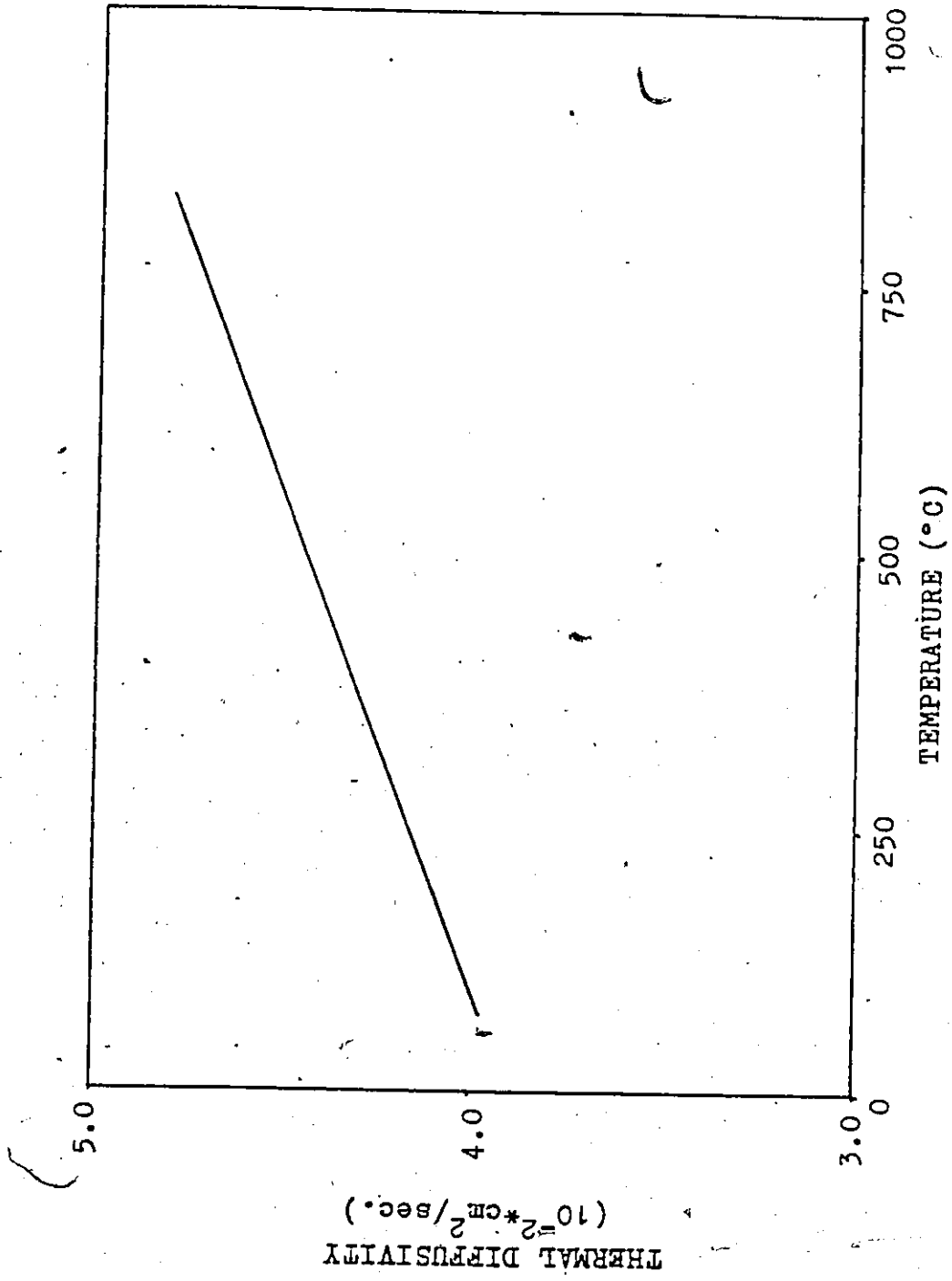


FIG. 6.3 THERMAL DIFFUSIVITY OF STAINLESS STEEL (Type 316) [24].

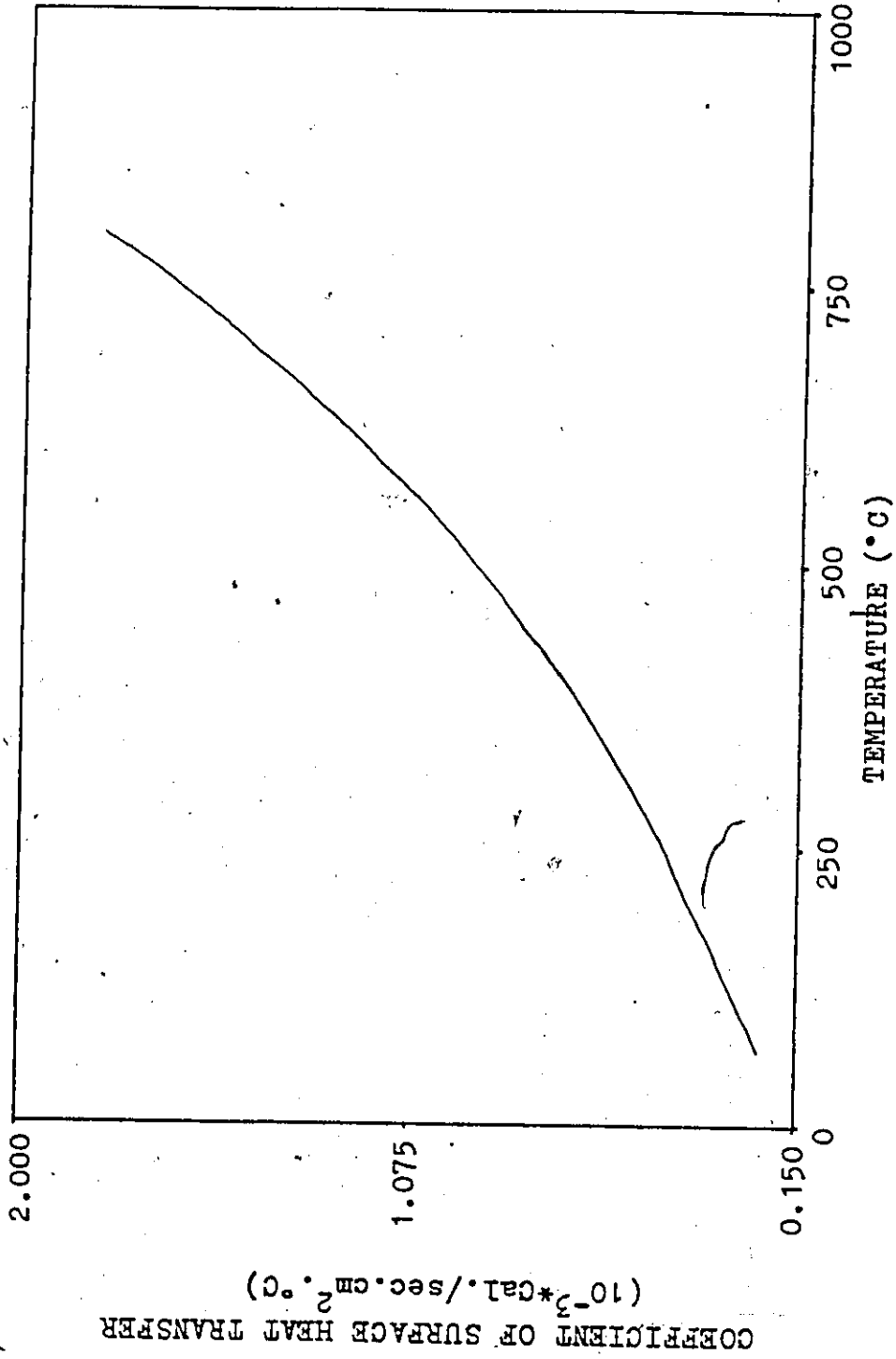


FIG. 6.4 SURFACE COEFFICIENT OF HEAT TRANSFER.

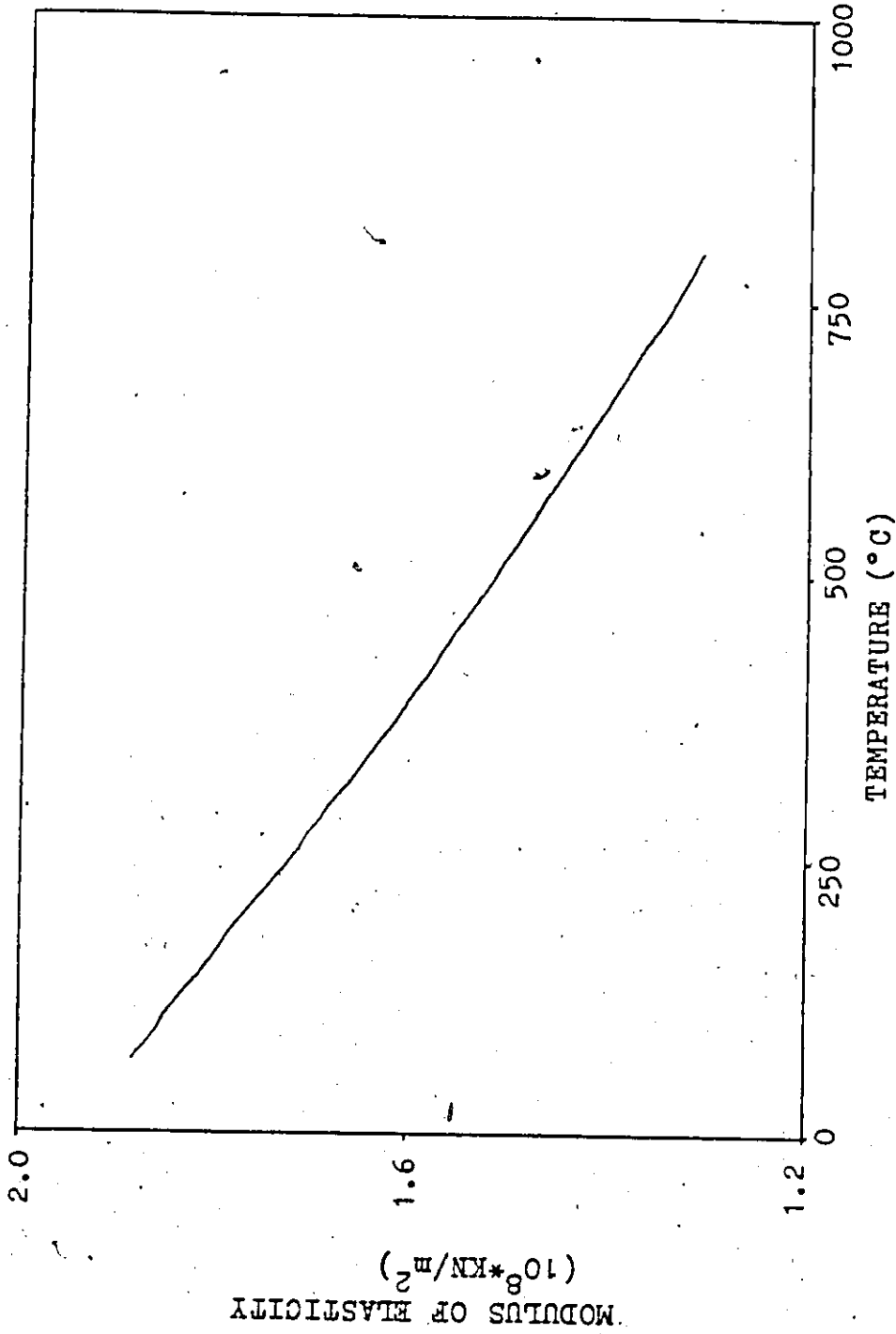


FIG. 6.5 YOUNG'S MODULUS AT ELEVATED TEMPERATURES [32].

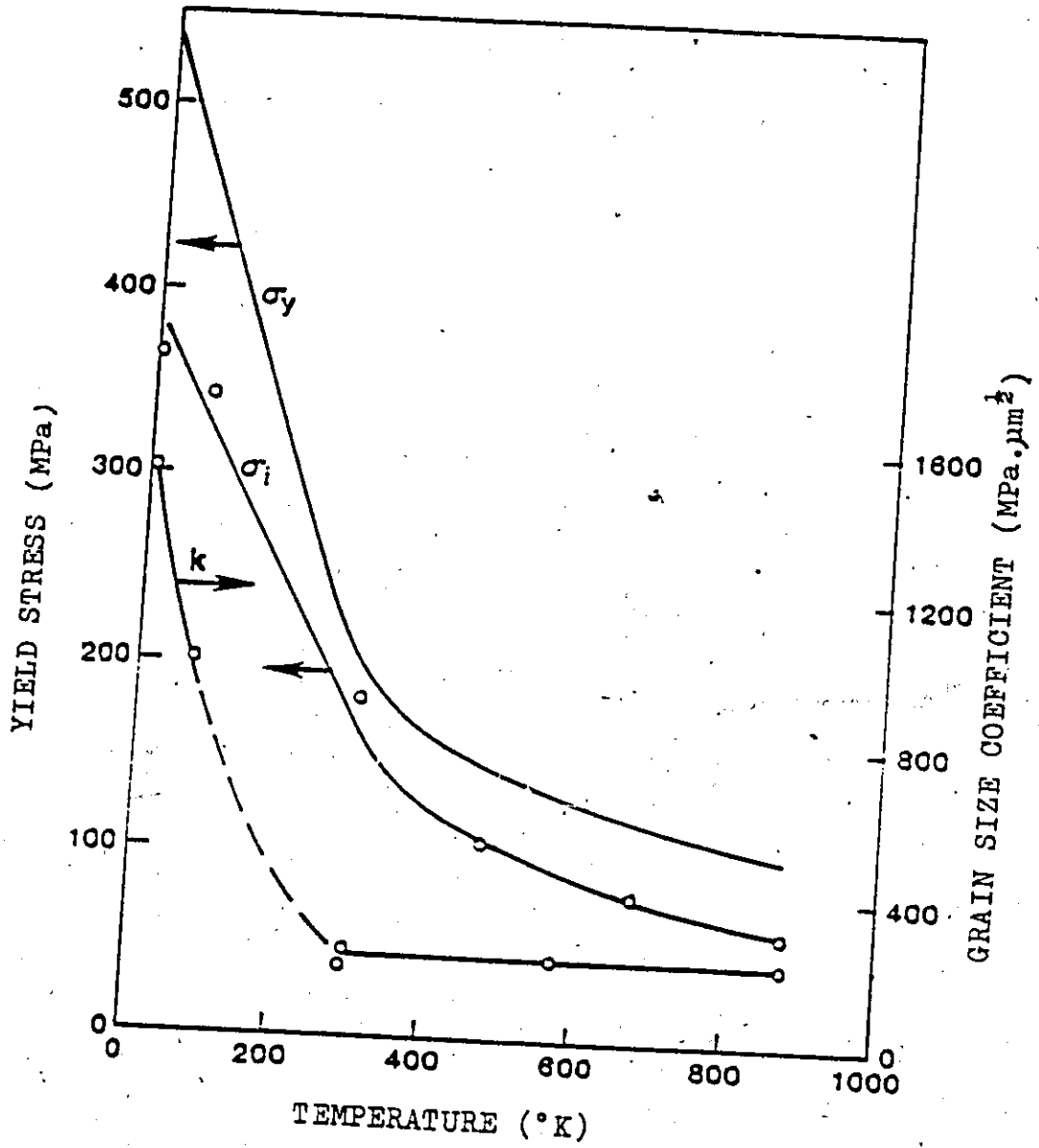


FIG. 6.6 YIELD POINT AT VARIOUS TEMPERATURES [33].

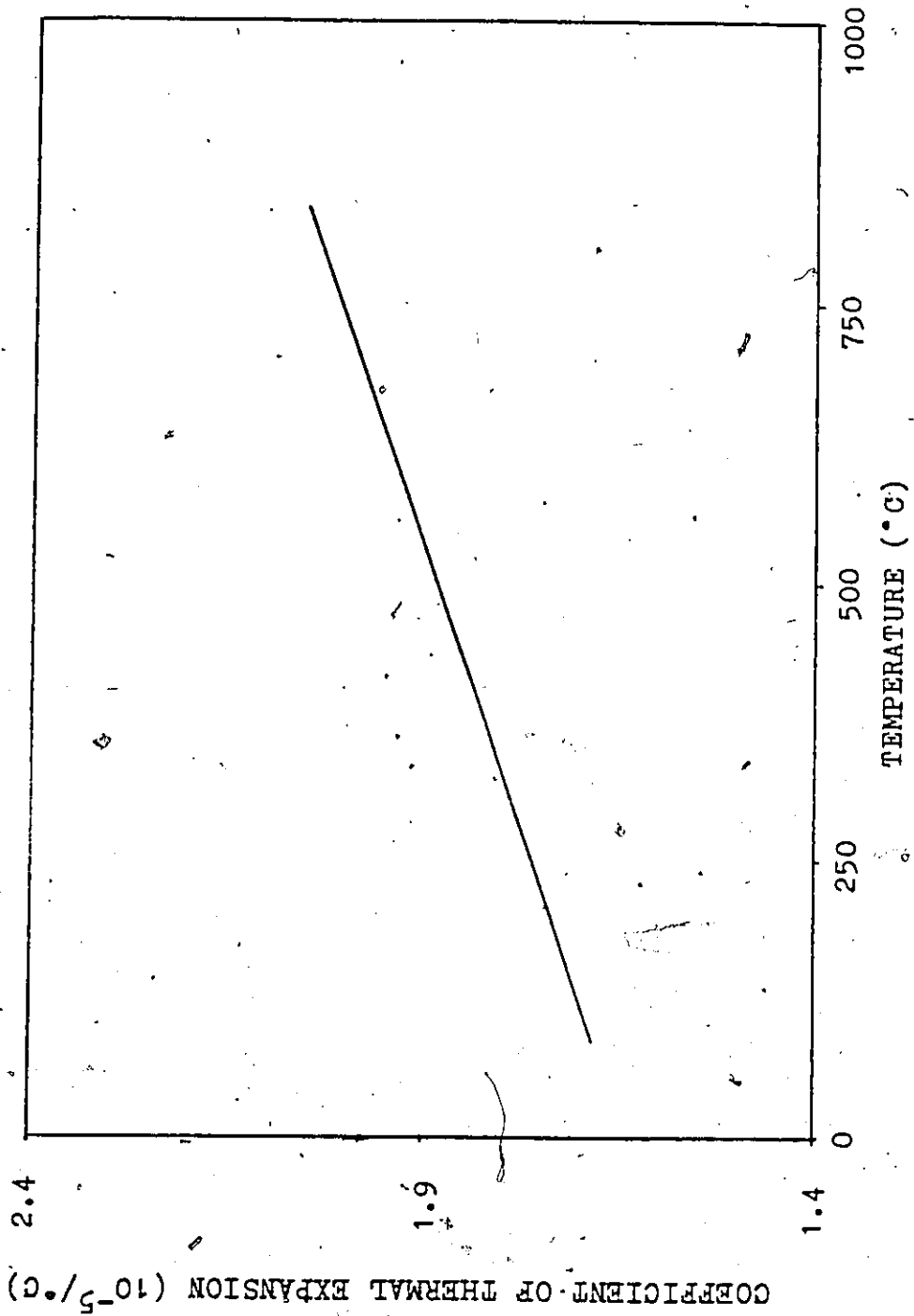
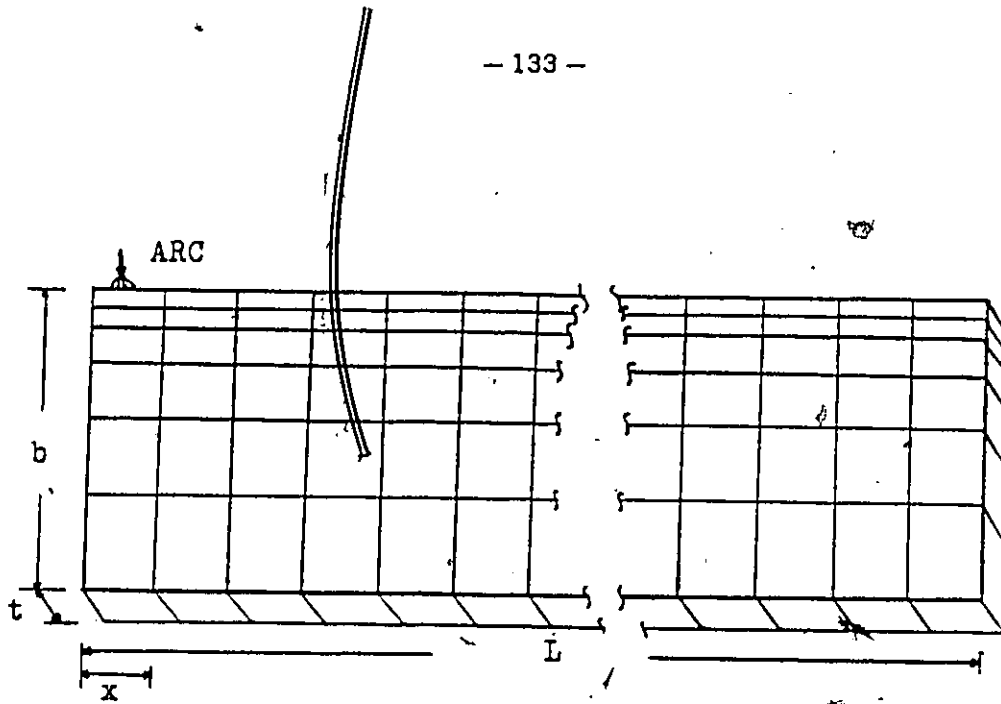


FIG. 6.7 COEFFICIENT OF LINEAR EXPANSION AT ELEVATED TEMPERATURES [17].



DIMENSIONS:  $L = 121.92$  cm  
 $b = 10.16$  cm  
 $t = 1.27$  cm  
 $x = 2.54$  cm

WELD PROPERTIES:

GMA WELD

$I = 250$  A

$V = 27$  V

$v = 1.19$  cm/sec.

Eff. = 0.43

GTA WELD

$I = 324$  A

$V = 12$  V

$v = 0.655$  cm/sec.

Eff. = 0.51

FIG. 6.8 GEOMETRY AND MESH PATTERN OF THE SPECIMEN, AND PROPERTIES OF THE WELDING ARC.

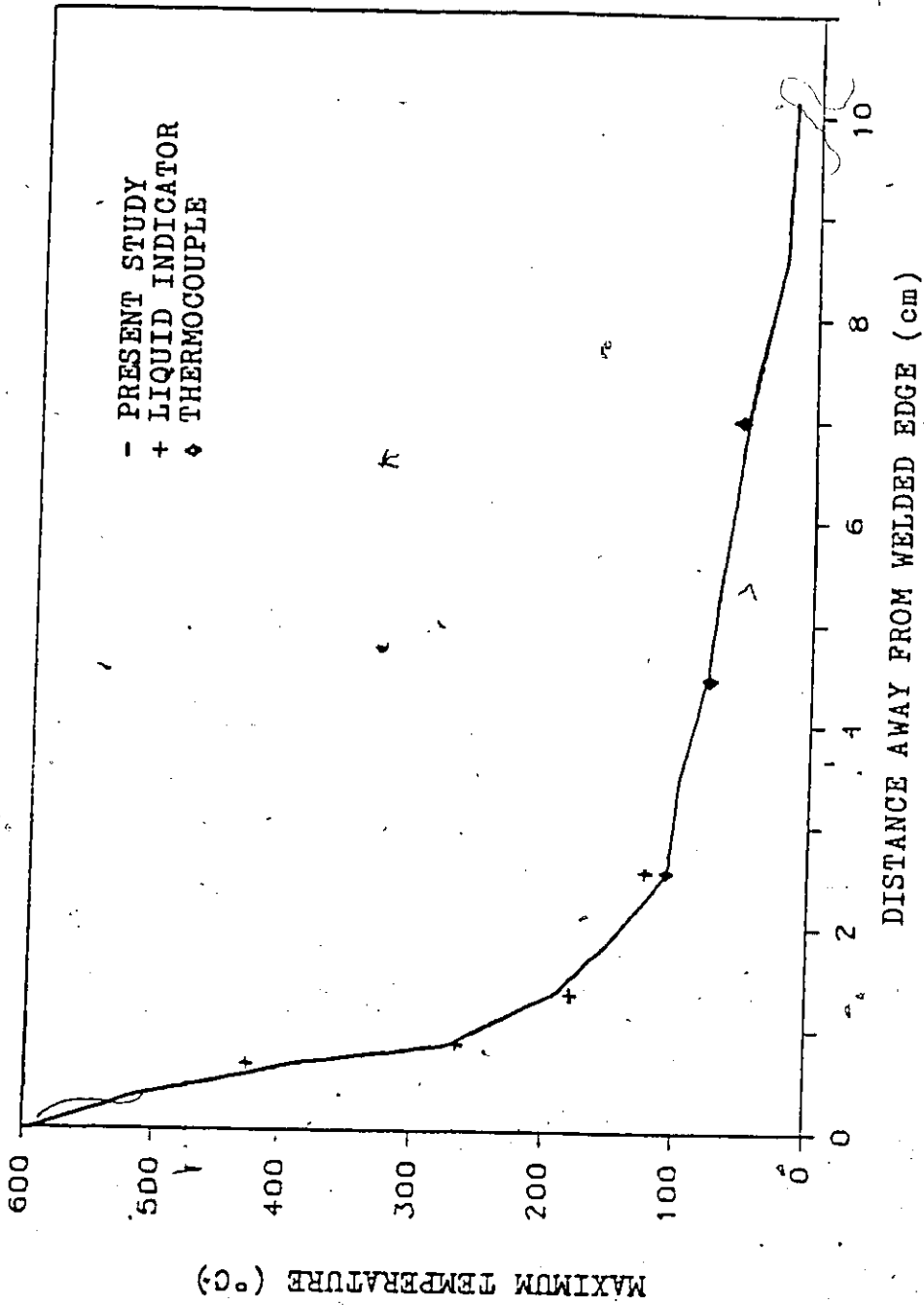


FIG. 6.9 MAXIMUM REACHED TEMPERATURE DISTRIBUTION ( GMA WELD ).



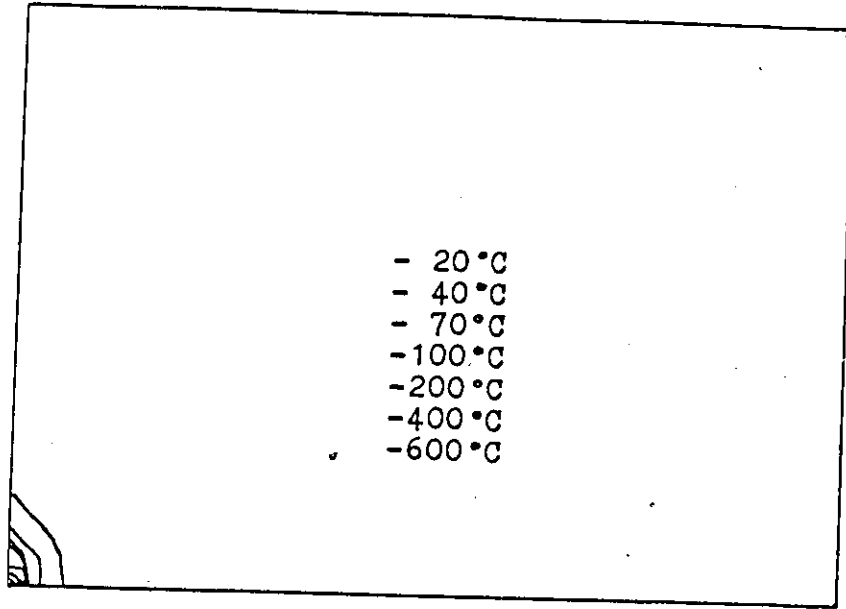


FIG. 6.10 EVOLUTION OF TEMPERATURES (°C) AT t=2.12 sec.



FIG. 6.11 EVOLUTION OF TEMPERATURES (°C) AT t=23.28 sec.

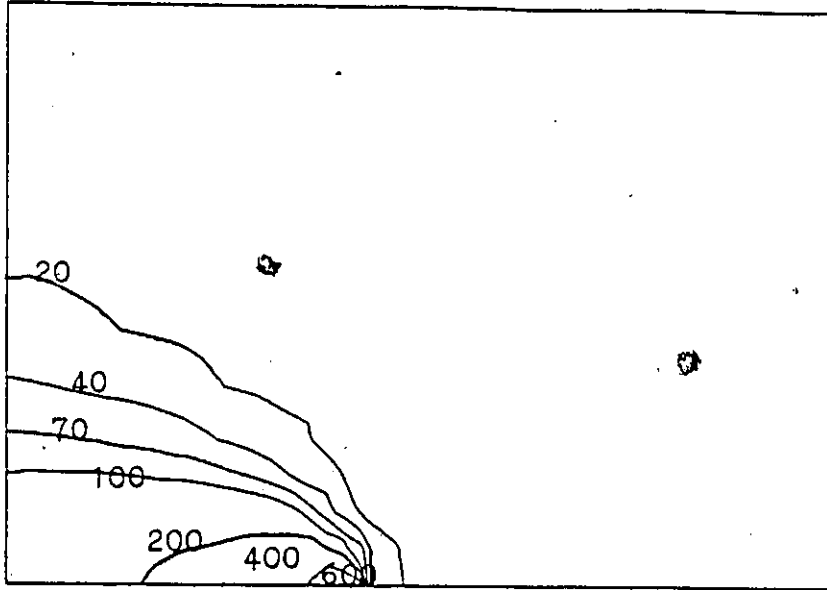


FIG. 6.12 EVOLUTION OF TEMPERATURES ( $^{\circ}$ C) AT  $t=44.45$  sec.

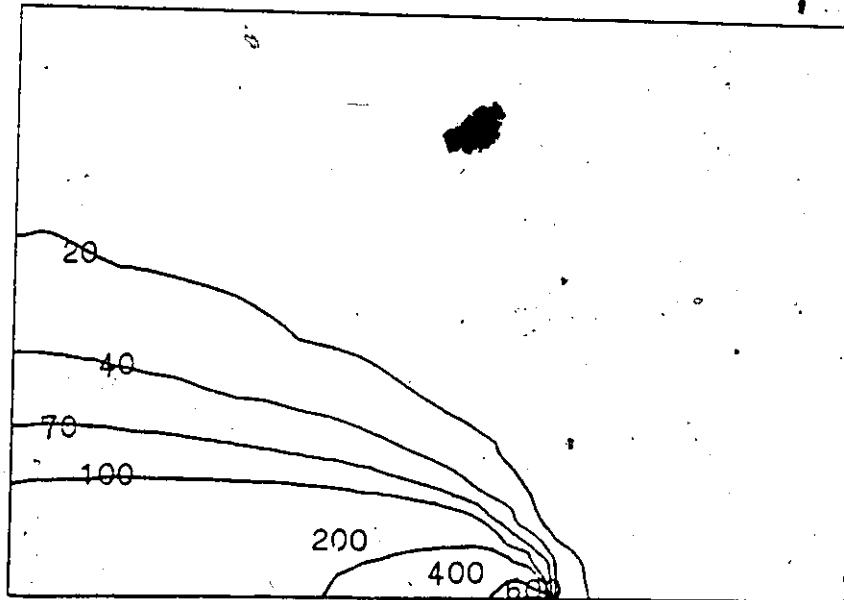


FIG. 6.13 EVOLUTION OF TEMPERATURES ( $^{\circ}$ C) AT  $t=65.62$  sec.

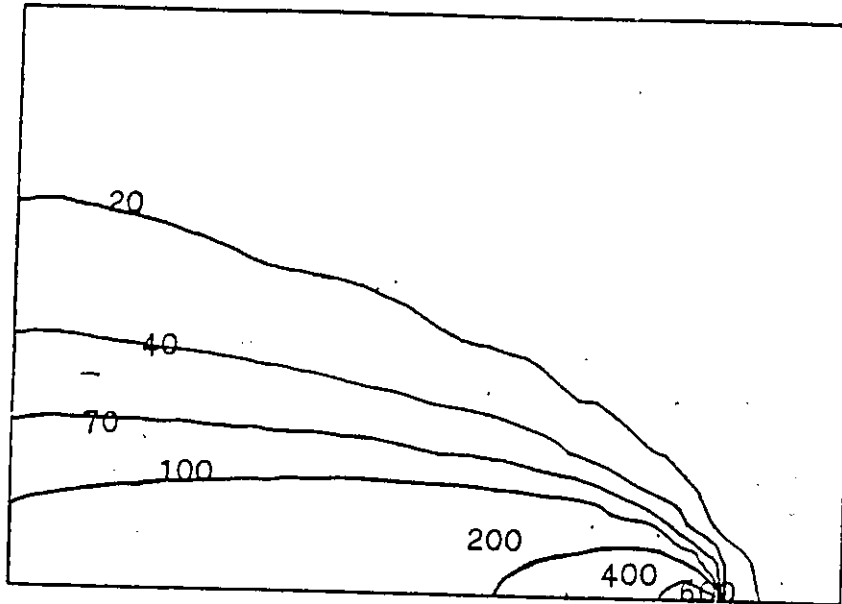


FIG. 6.14 EVOLUTION OF TEMPERATURES ( $^{\circ}$ C) AT  $t=86.78$  sec.

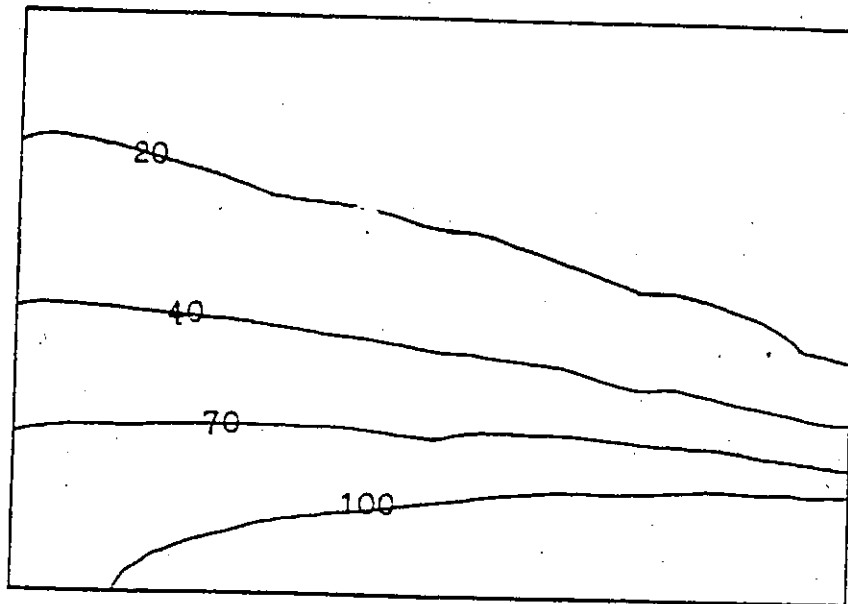


FIG. 6.15 EVOLUTION OF TEMPERATURES ( $^{\circ}$ C) AT  $t=129.12$  sec.

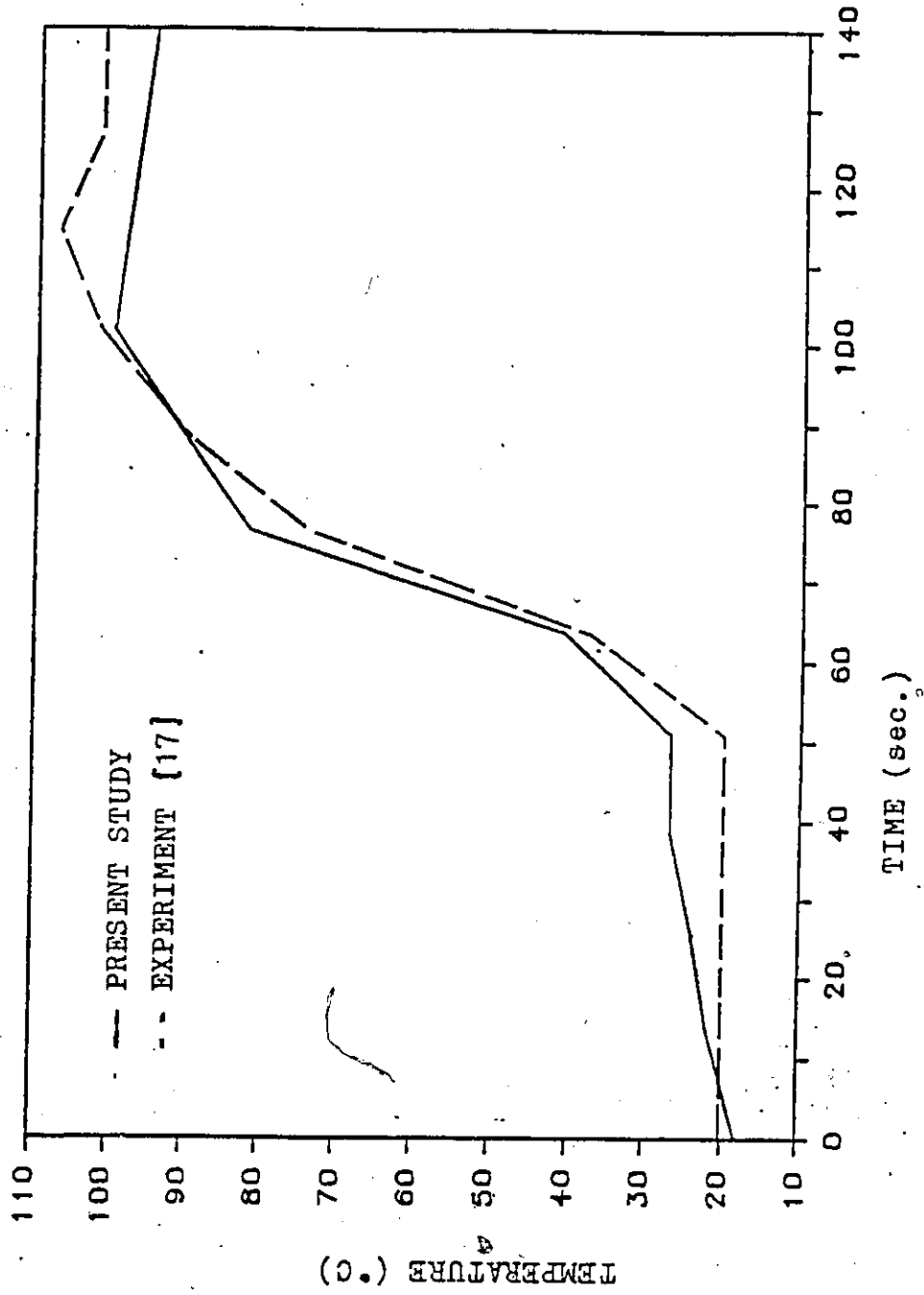


FIG. 6.16 TRANSIENT TEMPERATURE AT 2.54 cm FROM WELDING EDGE ( GMA WELD ).

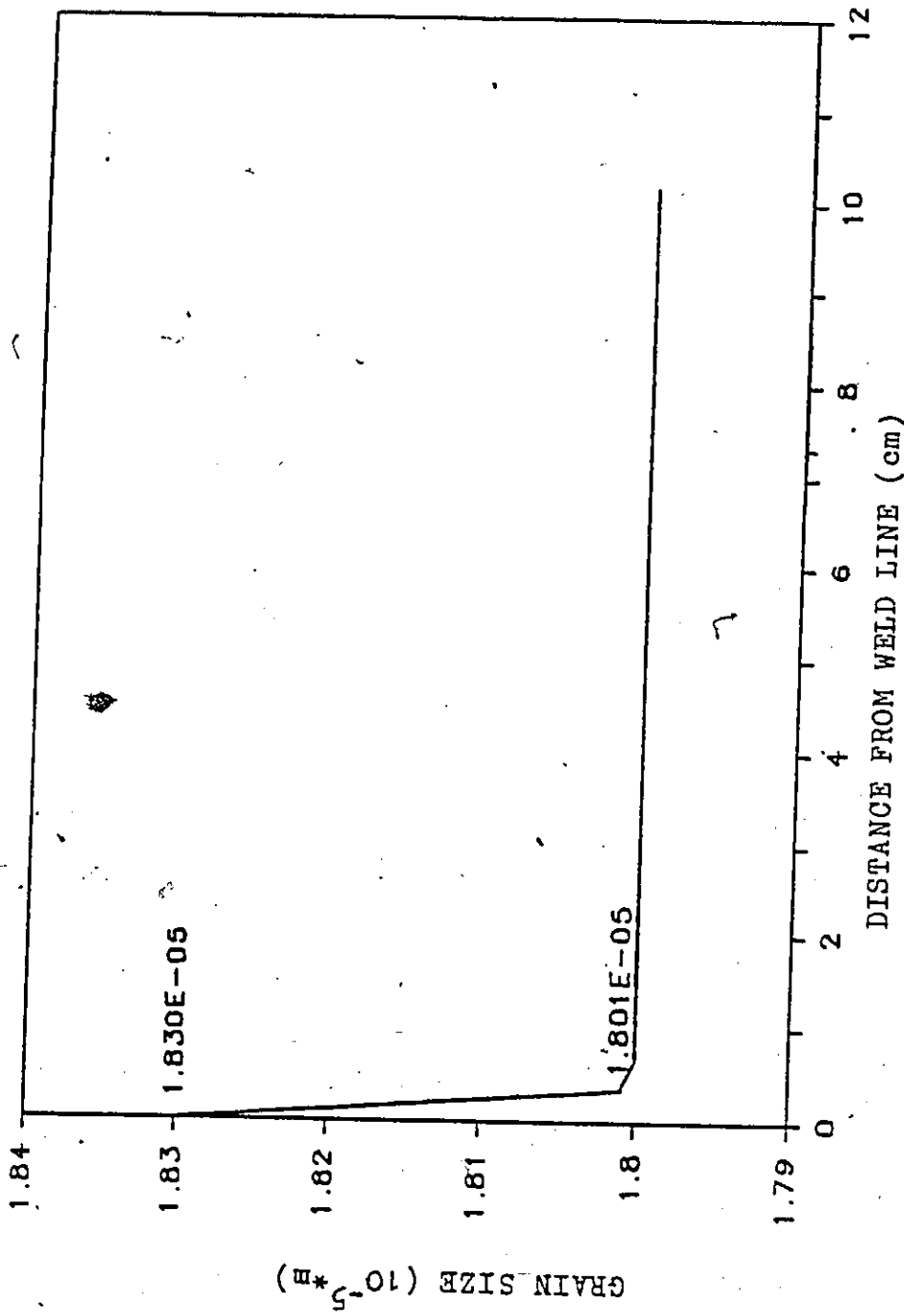
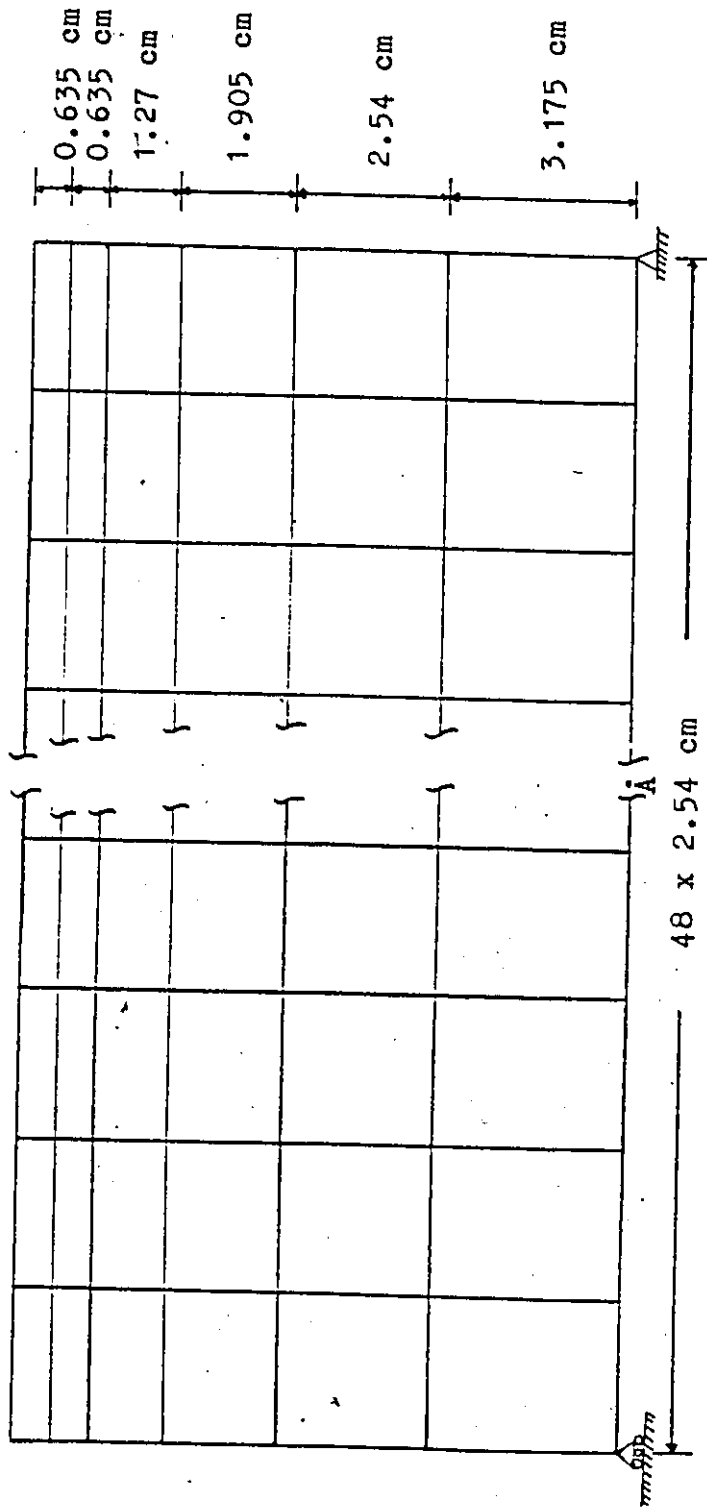


FIG. 6.17 GRAIN SIZE DISTRIBUTION.



MATERIAL PROPERTIES: Exponent,  $n = 7.9$

Dorn Constant,  $A = 10^{10}$

Activation Energy,  $Q_v = 280$  KJ/mole

Pre-exponential Diffusion Coefficient,  $D_{v0} = 3.7 \times 10^{-5}$

FIG. 6.18 MESH PATTERN AND THE VISCO-PLASTIC MATERIAL PROPERTIES [15].

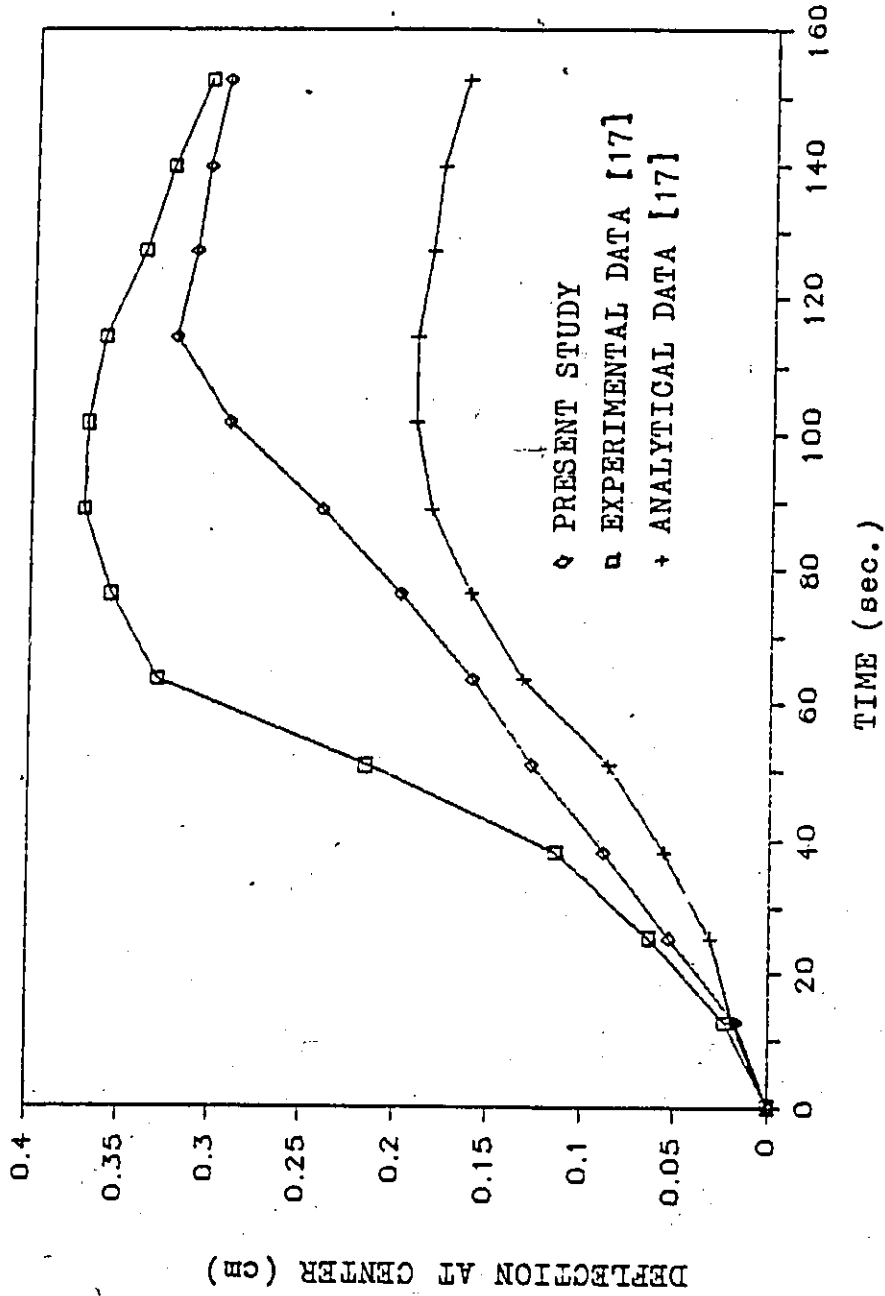


FIG. 6.19 DEFLECTION CHANGES AT THE CENTER OF 308 STAINLESS STEEL.

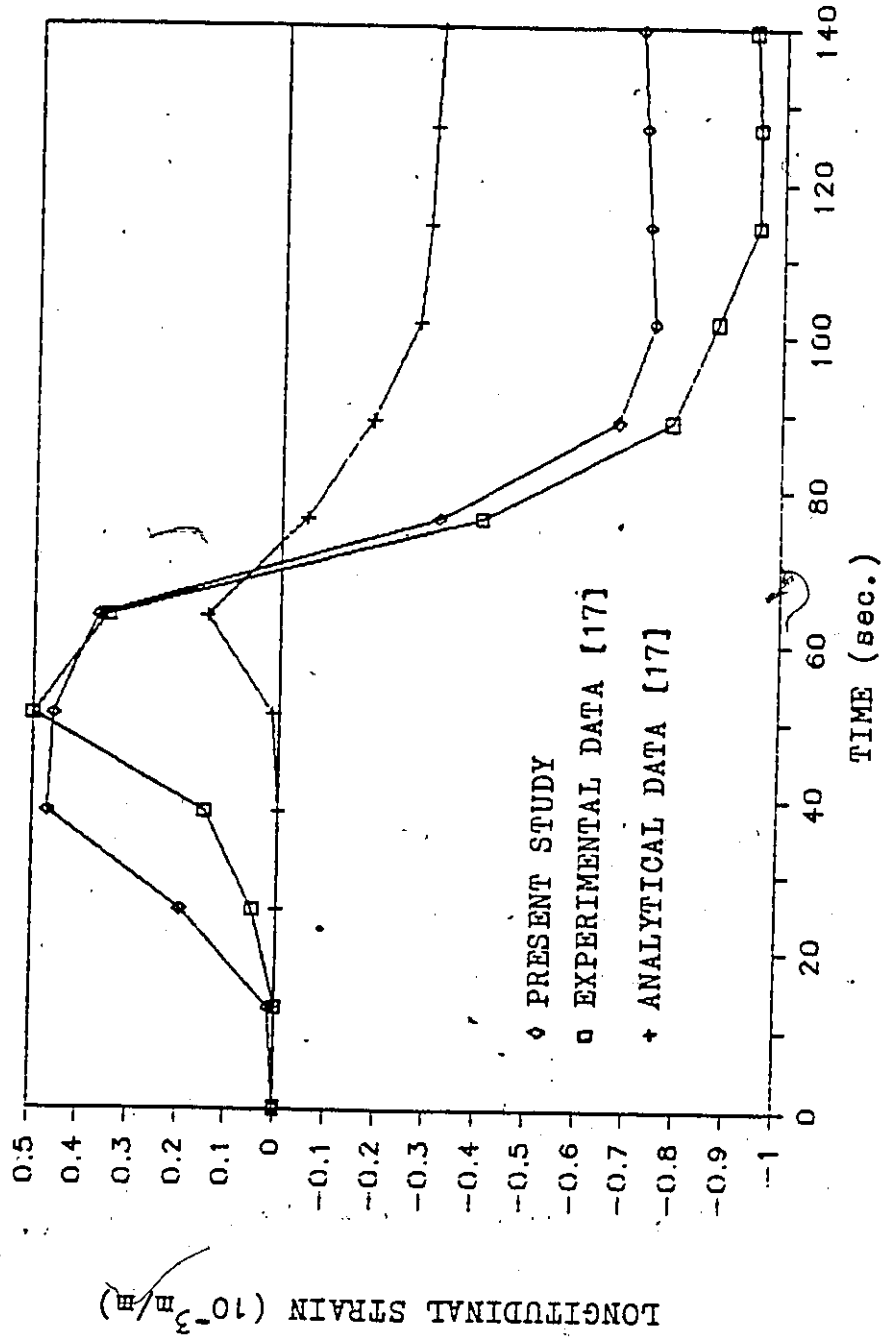


FIG. 6.20 STRAIN CHANGES FOR 308 STAINLESS STEEL AT 2.54 cm FROM WELDED EDGE.



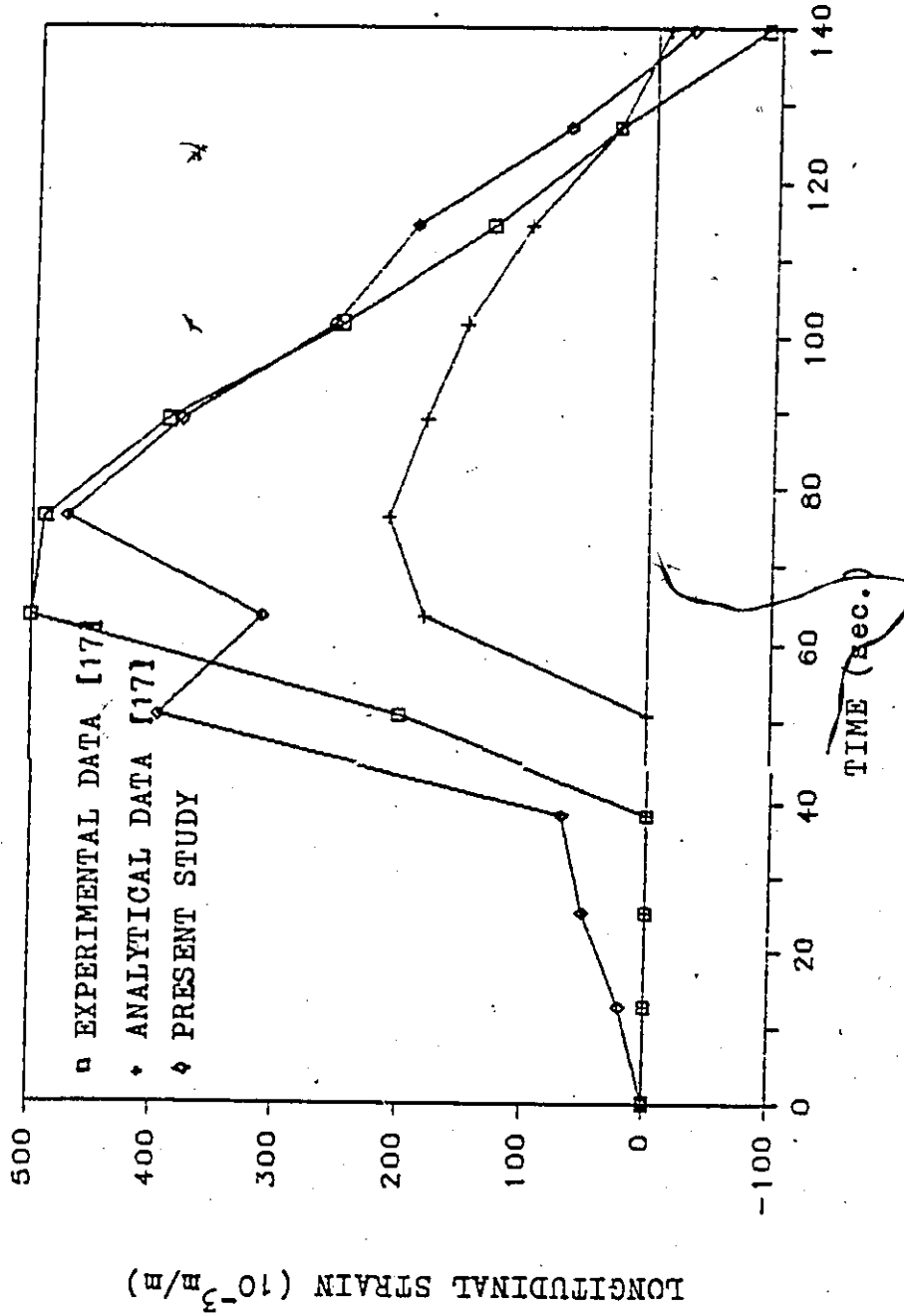


FIG. 6.21 STRAIN CHANGES FOR 308 STAINLESS STEEL AT 4.45 cm FROM WELDED EDGE.

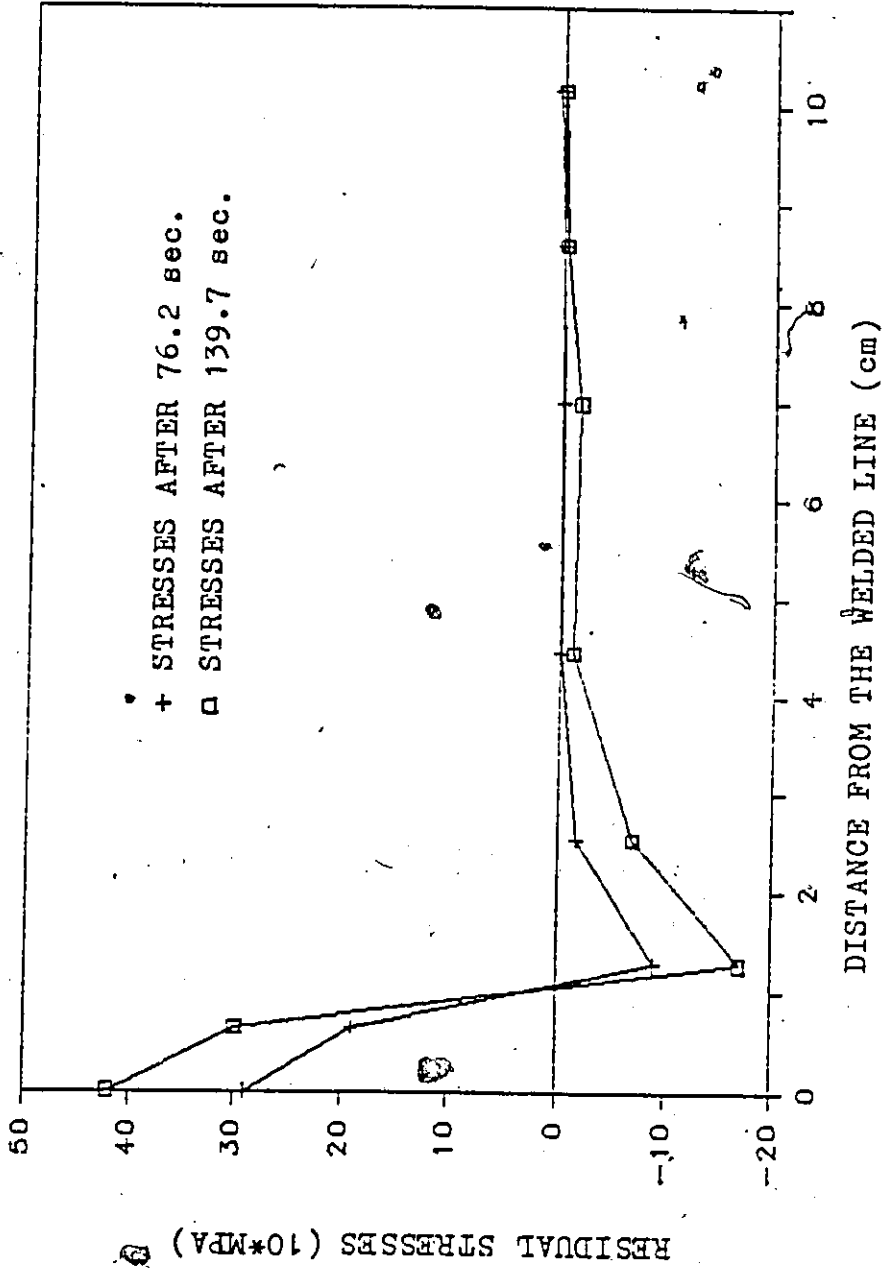


FIG. 6.22 LONGITUDINAL RESIDUAL STRESS DISTRIBUTION.

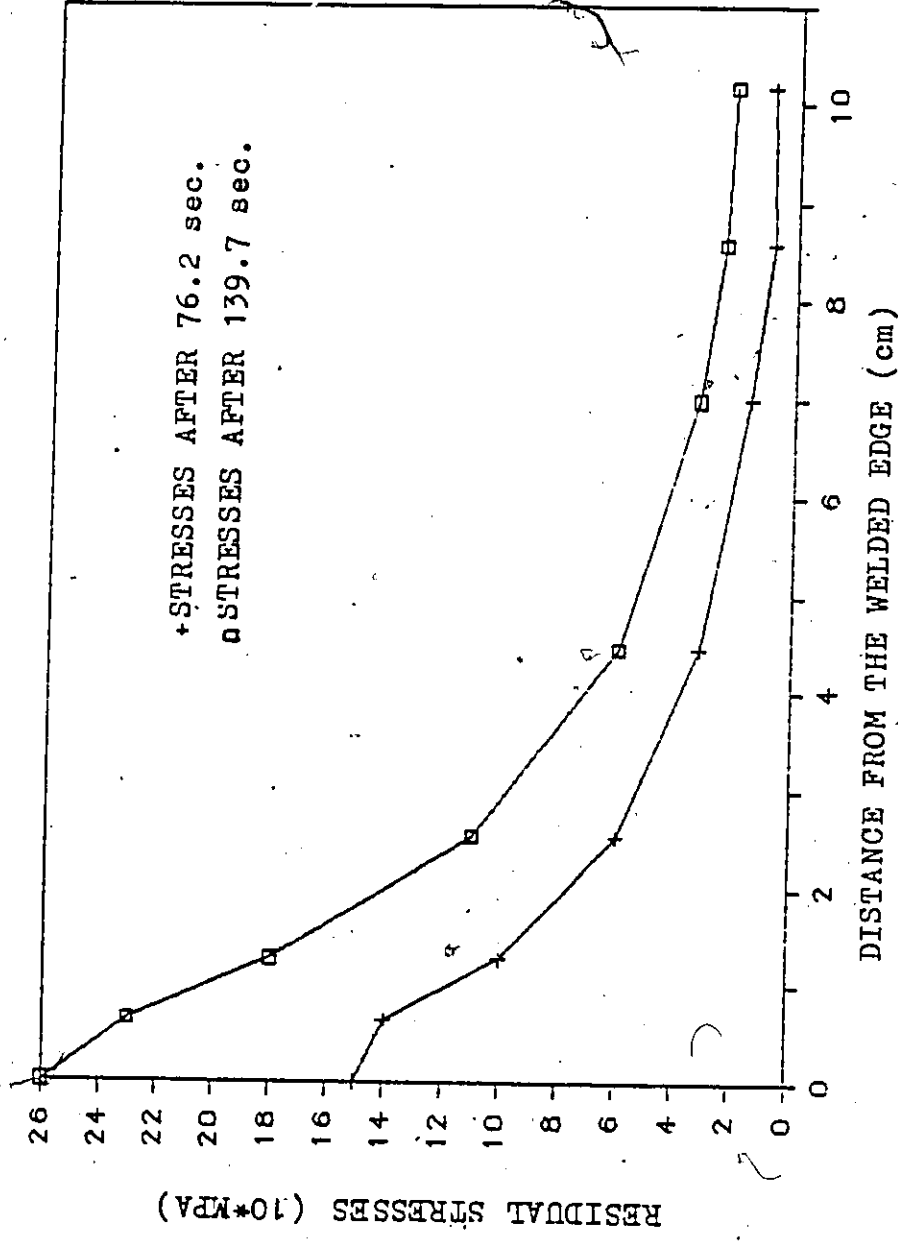


FIG. 6.23 TRANSVERSE RESIDUAL STRESS DISTRIBUTION.

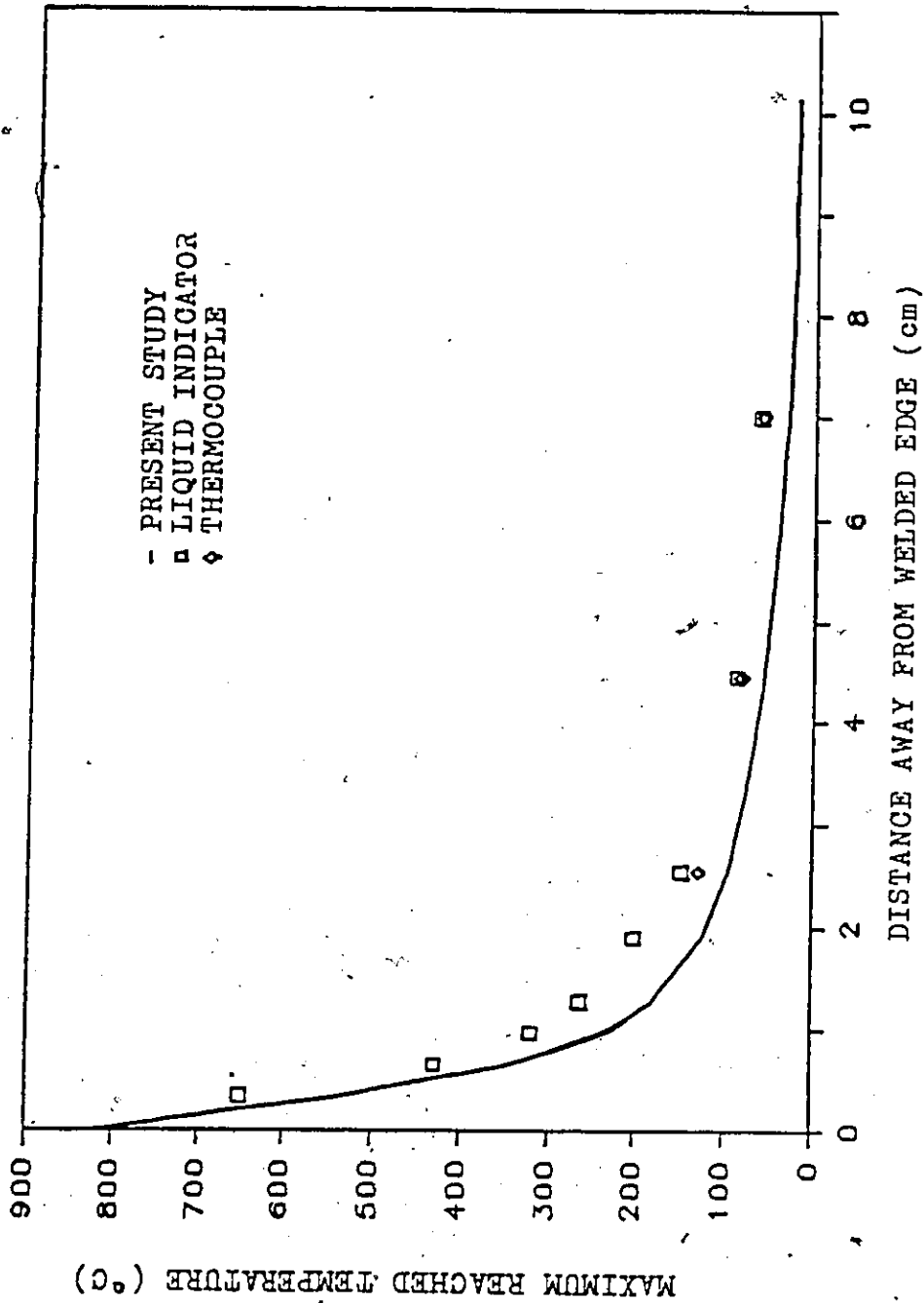


FIG. 6.24 MAXIMUM REACHED TEMPERATURE DISTRIBUTION (GTA WELD).

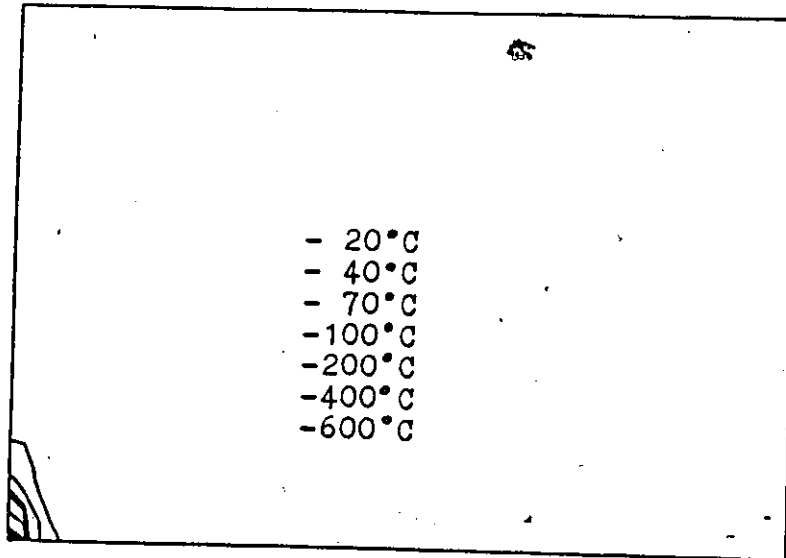


FIG. 6.25 EVOLUTION OF TEMPERATURES (°C) AT  $t=3.88$  sec.

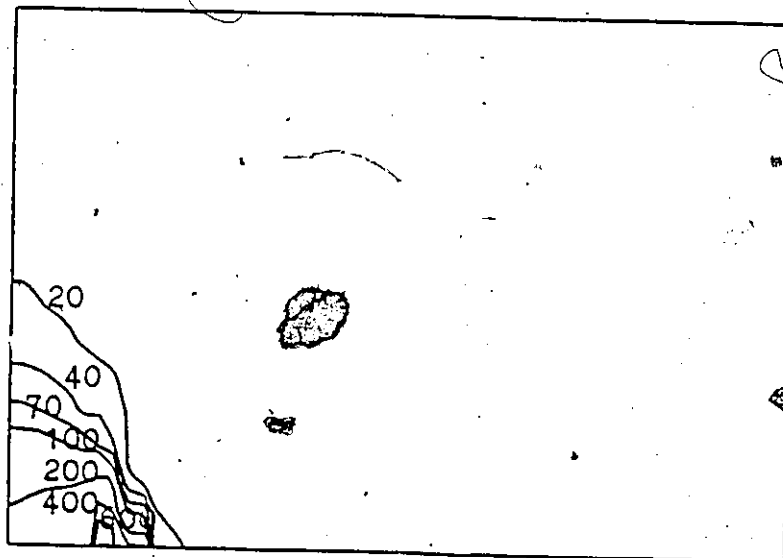


FIG. 6.26 EVOLUTION OF TEMPERATURES (°C) AT  $t=34.90$  sec.

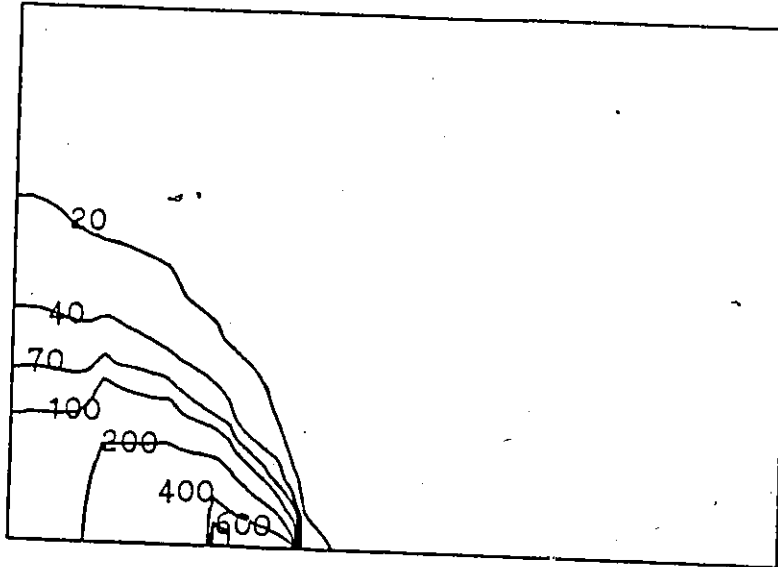


FIG. 6. 27 EVOLUTION OF TEMPERATURES ( $^{\circ}$ C) AT  $t=69.80$  sec.

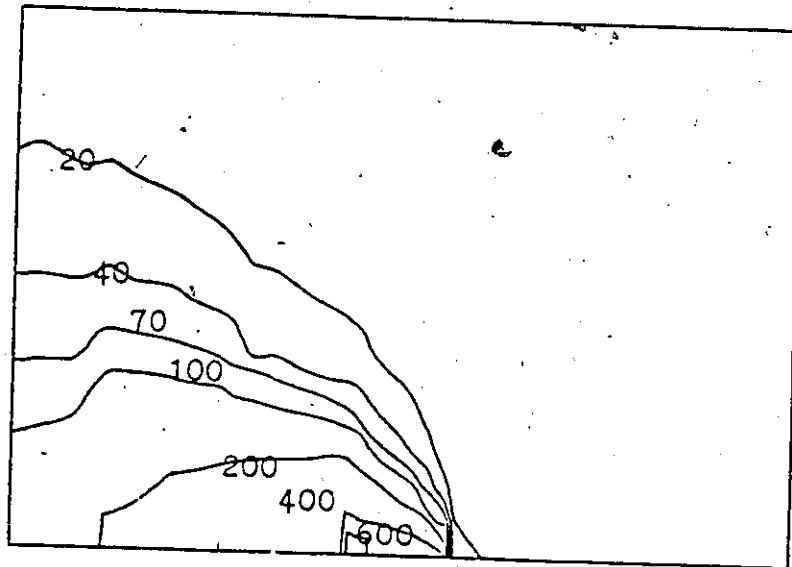


FIG. 6.28 EVOLUTION OF TEMPERATURES ( $^{\circ}$ C) AT  $t=104.70$  sec.

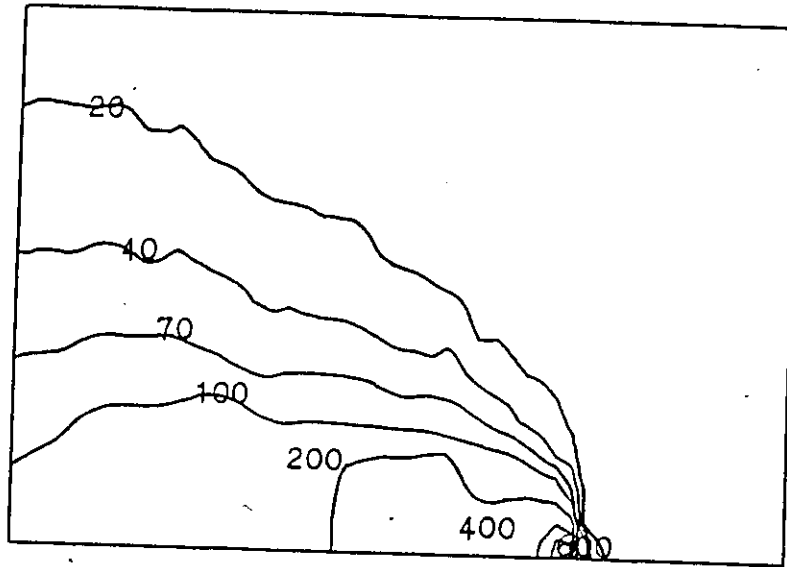


FIG. 6.29 EVOLUTION OF TEMPERATURES ( $^{\circ}\text{C}$ ) AT  $t=139.60$  sec.

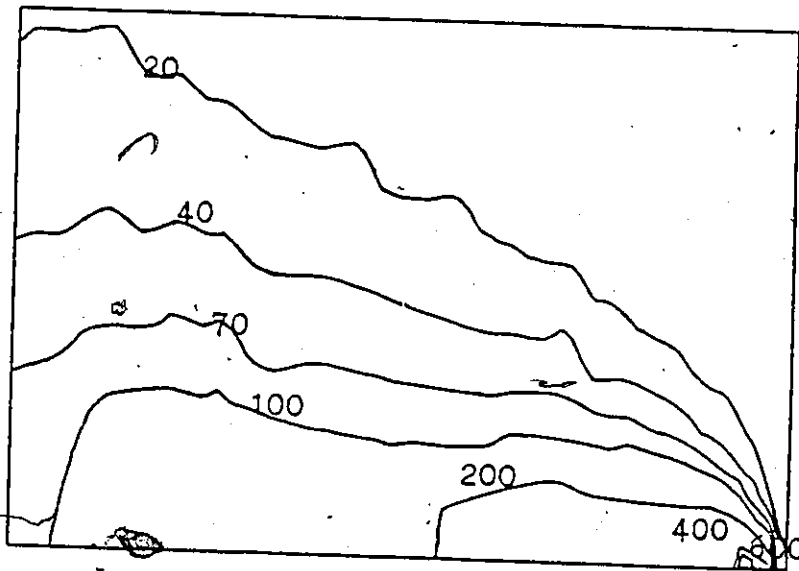


FIG. 6.30 EVOLUTION OF TEMPERATURES ( $^{\circ}\text{C}$ ) AT  $t=182.26$  sec.

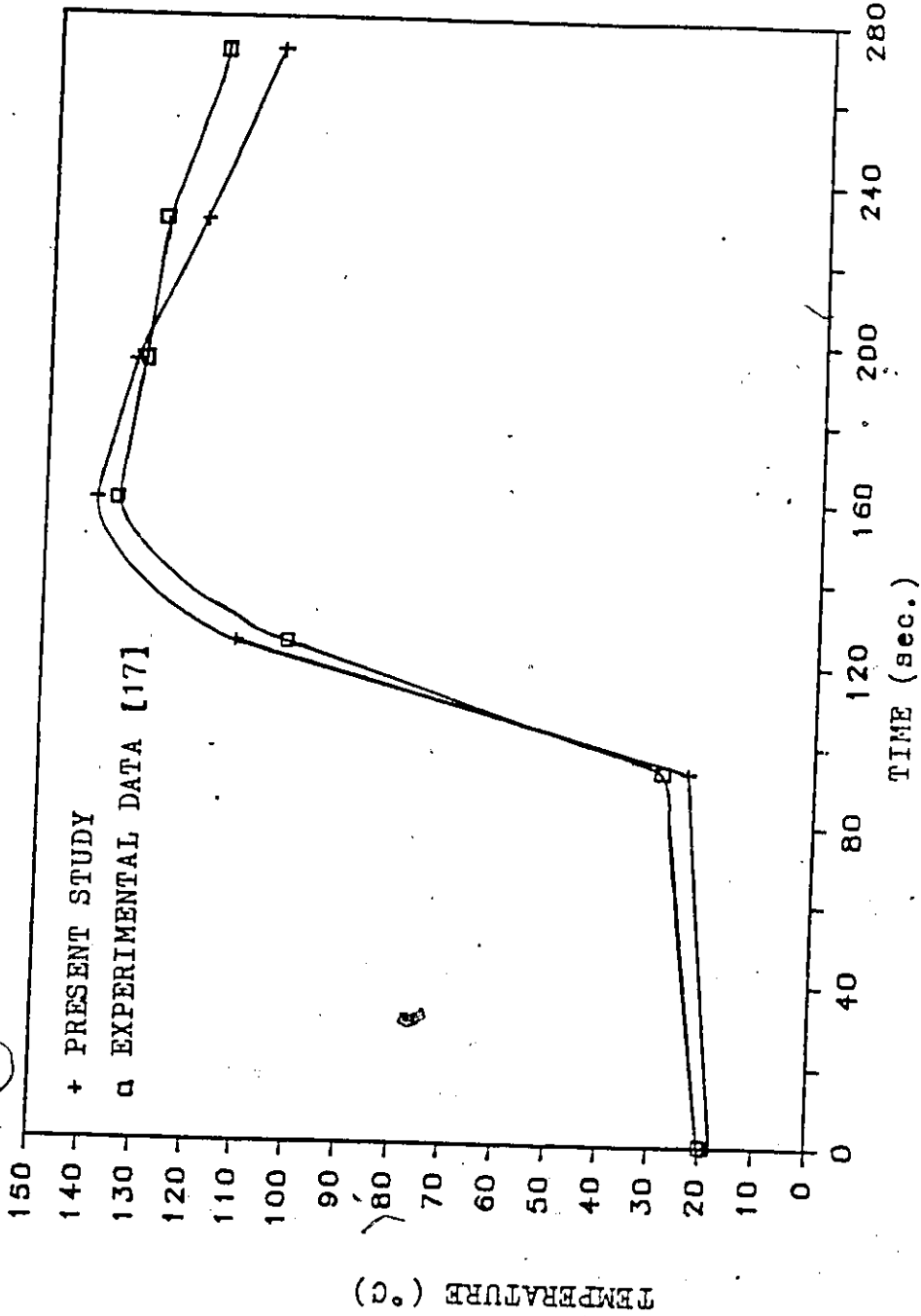


FIG. 6.31 TRANSIENT TEMPERATURE AT 2.54 cm FROM WELDING EDGE (GTA WELD).



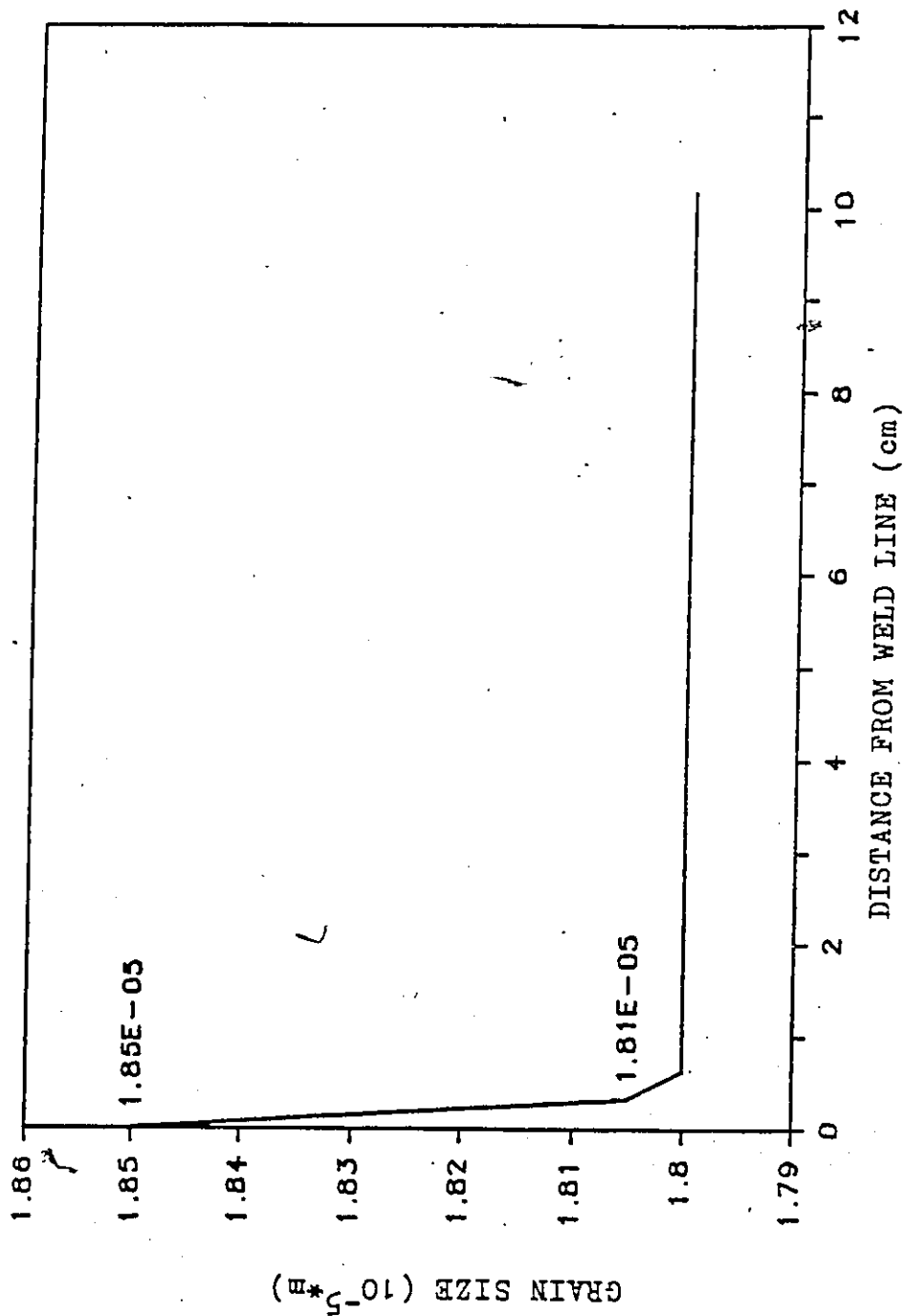


FIG. 6.32 GRAIN SIZE DISTRIBUTION.

## CHAPTER SEVEN

### CONCLUSIONS AND RECOMMENDATIONS

#### 7.1 Conclusions

The three dimensional finite element heat flow model presented in Chapter Two is found to be stable and accurate for predicting a welding thermal cycle. It is also very adequate for predicting the peak temperatures. The procedure for heat input presented turns out to be very versatile and employable for different weld types. It is also very reasonable and accurate. The effects of the molten zone turns out to be negligible on the heat flow analysis and the peak temperatures after comparison with the experimental results. The model is capable of predicting the proper temperature history for both mild steel and the austenitic stainless steel.

Numerical oscillations in the region near the weld are reduced with the use of small size element which also reproduce the high temperature gradients. The iterative approach used in heat flow finite element model is found to minimize drifting of the solution with time and at the same time is found to converge rapidly.

The three dimensional finite element grain growth model presented in Chapter Three is reasonably accurate and very stable in predicting the final size and

distribution of the austenite grains. The Avrami equation employed is found to predict the proper values for the volume fraction for all temperatures. The inclusion of the pinning force in the analysis did not alter the final distribution. Although, all of the analytical grain growth models reported in the literature have predicted the proper grain size, only the present finite element model is able to predict the proper grain size at extremes (high temperature and low cooling rates) and to yield the grain distribution along with the approximate size of the grain growth zone.

The reduced integration technique employed to suppress the transverse shear strain modes for the isoparametric shell element is found to render excellent results for both thick and thin plates provided the analysis remains in the linear elastic range. Once the analysis is extended to include material nonlinearities, it resulted in an unacceptably stiffer response. Due to the poor response, the selective integration is not recommended beyond the linear elastic range. The implicit formulation of the elastic visco-plastic finite element model, for macro-structural analysis of thick or thin plates and shells, presented in Chapter Four and the overall numerical algorithm is found to be accurate and convergent.

The Hall-Petch equation is found to be adequate for determining the magnitude of the yield stress as a function of temperature and grain size. This fact has been confirmed by comparing the predicted yield stress with the experimental data (available in the literature) in Chapter Five.

In Chapter Six, two numerical examples are used to perform the heat flow and the micro-structural analyses. The temperature history predicted has been

found to correlate very well with the experimental results reported in the literature. Although, there are no experimental results available for grain size, the distribution obtained appears to be very reasonable. One of the numerical examples, i.e. two plates welded together, is used to perform macro-structural analysis. A mixed type boundary condition, i.e. a free surface ahead of the welding arc and a contact type behind the welding arc along the line of symmetry, models the welded edge quite well. This boundary condition along with the visco-plastic strain rate equation and the Hall-Petch equation for predicting the yield stress as a function of the thermal regime and the grain size, have been employed in macro-structural model. The prediction for the transient central deflection and the transient thermal strains are in good agreement with the available experimental responses. The distribution of the normal and transverse residual stresses appear very reasonable and are similar to those reported in the literature for other arc properties of the same weld type. The magnitude of these stresses can not be compared for lack of experimental data. It appears that the accuracy depends strongly on the size of the time increment used.

The value of the longitudinal residual stress is found to be nearly as high as the yield stress for austenitic stainless steel and that the value of the transverse residual stress is found to be approximately equal to almost half the longitudinal residual stress.

Although the effects of the micro-structure are included in the overall analysis, it can not be concluded that such effects have been properly tested since the maximum temperature observed was less than 800°C. Of course, the model incorpor-

ates such effects and should always be considered especially for analyses at high temperatures or for long time exposures.

## 7.2 Recommendations

The models presented for the heat flow and the elastic visco-plastic problem in this thesis are found to render good results. Although the model is applicable to thick and thin plates and shells, computationally it is very expensive to use and at the same time requires a large scale computing facility. Costs for analyzing a full problem (with no symmetry) using the present computer program would be in thousands of dollars. Therefore, a more economical algorithm for the finite element model, which is also capable of modelling unsymmetric thick plates, is desirable.

The overall effort required to perform the elastic-visco-plastic analysis can be significantly reduced by dividing the problem into two parts. One part consists of the heat affected zone and should be analyzed using the elastic visco-plastic model. The other part requires elastic analysis. This can be accomplished through the partitioning technique and updating of the stiffness matrix will be required only where the plasticity sets in. With a more economical algorithm along with the partitioning technique above developed, it is strongly recommended to maintain the same small-time stepping for macro-structural analysis for duration of the heat input from a welding arc.

In the micro-structural analysis, the process of recrystallization has been ignored. An extension incorporating this will enable analysis of ferritic steels as well.

In order to extend the knowledge about weldments, additional experimental and analytical research is required. More experimental work is needed to determine the material properties at elevated temperatures. Also more experimental data, including the temperature history and micro and macro-structural response, is needed to further extend and verify the proposed finite element model.

**APPENDIX A**

**ELEMENT SHAPE FUNCTION**

**APPENDIX A1: Shell Element**

**APPENDIX A2: Brick Element**

## APPENDIX A: ELEMENT SHAPE FUNCTION

### APPENDIX A1: Shell Element

$$N_1 = \frac{\xi\eta}{4}(1-\xi)(1-\eta)$$

$$N_2 = \frac{-\xi\eta}{4}(1+\xi)(1-\eta)$$

$$N_3 = \frac{\xi\eta}{4}(1+\xi)(1+\eta)$$

$$N_4 = -\frac{\xi\eta}{4}(1-\xi)(1+\eta)$$

$$N_5 = -\frac{\eta}{2}(1-\xi^2)(1-\eta)$$

$$N_6 = \frac{\xi}{2}(1-\eta^2)(1+\xi)$$

$$N_7 = \frac{\eta}{2}(1-\xi^2)(1+\eta)$$

$$N_8 = -\frac{\xi}{2}(1-\eta^2)(1-\xi^2)$$

$$N_9 = (1-\eta^2)(1-\xi^2)$$



APPENDIX A2: Brick Element

$$N_1 = \frac{1}{8} (1 + \xi)(1 + \eta)(1 + \zeta)(\xi + \eta + \zeta - 2)$$

$$N_2 = \frac{1}{8} (1 - \xi)(1 + \eta)(1 + \zeta)(\zeta + \eta - \xi - 2)$$

$$N_3 = \frac{1}{8} (1 - \xi)(1 - \eta)(1 + \zeta)(\zeta - \eta - \xi - 2)$$

$$N_4 = \frac{1}{8} (1 + \xi)(1 - \eta)(1 + \zeta)(\zeta - \eta - \xi - 2)$$

$$N_5 = \frac{1}{8} (1 + \xi)(1 + \eta)(1 - \zeta)(\xi + \eta - \zeta - 2)$$

$$N_6 = \frac{1}{8} (1 - \zeta)(1 + \eta)(1 - \xi)(\eta - \zeta - \xi - 2)$$

$$N_7 = \frac{1}{8} (1 - \xi)(1 - \eta)(1 - \zeta)(-\xi - \eta - \zeta - 2)$$

$$N_8 = \frac{1}{8} (1 + \xi)(1 - \eta)(1 - \zeta)(\xi - \eta - \zeta - 2)$$

$$N_9 = \frac{1}{4} (1 + \eta)(1 + \zeta)(1 - \eta^2)$$

$$N_{10} = \frac{1}{4} (1 - \xi)(1 + \zeta)(1 - \eta^2)$$

$$N_{11} = \frac{1}{4}(1 + \zeta)(1 - \eta)(1 - \xi^2)$$

$$N_{12} = \frac{1}{4}(1 + \zeta)(1 + \xi)(1 - \eta^2)$$

$$N_{13} = \frac{1}{4}(1 + \eta)(1 - \zeta)(1 - \xi^2)$$

$$N_{14} = \frac{1}{4}(1 - \xi)(1 - \zeta)(1 - \eta^2)$$

$$N_{15} = \frac{1}{4}(1 - \eta)(1 - \zeta)(1 - \xi^2)$$

$$N_{16} = \frac{1}{4}(1 + \xi)(1 - \zeta)(1 - \eta^2)$$

$$N_{17} = \frac{1}{4}(1 + \eta)(1 + \xi)(1 - \zeta^2)$$

$$N_{18} = \frac{1}{4}(1 + \eta)(1 - \xi)(1 - \zeta^2)$$

$$N_{19} = \frac{1}{4}(1 - \xi)(1 - \eta)(1 - \zeta^2)$$

$$N_{20} = \frac{1}{4}(1 + \xi)(1 - \eta)(1 - \zeta^2)$$

APPENDIX B

CONSTRUCTION OF ORTHOGONAL BASIS

## APPENDIX B

### CONSTRUCTION OF ORTHOGONAL BASIS

If a vector  $\bar{V}_3$  is defined by its three cartesian components, then a unique orthogonal basis can be constructed as follows:

Let

$$\bar{I} = \begin{Bmatrix} 1 \\ 0 \\ 0 \end{Bmatrix}$$

then

$$\bar{V}_1 = \bar{I} \times \bar{V}_3$$

which is normal to the plane defined by the vectors  $\bar{V}_3$  and  $\bar{I}$ . One should note that this procedure fails if  $\bar{V}_3$  is parallel to  $\bar{I}$  and a vector  $\bar{j}$  should be used instead, where

$$\bar{j} = \begin{Bmatrix} 0 \\ 1 \\ 0 \end{Bmatrix}$$

$$\bar{V}_2 = \bar{V}_3 \times \bar{V}_1.$$

To obtain the unit vectors ( $\bar{v}_1, \bar{v}_2, \bar{v}_3$ ), one simply needs to divide by their scalar length,  $|V|$ ,

$$|V| = \sqrt{V_1^2 + V_2^2 + V_3^2}.$$

This approach is suggested by Ahmad et al. [1].

## APPENDIX C

### MATHEMATICAL MODEL FOR CARBIDE/NITRIDE PINNING FORCE

The pinning force presented in Chapter Three is based on Zener's observation [23] where the grain boundaries are pinned by the presence of a second phase inclusion. The presence of carbide give rise to the pinning force which can be approximated by

$$P[T(t)] = \frac{3f_v}{2r} \quad (C.1)$$

and then by assuming that the number of particles per volume fraction  $N_v$  remain constant, Equation C.1 is re-written as

$$P[T(t)] = \frac{1}{2}(3f_v)^{2/3}(4\pi N_v)^{1/3} \quad (C.2)$$

In order to determine the pinning force, the volume fraction needs to be first approximated. By adopting Avrami equation, the volume fraction can be computed as a function of the initial volume fraction,  $f_{v0}$ , the diffusion coefficient for particle dissolution,  $D$ , time,  $t$ , and the radius of the volume matrix,  $\ell$ , ie.,

$$f_v = f_{v0} \exp - \left[ \frac{(6Dt)^{3/2}}{\ell^3} \right] \quad (C.3)$$

In order to implement the above equation, it has to be re-written as a rate equation after which one can determine the magnitude of the pinning force.

By differentiating Equation C.3 with respect to time yields

$$\begin{aligned} \frac{\partial f_v}{\partial t} &= f_{v0} \left[ \exp - \left[ \frac{(6Dt)^{3/2}}{\ell^3} \right] \right] \cdot \left[ \frac{-(6D)^{3/2}}{\ell^3} \right] \left[ \frac{3}{2} t^{1/2} \right] \\ &= -\frac{3}{2} f_{v0} t^{1/2} \frac{(6D)^{3/2}}{\ell^3} \exp - \left[ \frac{(6Dt)^{3/2}}{\ell^3} \right] \end{aligned} \quad (C.4)$$

In order to reduce Equation C.4 to a single valued function, using Equation C.3, the following relation is obtained

$$t^{1/2} = \frac{\ell}{\sqrt{6D}} \text{Log}^{1/3} \left( \frac{f_{v0}}{f_v} \right) \quad (C.5)$$

which after substituting into the rate equation yields

$$\frac{\partial f_v}{\partial t} = \frac{-9D}{\ell^2} f_v \text{Log}^{1/3} \left( \frac{f_{v0}}{f_v} \right) \quad (C.6)$$

Now re-arranging Equation C.6 yields



$$\frac{df_v}{f_v \text{Log}^{1/3} \left( \frac{f_{v0}}{f_v} \right)} = \frac{-9D}{\ell^2} dt. \quad (\text{C.7})$$

Integrating both sides yields

$$\int_{f_{v_i}}^{f_{v_{i+1}}} \frac{df_v}{f_v \text{Log}^{1/3} \left( \frac{f_{v0}}{f_v} \right)} = \int_{t_i}^{t_{i+1}} \frac{-9D}{\ell^2} dt$$

$$\Rightarrow f_{v_{i+1}} = \frac{f_{v0}}{\exp \left[ \frac{6D(t^{i+1} - t^i)}{\ell^2} + \text{Log}^{2/3} \frac{f_{v0}}{f_{v_i}} \right]^{3/2}} \quad (\text{C.8})$$

Having obtained Equation C.8, one can incrementally compute the changes in the volume fraction and subsequently compute the value of the pinning force as given in Equation C.2. Moreover, to check the accuracy of the mathematical manipulation of Equation C.8, one should obtain the Avrami equation by setting  $t_i$  equal to zero and  $f_{v_i}$  equal to the initial volume fraction. This yields

$$f_v = \frac{f_{v0}}{\exp \left[ \frac{6Dt}{\ell^2} + \log^{2/3} \frac{f_{v0}}{f_v} \right]^{3/2}}$$



$$= f_{v0} \exp - \left[ \frac{(6Dt)^{3/2}}{\rho^3} \right] \quad (C.9)$$

which is the Avrami Equation.

This implies that the physics of the Avrami equation was not altered while obtaining Equation C.8.

## APPENDIX D

### STEFFENSEN METHOD

The Steffensen iterative approach is adopted to solve the non-linear grain growth equation. This method is a modification to the Newton-Raphson iterative method and is also quadratically convergent [26]. It is used in this study because it was found to converge faster than the Newton-Raphson method. The Steffensen iteration algorithm as given by Conte and Boor [12] is used and is summarized below;

Given the iteration function  $g(x)$ , Equation 3.19, and an initial grain size,

$y_0$

	- set $x_0 = y_n$
	- Calculate $x_1 = g(x_0)$ and $x_2 = g(x_1)$
REPEAT FOR	- Calculate $d = (x_2 - x_1)$
$n=0,1,2,..$	
until satisfied	- Calculate $r = (x_1 - x_0)/d$
	- Calculate $y_{n+1} = x_2 + d/(r-1)$

For more information refer to Morris [26] or Conte and Boor [12].

## APPENDIX E

### NUMERICAL INSTABILITY IN THE GRAIN GROWTH MODEL

From the grain growth model presented in Chapter Three, one was able to obtain the following rate equation

$$\frac{d\phi}{dt} = A \left[ \frac{1}{\phi} + B \right] \exp - \frac{Q}{RT} \quad (E.1)$$

where

$$\begin{aligned} A &= \text{kinetic constant,} \\ B &= -\frac{1}{2} (4\pi N_v)^{1/3} (3f_v)^{2/3} \end{aligned}$$

which, after re-arranging, yielded

$$\frac{\phi d\phi}{1+B\phi} = A \cdot \exp - \frac{Q}{RT} \cdot dt. \quad (E.2)$$

Equation E.2 can be integrated exactly, ie.

$$\int_{\phi_i}^{\phi_{i+1}} \frac{\phi d\phi}{1+B\phi} = \int_{t_i}^{t_{i+1}} A \cdot \exp - \frac{Q}{RT} \cdot dt$$

$$\left[ \frac{\phi}{B} - \frac{1}{B^2} \text{Log}(1 + B\phi) \right]_{\phi_1}^{\phi_{i+1}} = A \exp - \frac{Q}{RT} (t_{i+1} - t_i) \quad (\text{E.3})$$

By ignoring the limit of integration, Equation E.3 can be written as

$$\phi - \frac{1}{B} \log(1 + B\phi) = ABt \exp - \frac{Q}{RT} \quad (\text{E.4})$$

With the increase in temperature, the volume fraction will decrease and so will the value of B until it reaches zero. This will take place when the carbide has completely dissolved and the pinning force is no longer present. Examining Equation E.4 in the limit as B goes to zero yields

$$\begin{aligned} \lim_{B \rightarrow 0} \left[ \phi - \frac{1}{B} \log(1 + B\phi) - ABt \exp - \frac{Q}{RT} \right] &= \lim_{B \rightarrow 0} \left[ \phi - \frac{B}{1 + B\phi} \right] \\ &= \phi \end{aligned} \quad (\text{E.5})$$

This implies that as the pinning force reaches zero, there will be no grain growth. However, from the physics of the problem and experimental observations, it is believed that as the pinning force goes to zero, the grain grows quadratically. This can be still achieved by setting B equal to zero in Equation E.1, i.e.,

$$\frac{d\phi}{dt} = A \frac{1}{\phi} \exp - \frac{Q}{RT} \quad (\text{E.6})$$

which after integrating yields

$$\frac{\phi^2}{2} \Big|_{\phi_1}^{\phi_{i+1}} = A \exp - \frac{Q}{RT} \cdot t \Big|_{t_i}^{t_{i+1}} \quad (E.7)$$

This implies that the model is unstable once the pinning force or the volume fraction goes to zero. To eliminate this difficulty, it was decided to check the value of the pinning force with respect to a specified value, and if it is small enough then Equation E.7 is used instead of Equation E.3 in the calculation of austenite grain growth.

## BIBLIOGRAPHY

- [1] Ahmad, S., Irons, B.M., and Zienkiewicz, O.C., "Analysis of Thick and Thin Shell Structures by Curved Finite Elements", Int. J. Num. Meth. in Eng., Vol. 2, 1970, pp. 419-451.
- [2] Akselsen, O.M., Grong, O., Ryum, N., and Christensen, N., "HAZ Grain Growth Mechanisms in Welding of Low Carbon Microalloyed Steels", Acta Metall., Vol. 34, No. 9, 1986, pp. 1807-1815.
- [3] Alberry, P.J. and Jones W.K.C., "Diagram for the Prediction of Weld Heat-Affected Zone Microstructure", Metals Technology, 1977, pp. 360-364.
- [4] Alberry, P.J. and Jones, W.K.C., "Computer Model for Prediction of Heat-Affected Zone Microstructures in Multipass Weldments", Metals Technology, Vol. 9, 1982, pp. 419-426.
- [5] Argyris, J.H., Szimmat, J., and William, K.J., "Computational Aspects of Welding Stress Analysis", Computer Methods in Applied Mechanics and Engineering, Vol. 33, 1982, pp. 635-666.
- [6] Ashby, M.F. and Easterling, K.E., "A first Report on Diagrams For Grain Growth in Welds", Acta Metall., Vol. 30, 1982, pp. 1969-1973.

- [7] Bathe, K.J., "Finite Element Procedures in Engineering Analysis", Prentice Hall, New Jersey, 1982.
  
- [8] Bathe, K.J. and Bolourchi, S., "A Geometric and Material Nonlinear Plate and Shell Element", Computers and Structures, Vol. 11; 1980, pp. 23-48.
  
- [9] Beer, G. and Meek, J.L., "Transient Heat Flow in Solids", Finite Element Methods in Engineering, 1974, pp. 729-740.
  
- [10] Carslaw, H.S. and Jaeger, J.C., "Conduction of Heat in Solids", Oxford University Press, Great Britain, 1959.
  
- [11] Chidiac, S.E., "Finite Element Modelling of Residual Stresses via Thermal-Elasto-Plastic Analysis", M.Eng. Thesis, McMaster University, 1985.
  
- [12] Conte, S.D. and de Boor, C., "Elementary Numerical Analysis; An Algorithmic Approach", McGraw-Hill Book Co., New York, 1980.
  
- [13] Dokainish, M.A., "INDAP-A Finite Element Program for Incremental Nonlinear Dynamic Analysis", Dept. of Mechanical Engineering, McMaster University, January 1987.

- [14] Easterling, K., "Introduction to the Physical Metallurgy of Welding", Butterworths & Co. Ltd., London, 1983.
- [15] Frost, H.J. and Ashby, M.F., "Deformation-Mechanism Maps: The Plasticity and Creep of Metals and Ceramics", Pergamon Press, Oxford, 1982.
- [16] Hinton, E. and Owen, D.R.J., "Finite element Programming", Academic Press, New York, 1980.
- [17] Hwang, J.S., "Residual Stresses in Weldments in High Strength Steels", M.S. Thesis, M.I.T., January 1976.
- [18] Ion, J.C., Easterling, K.E., and Ashby, M.F., "A Second Report on Diagrams of Microstructure and Hardness for Heat-Affected Zones in Welds", Acta Metall., Vol. 32, No. 11, 1984, pp. 1949-1984.
- [19] Irons, B.M., "Engineering Applications of Numerical Integration in the Stiffness Method", A.I.A.A. J., Vol. 4, 1966, pp. 2035-2037.
- [20] Kanchi, M.B., Zienkiewicz, O.C., and Owen, D.R.J., "The Visco-Plastic Approach to Problems of Plasticity and Creep Involving Geometric Non-Linear Effects", Int. J. Num. Meth. in Eng., Vol. 12, 1978, pp. 169-181.



- [21] Kihara, H., Suzuki, H., and Tamura, H., "Researches on Weldable High-Strength Steels", 60th Anniversary Series, Vol. 1, The Society of Naval Architects of Japan, Tokyo, 1957.
- [22] Kraus, H., "Creep Analysis", John Wiley & Sons, New York, 1980.
- [23] Martin, J.W. and Doherty, R.D., "Stability of Microstructure in Metallic Systems", Cambridge University Press, Cambridge, 1976.
- [24] Masubushi, K., "Analysis of Welded Structures", Pergamon Press Ltd., Oxford, 1980.
- [25] Mirza, F.A., Shehata, A.A., and Korol, R.M., "Elasto-Plastic Finite Analysis of Double Chord Rectangular Hollow Section T-Joints", Computer and Structures, Vol. 19, 1984, pp. 829-838.
- [26] Morris, J.L.L., "Computational Methods in Elementary Numerical Analysis", John Wiley & Sons Inc., New York, 1983.
- [27] Norstrom, L.-A., "The Influence of Nitrogen and Grain Size on Yield Strength in Type AISI 316L Austenitic Stainless Steel", Metal Science, 1977, pp. 208-212.
- [28] Owen, D.R.J., and Hinton, E., "Finite Elements in Plasticity: Theory and Practice", Pineridge Press, Swansea, 1980.

- [29] Pawsey, S.F. and Clough, R.W., "Improved Numerical Integration of Thick Shell Finite Elements", *Int. J. Num. Meth. in Eng.*, 1971., pp. 575-586.
- [30] Snyder, M.D. and Bathe, K.J., "A Solution Procedure for Thermo—Elastic—Plastic and Creep Problems", *Nuclear Engineering and Design*, Vol. 64, 1981, pp. 49-80.
- [31] Stanton, E.L. and Schmit, L.A., "A Discrete Element Stress and Displacement Analysis of Elasto—Plastic Plates", *AIAA J.*, Vol. 8, No. 7, July 1970, pp. 1245-1251.
- [32] Takenti, Y., Komori, S., Noda, N., and Nyuko, H., "Thermal Stress Problems in Industry. 3: Temperature Dependency of Elastic Moduli for Several Metals at Temperatures From -196 to 1000°C", *Journal of Thermal Stresses*, Vol. 2, 1979, pp. 233-250.
- [33] Tobler, R.L., Beekman, D.H., and Reed, R.P., "Factors Influencing the Low—Temperature Dependence of Yielding in AISI 316 Stainless Steel", in *Austenitic Steels at Low Temperatures* ( R.P. Reed and T. Horiuchi, Eds.), Plenum Press, New York, 1983.
- [34] Yamada, Y., Yishimura, N. and Sakurai, T., "Plastic Stress—strain Matrix and its Application for the Solution of Elastic—Plastic Problems by

the Finite Element Method", Int. J. Mech. Sci., Vol. 10, 1968, pp. 343-354.

- [35] Zienkiewicz, O.C., "The Finite Element Method", McGraw-Hill, London, 1977.
- [36] Zienkiewicz, O.C. and Parekh, C.J., "Transient Field Problems: Two-Dimensional and Three-Dimensional Analysis by Isoparametric Finite Elements", Int. J. Num. Meth. in Eng., Vol. 2, 1970, pp. 61-71.
- [37] Zienkiewicz, O.C. and Corneau, I.C., "Visco-Plasticity Plasticity and Creep in Elastic Solids — A Unified Numerical Solution Approach", Int. J. Num. Meth. in Eng., Vol. 8, 1974, pp. 821-845.
- [38] Zienkiewicz, O.C., Taylor, R.L., and Too, J.M., "Reduced Integration Technique in General Analysis of Plates and Shells", Int. J. Num. Meth. in Eng., Vol. 3, 1971, pp. 275-290.
- [39] Zienkiewicz, O.C., Valliappan, S., and , I.P., "Elasto-Plastic Solutions of Engineering Problems. Initial-Stress, Finite Element Approach", Int. J. Num. Meth. in Eng., Vol. 1, 1969, pp 75-100.